University of Alberta

Spectroscopic and Electronic Characterization of Microfabricated Solid State Molecular Electronic Junctions

by

Amr Mohamed Mahmoud Mohamed

A thesis submitted to the Faculty of Graduate Studies and Research
in partial fulfillment of the requirements for the degree of

Doctor of Philosophy

Department of Chemistry

Fall 2012
Edmonton, Alberta

Dedication

To my mother, Fatma, who gave me my life

& to my wife, Fatma, who gave me her life.

Abstract

The objective of the research described in this thesis is structural characterization of molecular electronic devices and investigation of their compatibility with widely use conventional microelectronics. Back-side spectroscopy was performed to probe organic molecular later integrity at buried interfaces, during and after fabrication. Modifications of optically transparent substrates with organic molecules were achieved using ultrathin Ti as a primer, which then spontaneously reduced aromatic diazonium ions in solution to form free radicals. The free radicals then bond covalently to the substrate. Then, a second conducting contact was deposited by direct physical vapor deposition onto the molecular layer. The molecular layer integrity was probed by "back-side" Raman and infrared spectroscopy. The results demonstrated that metal deposition had minimal influence on molecular layer structure.

The compatibility of carbon based molecular junctions with various microfabrication processes such as elevated temperatures, photolithographic processing and metal deposition was investigated. Flat carbon surfaces were modified electrochemically by reduction of aromatic diazonium ions. The aromatic molecules bond covalently to the electrode though strong C-C bonds. Then the top metal contact was deposited to form a complete junction. Molecular layer integrity after deposition of various metals was inspected by "back-side" spectroscopy. Both Ti and Pt metals caused significant damage to the molecular layer, while Au and Cu had no observable effect on the molecular layer. The modified samples were thermally stable up to 400 ^{o}C and the complete junctions

were stable up to 250 °C under vacuum. Carbon based molecular junctions were compatible with a photolithographic process and different solvents used during the process.

The charge transport mechanism through silicon based molecular junctions was investigated by replacing carbon of previous investigations by a Si electrode. Heavily doped n- and p-Si (111) substrates were modified electrochemically with aromatic molecular layers and Cu contact was deposited, resulting in reproducible junctions with high yield. The junctions were characterized spectroscopically and electrically. Junctions made with n-Si exhibited significantly higher conductivity than those made with either p-Si or carbon substrates. This difference in conductivity was attributed to difference in the barrier height for tunneling as estimated from ultraviolet photoemission spectroscopy measurements.

Acknowledgement

First and foremost, I would like to thank God “Allah” for bestowing me with the grace of science and knowledge. I hope that this grace would be useful for others.

Second, I would like to express my deep gratitude and thankful for my supervisor Prof. Dr. Richard L. McCreery, for accepting me in his group and offering me such a great opportunity. Furthermore, I would like to thank him for his support, advice, patient and guidance all the way during my PhD research from my first day in the laboratory to thesis writing. I would like also to thank him for his group meetings that were the first step to learn how to conduct scientific research. I have earned a lot from his discussions, interpretations, corrections, suggestions and knowledge. Last but not least, I would like to thank him for his social gather of the group members and thank his wife Jane.

Third, I would like to thank the present and past group members in Prof. McCreery group, I was fortunate to work in such a collaborative environment. In particular, I would like to express my gratitude to Dr. Adam Johan Bergren for his help, time, advice and effort that helped me a lot to accomplish my thesis. In addition, I would like to thank Dr. Haijun Yan, Dr. Andrew Bonifas, Jie Ru, Dr. Jing Wu, Dr. Lian Shoute, Dr. Kenneth Harris, Dr. Fengjun Deng, Dr. Nikola Pekas, Dr. Rajesh Kumar and Dr. Rajesh Pillai for their helpful scientific discussions and support. In addition, I would like to thank Bryan Szeto, for his friendship and support in training me a lot of microfabrication skills and his

technical help. Furthermore, I would like to thank Dr. Sayed Nagy for his friendly and scientific support and help.

Fourth, I would like to thank people who directly support me to perform my experimental work: National Institute for Nanotechnology staff, University of Alberta NanoFab staff, University of Alberta ACSES staff especially, Dr. Dimitre Karpuzov, machine and glass shop staff. The department of chemistry graduate coordinators and the complete team.

Finally, I would like to thank my mother, my father, my two brothers, my sister, and latest member in my small family, my wife. I would like to thank my unforgotten friends here in Canada and Egypt for their unusual and special support that was essential during my PhD. I thank the Egyptian Student Association, the members of the department of analytical chemistry at faculty of pharmacy in Cairo University. Thanks all

Table of Contents

DEDICATION

ABSTRACT

ACKNOWLEDGEMENT

TABLE OF CONTENTS

LIST OF TABLES

LIST OF FIGURES

LIST OF ABBREVIATIONS

List of Tables

Table Page

List of Figures

List of Abbreviations

AFM	Atomic force microscopy
ATR	Attenuation total reflection
BOE	Buffer oxide etch
CCD	Charge coupled device
CP-AFM	Conductive probe- atomic force microscopy
CV	Cyclic voltammogram
DAQ	Data acquisition
E-GaIn	Eutectic mixture of gallium-indium
FTIR	Fourier transform infrared
HDPE	High density polyethylene
HOMO	Highest occupied molecular orbital
IETS	Inelastic electron tunneling spectroscopy
ITO	Indium tin oxide
LB	Langmuir-Blodgett
LOFO	Lift-off float-on
LUMO	Lowest unoccupied molecular orbital
MCBJ	Mechanically controllable break junction
MTR	Multiple transmission reflection IR
NAB	4-Nitroazobenzene
NAB DS	4-Nitroazobenzene 4’-diazonium salt
nTP	nanotransfer printing
OTPPF	Optically transparent pyrolyzed photoresist film

p-b IRRAS	*p*-polarized back side infrared reflection absorption spectroscopy
PALO	polymer assisted lift-off
PDMS	polydimethylsiloxane
PEDOT:PSS	poly(3,4-ethylenedioxythiophene)poly(4-styrenesulphonate)
ppb	part per billion
PPF	pyrolyzed photoresist film
QCM	Quartz crystal microbalance
rms	Root mean square
SAMs	Self-assembled monolayers
SDMD	Surface diffusion mediated deposition
STM	Scanning tunneling microscope
STM-BJ	Scanning tunneling microscope based break junction
$TBABF_4$	Tetrabutyl-ammonium tetrafluoroborate
TBAHFP	Tetrabutyl-ammonium hexafluorophosphate
TFMP	Trifluoromethylphenyl
TOC	Total organic carbon
UPS	Ultraviolet photoemission spectroscopy
UV-vis	Ultraviolet-visible
WF	Work function
XPS	x-ray photoelectron spectroscopy

Chapter 1

Introduction

1.1 Molecular Electronics

Miniaturization of solid state electronic devices commenced by introducing silicon based integrated circuit technology in 1958*[1]*. Since then, solid state electronic devices are becoming more and more dense due to advances of science and technology, especially advances in microfabrication technology. One of the early motivations for the development of molecular electronics was continuation of miniaturization of electronic devices down to the molecular and atomic scale.

The concept of employing a “single” organic molecule’s intrinsic properties to actively control the charge transfer within electronic devices was first proposed by Aviram and Ratner in 1974*[2]*. By controlling charge transport, organic molecules can, in principle, perform functions such as rectification, molecular switching, negative differential resistance, and charge storage in electronic devices*[3]*. In addition to the production of densely packed electronic devices, molecular electronics offers potential benefits such as faster operational speed and lower power consumption and production cost. Furthermore, the diversity of organic molecules is another advantage; there are millions of organic molecules with various structures and electronic behaviors. This diversity in structure can lead to novel electronic behavior in comparison to traditional Si electronics. In addition to controlling charge transport, organic molecules may function as sensors or even bio-sensors by incorporation of biomolecules (such as proteins) into molecular junctions to operate as both conductors and bio-sensors*[4]*.

To achieve practical molecular electronics there are significant fundamental, experimental and fabrication challenges*[5]*. For instance, it is essential to study how the intrinsic properties of organic molecules can control and affect the charge transport between two conducting electrodes. Such studies are the initial steps towards designing and synthesizing organic molecules which when incorporated into a device produce desirable electrical characteristics *[5]*.

Moreover, the fabrication challenge of integrating soft organic molecules into the relatively harsh fabrication processes used in modern microelectronic manufacturing is critical for the emergence of molecular electronics in practical form. Failure to integrate laboratory paradigms with current microfabrication process will confine molecular electronics to laboratory research. Such integration will require molecular devices with good thermal stability, compatibility with materials used in semiconductor processing, plus high device yield and reproducibility.

In addition, it is often desirable to perform spectroscopic characterization of organic molecules buried within complete molecular electronic devices. This characterization is important to determine if any chemical and/or physical damage of the organic molecules occurred during device fabrication. Furthermore, spectroscopic measurements provide fundamental understanding of charge transport through molecular electronics, in some cases while the devices are operating.

Molecular electronic junctions consist of a layer of organic molecules of interest attached to contacting electrodes as shown in Figure 1.1. The interface between the molecule and the contact has an important role on controlling the degree of charge conduction through a molecular junction. Various experimental platforms have been used to examine the electrical properties of organic molecules in molecular electronic junctions, and are often classified according to the number of molecules under investigation into "single molecule" or "ensemble" devices.

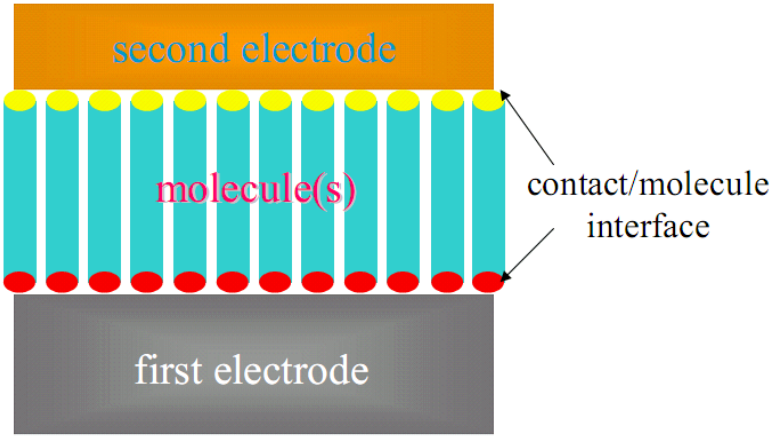

Figure 1.1. Scheme for elements of molecular electronic junction, the two conductive electrodes and the molecule(s) confined between the electrodes.

There is a significant variability of molecular conductivity among various experimental platforms, even for the commonly studied case of an alkane mono- or dithiol bonded to a gold surface. There is about an eight order of magnitude range in the observed conduction among various experimental platforms. This difference in conduction reflects the complexity and importance of the contact/molecule interface and how the nature of the interface has a large effect on the electrical behavior of the molecular junction*[6]*. In addition, yield and reproducibility are major challenges facing molecular electronics, resulting in serious uncertainty when comparing devices from different laboratories.

The next sections describe the fabrication of molecular electronic junctions, starting with techniques of attaching molecules to the electrode surface. Then, various experimental platforms developed to study molecular junctions will be introduced and challenges and issues with the top contact fabrication will be highlighted. Finally, the electrical and spectroscopic measurements of molecular junctions will be described. It should be noted that this discussion is not comprehensive and for each section there are reviews that have been published in more detail *[6-13]*.

1.2 Contacting the Molecules to Electrode Surface

Many modification techniques of inorganic substrate surfaces with organic molecules have been developed during the last four decades. Surface modification provides a method to control the substrate's chemical or physical characteristics. Modifications of both conductive and non-conductive substrates have been subjected to extensive studies for applications in various fields, such as solar energy conversion*[14-16]*, catalysis*[17]*, biosensing*[18-21]* and molecular electronics*[7, 13, 22]*. Depending on the nature of the interaction between the substrate and the organic molecule, the substrate surface can be modified through either physisorption or chemisorption of the organic molecule.

The first step in fabrication of a complete molecular electronic junction is bonding the organic molecular layer to a conductive electrode surface. In the next section, some of the common methods of surface modification used in molecular electronics will be briefly discussed.

1.2.1 Langmuir-Blodgett (LB) films

When amphiphilic molecules are dissolved in aqueous solution, the molecules will orient to form a Langmuir monolayer at the water/air interface, where the hydrophilic portion (head) will be immersed in the aqueous layer and the hydrophobic portion (tail) will be suspended in water/air interface. The Langmuir monolayer can be transferred mechanically to a planar solid surface while conserving its orientation and order, thus forming a Langmuir-Blodgett (LB) film on the surface as shown in Figure 1.2. LB films have the advantage of being ordered and various molecules can be used (as long as they have the ability to order on the surface as a Langmuir monolayer). Molecular multilayers may be constructed through repetition of the mechanical transfer process. Although the technique is very simple, LB films require planar substrates and are sensitive to environmental contamination. Another major disadvantage is that the LB film is physisorbed onto the substrate surface through weak electrostatic interactions. As a result of this weak bond, an indirect deposition technique was developed to prevent damaging of the LB during Au top contact deposition onto the LB molecular layer*[23]* as discussed below. In addition, the fact that the molecules are physisorbed on the surface makes the LB process less suitable for the fabrication of robust and stable molecular electronic devices.

1.2.2 Self-assembled monolayers (SAMs)

The term self-assembled monolayer (SAM) is used to describe the spontaneous process of adsorption and organization/orientation of organic molecules onto a substrate surface to form a two-dimensional monolayer*[24]*. The organic molecule possesses a surface-active head group that interacts with and assembles on the substrate surface as shown in Figure 1.3. The phenomenon of self-assembly is not limited to an organic molecule/solid interface, and can occur also in solution between organic molecules to create supramolecular self-assembled architectures*[25]*. Many organic molecules have been studied as examples of SAMs, such as long chain fatty acids (alkanoic acids) adsorption onto aluminum oxide*[26, 27]* and silver*[28]*, and organosilane derivatives chemisorbed on various hydroxylated surfaces such as SiO_2*[29, 30]*, quartz*[31]*, glass*[29]*, aluminum oxide*[32]*, indium tin oxide (ITO)*[14, 33]*, zinc selenide*[29, 32]* and Pt oxide*[34, 35]*. Organosilanes can also form SAMs on elastic substrates such as polydimethylsiloxane (PDMS) after surface activation to manipulate surface properties*[36]*. Surface modification by organosilane is very sensitive to environmental conditions such as moisture content and temperature*[24]*.

The assembly of organosulfur (thiolate) molecules onto metal surfaces has been widely studied since the first paper reported adsorption and assembly of a disulfide on a gold substrate*[37]*. Adsorption of thiolates to form SAMs has been studied on various metals, including Au, Ag, Cu Pt and Hg. The thiol molecules adsorb on the metal surface within a few seconds and then undergo a process of organization and orientation to produce a densely packed two-dimensional organic monolayer. The binding energy of Au-S bond is about ~50 kcal/mol*[38]*, so the thiolate molecules are mobile on the Au surface and can pack to a minimum-energy configuration. Self-assembled monolayers have significant advantages as surface modification techniques, such as preparation simplicity, no need for special equipment or a planar surface*[38]*. Many platforms for studying the charge transfer in molecular electronic junctions are based on SAMs of thiols on Au as discussed below*[39-41]*. One major problem with the use of SAMs in practical molecular electronic devices is thermal stability. The electronic behavior of SAM-based molecular junctions changes irreversibly for temperatures above 50 ^{o}C, thus limiting their practical operating temperature range *[42]*.

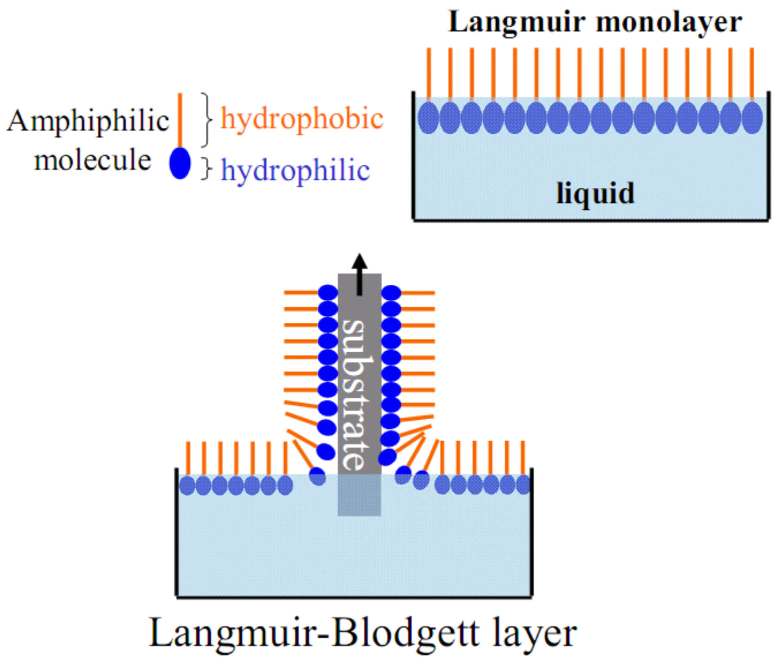

Figure 1.2. A scheme for the Langmuir monolayer formation at a liquid/air interface (top figure) and transfer of the monolayer from the solution to the substrate to form a Langmuir-Blodgett (LB) monolayer film (bottom figure).

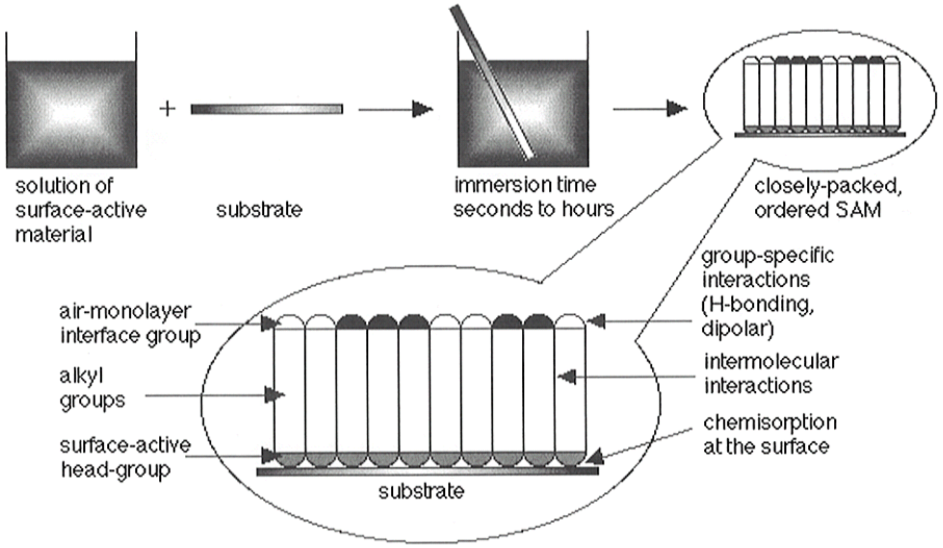

Figure 1.3. Formation of self-assembled monolayer (SAM) on a substrate immersed into surface active material solution. (Reprinted with permission from reference *[24]*. Copyright 1996 American Chemical Society)

1.2.3 Electrochemical Modification

Electrochemical modification of a conducting surface occurs via electron transfer between the substrate and organic molecules in the solution, which leads to covalent attachment of the molecules to the substrate surface. Surface modifications by electrochemical method have been performed through oxidation or reduction of selected organic molecules, and are not limited to a single functional group, thus enabling bonding of a large number of interesting molecules to the surface. Grafting various molecules through oxidation has been reported via oxidation of aliphatic amines*[43-46]*, oxidation of carboxylate to modify carbon surfaces*[47, 48]*, oxidation of alcohols*[49, 50]* and Grignard reagents*[51, 52]*. Electrochemical reduction of molecules has been applied also, such as electrochemical reduction of vinyl groups*[53, 54]* or aromatic diazonium ions*[55-61]*. More about aromatic diazonium salt chemistry will be introduced in the next section, as it is the main surface modification technique utilized in the next three chapters.

1.2.3.1 Aromatic Diazonium Salt Chemistry

Electrochemical surface modification by reduction of aromatic diazonium salts was first reported on carbon surfaces by Pinson and co-workers *[57, 58]* in 1992. This modification technique has since been used to modify various substrates such as Si*[55, 62-66]*, GaAs*[67]*, Cu*[68]*, Au*[69]*, Al*[68]*, Fe *[70-72]* and Ni*[71]*. Diazonium chemistry can also modify various oxides such as ITO*[73]*, SnO_2*[71]* and TiO_2*[74]*. The reduction process of diazonium salt can occur spontaneously when the substrate surface has enough reducing power*[67,* *75, 76]* providing a facile and simple method for modification with no need for electrochemical instruments.

The electrochemical reduction of aromatic diazonium ions on carbon electrodes results in covalent modification of the carbon surface through a strong C-C bond (~80-100 kcal/mol)*[7]*. The mechanism of surface modification starts by electron transfer from the substrate to reduce the aromatic diazonium ion, followed by production of N_2 and aromatic free radicals. The free radicals attack the surface and form a covalent bond*[77]* as shown in Figure 1.4a. Another mechanism was proposed*[55]* for electrochemical surface modification of H-terminated Si with diazonium ion to form strong Si-C bond (~ 4 eV or ~ 80-100 kcal/mol)*[13]*. A scheme summarizing the modification steps is shown in Figure 1.4b.

Electrons tunneling through an initial aromatic molecular monolayer can sustain the electrochemical reduction of diazonium salts, thus generating more free radicals that attack the first molecular layer and lead to formation of a molecular multilayer*[76, 78-80]*. The organic molecular multilayer thickness can be controlled by adjusting the electrochemical reduction parameters*[79]*.

1.2.4 Additional Methods for Si Surface Modification

Several methods have been applied to modify the H-terminated Si surface by organic molecular layers*[81, 82]*. For example, thermal activation has been used to initiate the modification of H-terminated Si by decomposition of diacyl peroxides, which results in free radical formation and covalent modification of the Si surface through formation of a Si-C bond*[83, 84]*. Alkenes and alkynes have been grafted onto the H-terminated Si surface through thermal activation, the reaction resulted in formation of Si-C bond*[85]*. Furthermore, thermal activation of alcohols and aldehydes was used to directly bond them to a Si surface through formation of Si-O-C bond*[86]*. Photoactivation has been employed to initiate the reaction between aldehyde molecules and H-terminated Si surface. The reaction resulted in attachment of the aldehyde molecule to Si through a Si-O-C bond*[87]*.

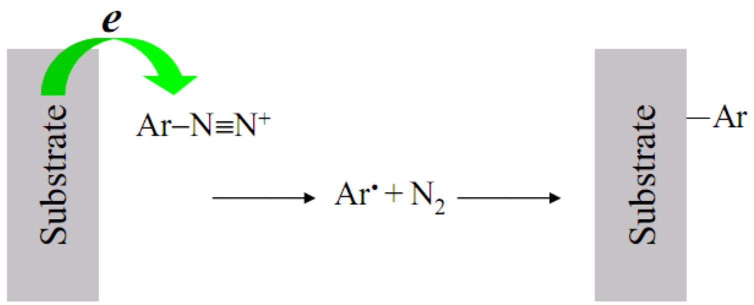

<u>Substrate</u>: C, metal or semiconductor

Figure 1.4a. General scheme for substrate surface modification by electrochemical reduction of aromatic diazonium ion (Ar-N≡N$^+$), which produces an aromatic free radical that bonds to the surface.

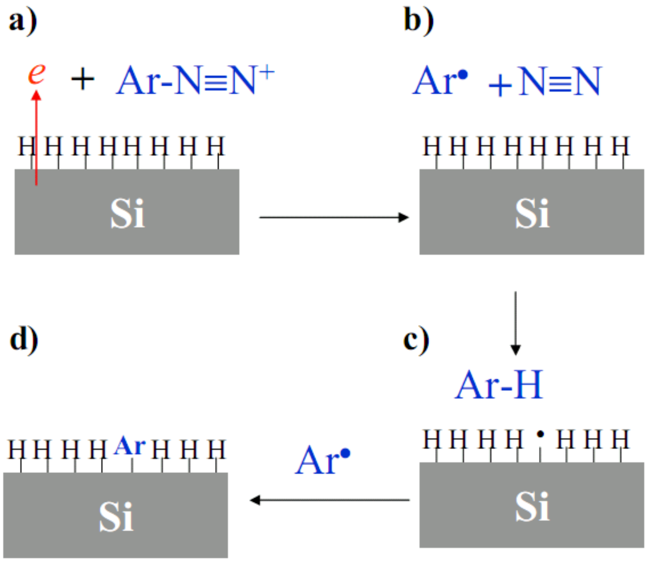

Figure 1.4b. Scheme for surface modification of H-terminated Si by electrochemical reduction of aromatic diazonium ions (Ar-N≡N$^+$). a) reduction of diazonium ion. b) Formation of aromatic free radical and N_2. c) Abstraction of H from Si surface by the free radical and formation of dangling bond on Si surface. d) Reaction between aromatic and Si free radical and formation of Si-C bond.

1.3 Platforms to Study Molecular Layer Electrical Properties

Investigating the molecular layer electrical characteristics was pursued through several experimental platforms. These platforms can be divided broadly into two categories according to the number of molecules under investigation: platforms that measure a “single” or few molecules and platforms that measure ensembles of millions molecules oriented between two conducting “contacts”.

1.3.1 “Single” Molecular Electronic Junctions

Scanning probe techniques*[6, 10]* such as scanning tunneling microscopy (STM) and conductive probe atomic force microscopy (CP-AFM)*[88]* and molecular break junctions (either mechanically controlled or electromigration break junctions) have enabled the measurement and study of the electrical properties of single molecules or collections of a few (<100) molecules. The electrical measurement of an isolated single molecule provides information about how molecular orbitals control charge transport while reducing or eliminating the intermolecular electronic interactions possible in the case of molecular ensembles *[12]*.

1.3.1.1 Scanning Tunneling Microscopy

The scanning tunneling microscopy technique with its atomically sharp tip can achieve high spatial resolution to manipulate and measure the electrical characteristics of single/few molecules. STM measurements can be operated in either constant current mode (tunneling current kept constant and surface topography is recorded) or constant height mode (change in current is recorded at different surface positions) or a combination of both. In STM measurements, the molecules are either physisorbed or chemisorbed onto a conductive bottom electrode, and the STM tip acts as the top electrode. A bias is applied between the bottom electrode and the STM tip and the tunneling current is recorded to probe the molecular layer conductance, as shown in Figure 1.5. Although STM technique is capable of measuring a single molecule, the position of the STM tip cannot be accurately assigned for a single molecule in a densely packed two-dimensional self-assembled monolayer. To overcome that, a conductive molecule (conjugated aromatic thiolate) is embedded into an insulating self-assembled monolayer of alkanethiol*[89],* where higher conductivity was assigned for a single aromatic molecule conduction. STM has the ability of measuring huge numbers of molecular electronic junctions just by moving the tip, which results in large set of data that can be analyzed statistically. A major disadvantage of STM technique is the distance between the molecule and the STM tip is not accurately defined, so the current change can be due to a change in molecular conduction or simply a change in height.

STM based break junction (STM-BJ) is a method to create molecular junction repeatedly by moving an STM tip into and out of the substrate electrode in the presence of the molecule of interest*[10, 90-91]*. The method has the advantage of measuring large number of molecular junctions in short time and creating a conductance histogram. The conductance histogram is used to identify single molecule conductance as shown in Figure 1.6.

1.3.1.2 Conducting Probe Atomic Force Microscopy [CP-AFM]

In conducting probe AFM measurements, the tip is coated with a metal and placed in direct contact with the molecular layer assembled onto a conductive electrode surface. A bias is applied between the CP-AFM tip and the bottom electrode and current through molecules is measured as shown in Figure 1.7a. The technique is relatively simple and coating the AFM tip with different metals enables the study of the effect of changing top contact work function on conduction through molecular electronic junctions*[92]*. The spatial resolution of CP-AFM is lower than STM because the AFM tip is much larger than atomic scale, resulting in uncertainty in the number of molecules probed by the AFM tip. One method to avoid this issue is using metal nanoparticles of known size so the number of molecules under investigation can be estimated, but it also raises a problem of contact resistance between the metal nanoparticle and AFM tip. Another issue to be considered during analysis of the data is dependence of current on the force applied by the AFM tip and the possibility of molecular layer deformation.

In another CP-AFM study, the effect of the molecule/electrode interface was investigated by comparing conduction of alkane monothiols to alkane dithiol molecules of the same length using Au-, Ag- and Pt-coated AFM tips*[93]*. The contact resistance of alkane dithiol molecules was 1-2 orders of magnitude lower than alkane monotiol molecules as shown in Figure 1.7b. This observation was attributed to the ability of alkane dithiols to form metal-S bonds with the Au AFM tip, while alkane monothiol cannot. This result shows the importance of bonding between electrode and molecule to the observed molecular conduction*[93]*. The dependence of charge conduction mechanism on the length of the conjugated molecular layer was studied by AFM tip *[94]*. The data showed that the dominant mechanism of charge transport was tunneling for a molecular layer thickness of ~ 4-5 nm, then a transition from tunneling conduction to hopping conduction was observed for molecular layer thickness over 4-5 nm*[94]*.

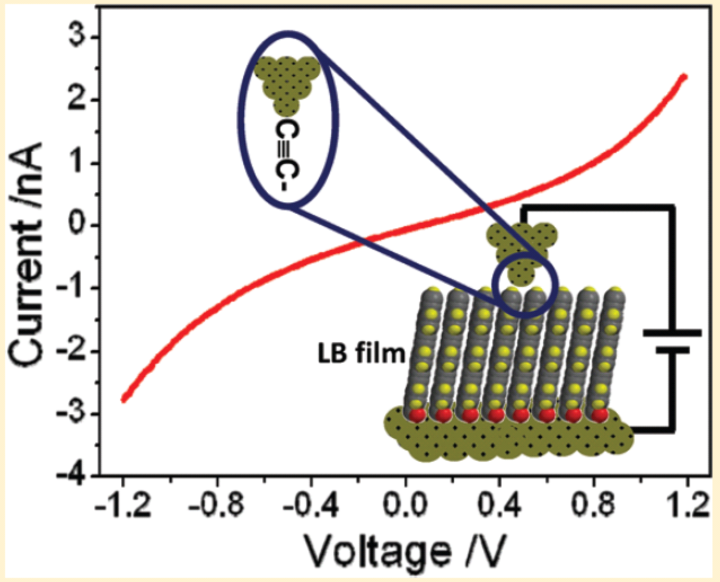

Figure 1.5. Electrical characterization of Au/LB monolayer by STM tip (Reprinted with permission from reference*[95]*. Copyright 2012 American Chemical Society)

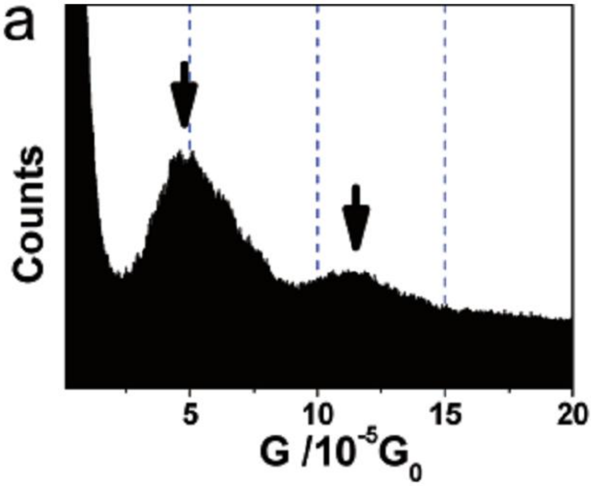

Figure 1.6. Conductance histogram of alkane dithiol (8 carbons) molecule from ~10,000 measurements by STM BJ method. Black arrows mark conductance peak of one and two molecules. (Reprinted with permission from reference *[90]*. Copyright 2007 American Chemical Society).

1.7a

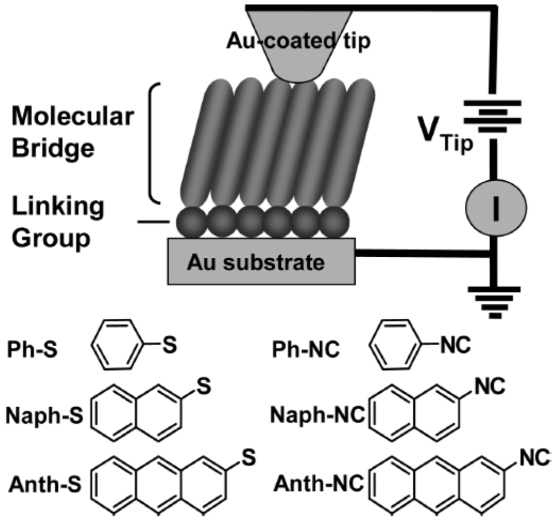

1.7b

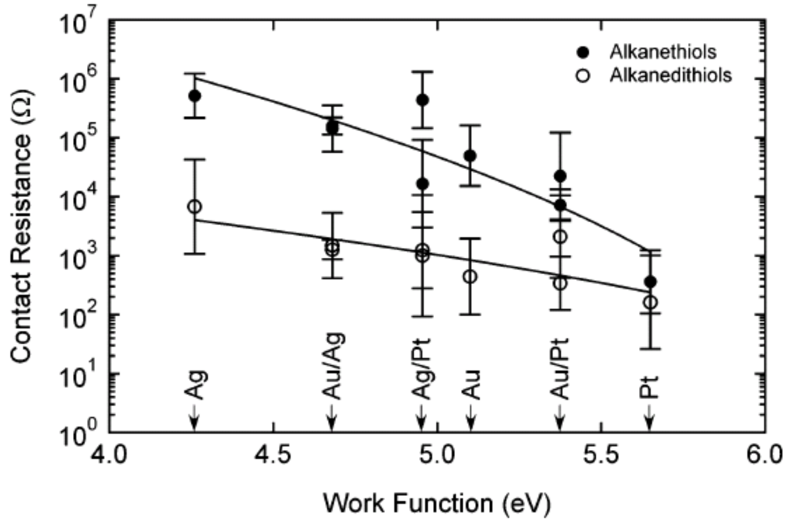

Figure 1.7 A). Formation of Metal/Molecule/Metal molecular electronic junction using Au coated conducting probe AFM tip (Reprinted with permission from reference*[96]*. Copyright 2000 American Chemical Society)
B). Comparison of contact resistance of alkane monothiol and alkane dithiol probed by AFM tip coated by various metals (Reprinted with permission from reference*[93]*. Copyright 2004 American Chemical Society)

1.3.1.3 Mechanically controllable break junctions

The mechanically controllable break junctions (MCBJ) technique was initially designed to study the tunneling behavior of superconductors*[97]*. This technique was then introduced by Reed and co-worker to study the charge conduction through molecular electronic junctions*[98]*. During the MCBJ experiment, a metal filament or notched wire is fixed on insulating layer (e.g. polyimide) attached to bendable substrate “bending beam”. Then the insulating layer is etched under the metal to form a freely suspended metal bridge. The nanogap is formed by mechanically bending the substrate using a piezoelectric controlled pushing rod in z-direction as shown in Figure 1.8. Then the molecules are chemisorbed on the metal to form the molecular junction, in sole cases with a single molecule bridging the nanogap*[98]*. The nanogap distance can be defined precisely through piezoelectric control. Another advantage of MCBJ is the ability to repeat the bending process and collect a large number of measurements to obtain statistical evidence of single molecule conductance. Although the distance between the two electrodes can be controlled, the electrode shape and configuration cannot be controlled (surface is not smooth and flat), and so molecule/electrode contact is not well defined.

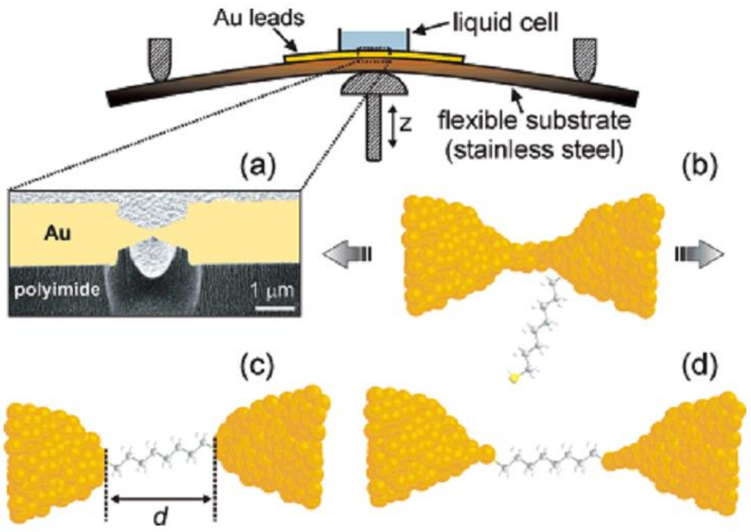

Figure 1.8. Scheme for MCBJ and SEM image of one Au junction. A) is the fabrication process with magnified image of the beak junction. B) Continuous Au film before breaking. C and D) Various orientation of the molecules between Au contacts. (Reprinted with permission from reference*[101]*, Copyright 2006 American Chemical Society)

1.3.1.4 Electromigration break junctions

Electromigration break junctions are formed by passing a high electrical current through a metal nanowire. This current leads to electromigration of the metal and breaking of the nanowire and formation of a tunneling gap of 1-2 nm*[99, 100]*. Once the nano-gap is formed, it cannot be altered by the applied current. Therefore, each nanogap has its own unique shape and length. Consequently, the molecular junctions that are formed by modifying the nanogaps have diverse junctions’ length and metal/molecule interfaces.

1.3.1.5 Crossed-wire tunnel junctions

A crossed-wire tunnel junction is formed from crossing two metal wires (10 μm in diameter), one of which is modified with a self-assembled monolayer*[102]* as shown in Figure 1.9. The metal wires are mounted on a test stage perpendicular to each other. A magnetic field is applied perpendicularly to the modified wire, and upon passing DC current in the wire it deflects and the spacing between the two wires is controlled by Lorentz force. The deflection current is increased slowly to bring the two wires in contact, thus forming a molecular junction containing about ~ 10^3 molecules.

1.3.1.6 Surface diffusion mediated deposition

The surface diffusion of metals towards modified conductive electrode permits the electrical characterization of junctions consisting of 1-10 molecules*[103]*. The resulting measurement of alkane layer conductance showed exponential dependence of current on molecular length and also decay constant β of 0.9 per (-CH_2-) group*[103]* as shown in Figure 1.10. The diffusion of metal is also considered as “soft” nondestructive deposition of top contact as discussed below.

1.3.2 “Ensemble” molecular electronic junctions

Ensembles of molecules (~ 10^3 to 10^{12} molecules) are adsorbed on the first electrode and then a second conducting electrode is used to probe their electrical behavior. Experimental platforms such as cross bar junctions, hanging Hg drop electrode and nanopore junctions have been used to fabricate and characterize molecular ensemble junctions. Several paradigms have the potential of integration with the current fabrication processes as discussed below*[7, 39, 40]*. However, the intermolecular electronic interactions complicate data interpretation and theoretical modeling. Paradigms that measure ensembles of molecules will be discussed in the next section, classified according to the method of top contact formation.

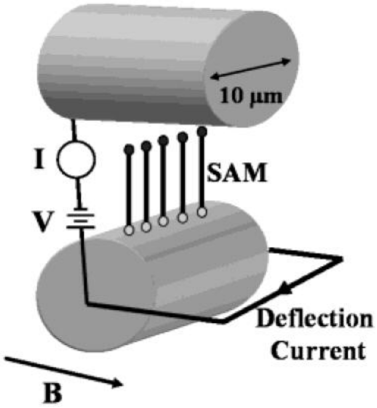

Figure 1.9. Scheme representing crossed wire tunnel junction, one wire is modified with SAM, and the other wire is perpendicular to it. (Reprinted with permission from reference*[102]*, Copyright 2002 American Chemical Society).

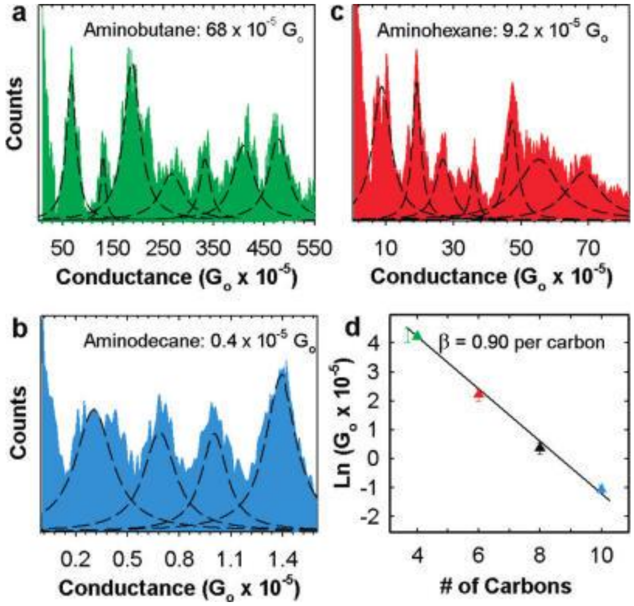

Figure 1.10. Conductance measurement of homologous series of “single“ or few alkane molecules connected to carbon electrode & contacted by metal diffusion to form the other contact (Reprinted with permission from reference*[103]*. Copyright 2011 American Chemical Society).

1.4 Top Contact Formation and Molecular Layer Integrity

In order to successfully fabricate ensemble molecular electronic junctions, the organic molecular layer should be connected electrically to the macroscopic world through a permanent top contact*[9]*. The ideal top contact should be permanent, robust, and reproducible and should not damage the molecules either chemically through bond destruction or physically through penetrating and disturbing the molecular layer, possibly forming a metal/metal short circuit. In addition, the top contact should be electrically conductive so that the observed current is a function of the molecular layer characteristics and not the top contact itself. The methods used to fabricate top contacts in ensemble junctions are summarized below as “direct” deposition involving vapor deposition directly onto a molecular layer, and “soft” or “indirect” methods designed to minimize disturbance of the molecular layer.

1.4.1. Direct Metal Top Contact Deposition

Direct physical vapor deposition of metals has been used as a fabrication step to make electrical contact with the molecular layer bonded to a conducting substrate. During direct metal evaporation, the metal is heated under vacuum either by an electron beam or thermally to evaporate the metal. Then the evaporated metal atoms are condensed onto the molecular layer to form a metal contact. Although the technique is appealing because it is currently used in microelectronics fabrication and possesses massively parallel fabrication capability, many studies reported molecular layer damage during direct metal deposition and attributed the damage to the high temperatures and kinetic energy of the metal atoms as well as to radiation emitted from the heated source*[104]*. Molecular layer integrity has been studied after direct evaporation of various metals, including Al, Cu, Ag, Ti and Au. Metals have been deposited on the top of Au substrate modified with SAMs of alkylthiol molecules*[105-110]* and SAMs of mono- and dithiol conjugated molecules*[111, 112]*. Metals were reported to penetrate and/or destroy the alkythiol SAMs to different degrees depending on the metal deposited*[106]*, molecular layer structure*[107]*, terminal head group*[105]*, and packing density*[106]*. It was reported that Ti atoms cause complete destruction of a conjugated molecular layer*[111, 112]* and formation of Ti-C bonds*[112]*, while Au atoms penetrate the conjugated molecular layer to result in metal-metal short circuits*[111, 112]*.

In addition, it was observed that the terminal head group of the organic molecular layer can have important role in controlling metal diffusion through the molecular layer. For example, it was demonstrated that a SAM with a terminal thiol group (dithiol) could reduce Au atom penetration into the molecular layer*[105, 111]*. Even a short, thiol-terminated propylsilane assembled on Si/native SiO_2 is able to block Au diffusion into the molecular layer*[113]*. Another example is the control of Al penetration by a methoxy terminated thiol*[106, 107]*.

This penetration and/or damage were not limited to SAMs on Au substrate. An alkyl molecular monolayer that was covalently bonded to a Si surface exhibited metal penetration and/or molecular layer damage during direct metal deposition*[114-116]*. Complete destruction of an aromatic molecular monolayer by direct evaporation of Au was observed in another spectroscopic study *[66]* as shown in Figure 1.11.

In the case of a carbon surface modified by diazonium reduction, the direct evaporation of Cu metal has been used to fabricate reproducible and high yield (over 90%) carbon based molecular electronic junctions. The molecular layer integrity was investigated with spectroscopic methods*[117, 118]*, and more investigations are presented in Chapters 2 and 3. As described later the stability of diazonium-derived molecular layers on carbon surfaces is likely due to their strong C-C surface bond.

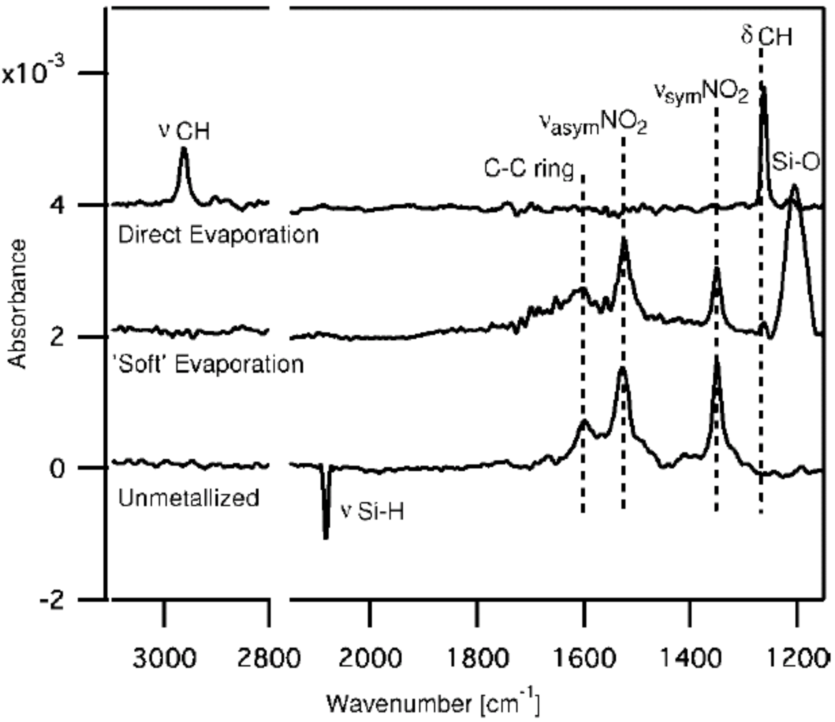

Figure 1.11. FT-IR spectra of aromatic molecular *monolayer* (nitrobenzene) covalently attached to Si substrate. Bottom spectrum: Molecule/Si surface initially. Middle spectrum: molecular layer after "soft" deposition of Au. Top spectrum: after "direct" deposition of Au metal as top contact. (Reprinted with permission from reference *[66]*. Copyright 2008 American Chemical Society)

1.4.2 Indirect, or “Soft” deposition Techniques

1.4.2.1 Soft Liquid Contact

Many techniques have been investigated to make nondestructive contact with the organic molecular layer to fabricate complete molecular electronic junctions*[8]*. Conductive liquid contacts such as Hg*[119-121]* and eutectic mixture of Ga/In (eGaIn)*[122-125]* have been used to make a “soft” top contact with molecular layer, usually by lowering a drop of liquid metal onto a molecular layer. Although such techniques helped to understand charge transport mechanisms*[120]* and reproducible results have been reported, liquid metal techniques are not practical for commercial device manufacturing and are restricted to laboratory research. In addition, there is uncertainty regarding the presence of impurities and oxides at the metal/molecule interface.

1.4.2.2 Indirect Physical Vapor Deposition

Indirect evaporation of metals was developed to minimize metal penetration into the organic molecular layer and/or damage during deposition*[23, 104, 126, 127]*. During indirect evaporation, the samples were cooled and positioned away from the metal deposition pathway. In addition, the evaporation chamber was filled with inert gas (Ar) to obtain a pressure of ~2 x 10^{-3} mbar, which permited the inert gas atoms to collide with the metal atoms. Thus, the metal atoms lose most of their kinetic energy before reaching the sample surface*[8]* as shown in Figure 1.12. The samples were positioned away from the metal vapor pathway in order to avoid heating and damage by radiation from the e-beam source. Molecular layer integrity was investigated after both direct and indirect evaporation*[66, 104, 128]*. In one study, direct deposition of Pd on molecule/GaAs was compared to indirect evaporation, and it was concluded that direct deposition damaged the molecular layer compared to indirect deposition *[128]*. However, the tradeoff of the indirect evaporation method is a much slower metal deposition rate (0.01 nm/s), and inefficient use of metal contact material*[104]*.

1.4.2.3 Nanotransfer Printing (nTP)

Soft photolithographic techniques, such as nanotransfer printing (nTP) *[129]* have been used to fabricate molecular electronic junctions. A stamp was prepared by direct e-beam evaporation of Au on an elastomer layer such as polydimethylsiloxane (PDMS). Then the Au was mechanically transferred from the stamp to organic molecular layer/GaAs to make the top metal contact as shown in Figure 1.13.

1.4.2.4 Spin Coating of conductive polymers

A conducting polymer, poly(3,4-ethylenedioxythiophene)/poly(4-styrenesulphonic acid) (PEDOT:PSS), has been spin coated on top of dithiol SAMs on Au substrate. Au metal was then vapor deposited on top of the polymer to fabricate complete junctions. The polymer was used to prevent metal penetration through molecular layer or through pinholes as shown in Figure 1.14*[39, 40]*. Use of PEDOT:PSS on top of molecular layer resulted in fabrication of molecular junctions with high yield (> 95%) and large areas of 100 μm in diameter*[39, 40]*. The PEDOT:PSS junctions were reported to be stable up to 50 °C*[42]*.

1.4.2.5 Lift-Off Float-On (LOFO)

The basis of the LOFO technique is deposition of a thin metal top contact on a substrate that weakly bonds to the metal (e.g. Au bonded to SiO_2). If strong bond is formed between the metal and substrate, then a sacrificial layer is inserted between the metal and the substrate*[130]*. After that, the metal is immersed in a suitable solvent and lifted off from the substrate surface so the metal floats on a solvent surface. The metal then is transferred to the modified substrate as the top contact to form complete molecular junctions. Problems include repulsion between the substrate and the floating metal that can be reduced if either the substrate of the metal is hydrophobic. In addition, tearing and wrinkling of the metal film can occur. That tearing and wrinkling may be reduced by rapid evaporation of the solvent*[130]*. An improvement of LOFO technique has been demonstrated by combining nanotransfer printing with LOFO, often called polymer-assisted lift-off (PALO)*[131]*. In this technique, a polymer is added between the substrate (or substrate/sacrificial layer) and the metal. This polymer is detached with the metal. The detachment of the metal together with the polymer leads to increased stability of metal contact and prevention of wrinkle formation. This approach has been demonstrated to build large area molecular electronic junctions*[131]* as shown in Figure 1.15.

1.4.2.6 Soft Deposition through Metal Diffusion

A recent study of making soft metal contact with molecules with a comparison to direct evaporation of the same metal has been published,*[103, 132]* and is shown in Figure 1.16. The approach is based on using SiO_2 on top of the modified electrode as a screen to shield the molecules from direct metal evaporation, then metal is deposited on a nearby SiO_2 surface. Rapid thermal equilibration of the deposited metal is followed by diffusion of the metal toward the molecular layer results in a molecule/metal contact. Since the metal diffuses at near room temperature, the molecule is not subjected to energetic metal atoms. The technique also allows single molecule measurements as discussed above.

1.4.2.7 Electrodeposition

Formation of metal top contact on top of the molecular layer through electrodeposition has been studied as alternative to evaporation methods*[133-138]*. The metal ion was adsorbed by complexation onto the SAM/Substrate surface and then electrochemical reduction of the metal was performed. In addition, electrochemical deposition of metals has been used in conjunction with STM and BCMJ to fabricate metal/molecule/metal junctions*[139]*.

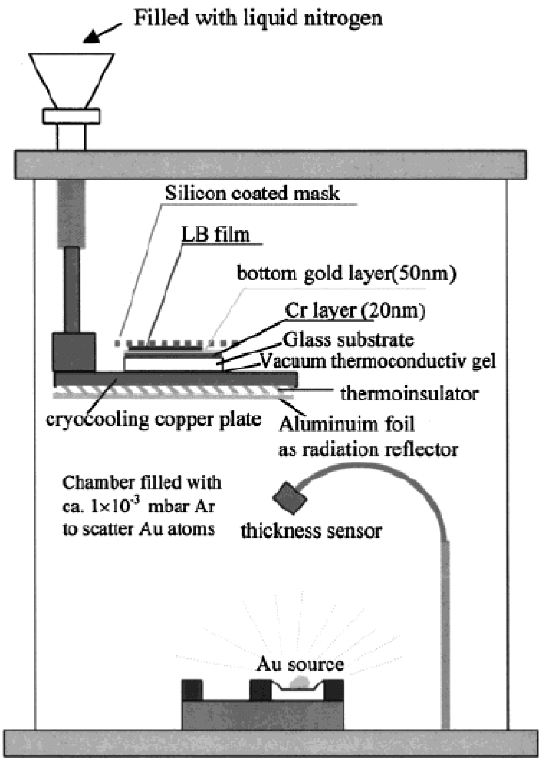

Figure 1.12. Scheme for indirect evaporation of a metal onto organic molecular layer to fabricate molecular electronic junction. (Reprinted with permission from reference *[23]*. Copyright 2001 American Chemical Society)

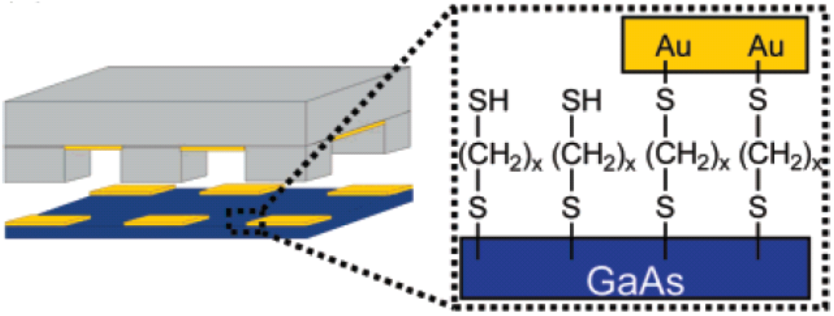

Figure 1.13. Illustration of nanotransfer printing of a metal from PDMS stamp to organic molecular layer to fabricate Au/molecular electronic/GaAs junction. (Adapted with permission from reference *[129]*. Copyright 2003 American Chemical Society).

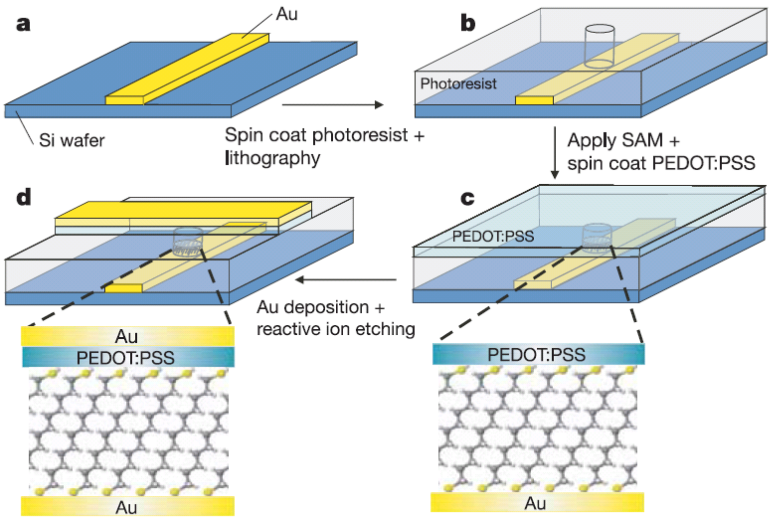

Figure 1.14. Schematic illustration of fabrication steps of Au/PEDOT:PSS/ molecular layer/Au junction. (Reprinted with permission from reference *[40]*. Copyright 2006 Nature Publishing Group).

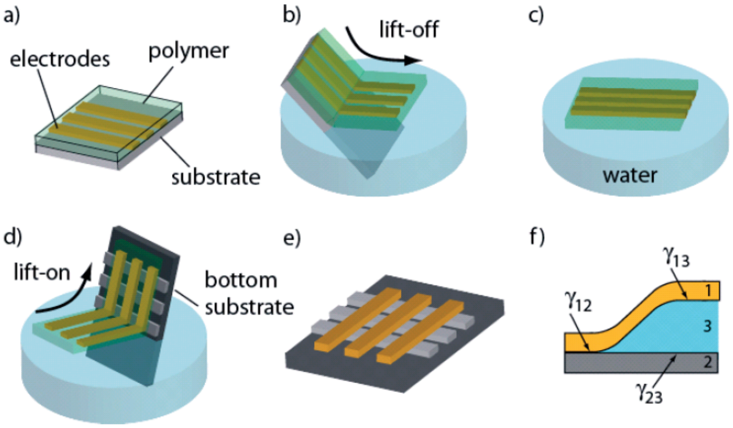

Figure 1.15. Scheme for polymer-assisted lift-off PALO for transfer of metal electrode to modified surface for fabrication of complete junction. a) the substrate/polymer/metal electrode. b) Lift-off process. c) Polymer/metal floating. d) Lift-on process and top contact formation on modified substrate. e) Complete junction. f) Side view of the molecular junction. (Reprinted with permission from reference*[131]*. Copyright 2006 John Wiley and Sons).

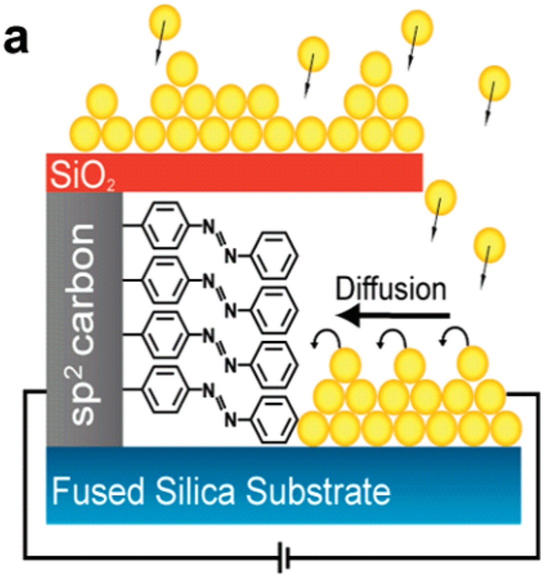

Figure 1.16. Schematic illustration of Au diffusion towards molecular layer during surface-diffusion mediated deposition (SDMD). (Adapted with permission from reference*[103]*. Copyright 2011 American Chemical Society).

1.5 Carbon Based Molecular Electronic Junctions

McCreery and co-workers fabricated cross bar molecular electronic junctions based on a flat carbon as the bottom electrode*[47, 117, 140]*. The carbon electrode is a pyrolyzed photoresist film (PPF)*[141, 142]*. Using a photoresist has the advantage of permitting photolithographic fabrication of carbon structures at micro*[142]* or nano-scale*[143]*. Another advantage of using the photoresist is the ability to dilute the photoresist to fabricate ultra-thin optically transparent carbon electrodes which can be used for spectro-electrochemical studies*[144-146]* and spectroscopic detection of molecules at buried interfaces as discussed below in chapter 3. The photoresist is pyrolyzed at ~ 1000 ^{o}C in presence of hydrogen gas (5% H_2 in N_2 gas). The pyrolyzed photoresist carbon film has a resistivity of (5.1 x10^{-3} ohm.cm)*[142]* which is comparable to glassy carbon. The surface of PPF is very flat with root mean square (rms) roughness determined with AFM of < 0.5 nm*[141]*, which is very important for molecular electronic junctions fabrication, where the roughness of the electrode should be less than the molecular length to prevent short circuit formation. The surface of PPF is covalently modified by organic aromatic molecules through electrochemical reduction of corresponding diazonium salts, which leads to form an irreversible strong covalent C-C bond between the aromatic molecules and PPF (as described in section 1.2.3.1 above). In addition, electrochemical oxidation of aminoalkane molecules have been used to fabricate alkane molecular junctions*[46]*. The Cu metal was directly deposited by electron beam evaporation as top contact to produce a complete molecular electronic junction.

1.6 Characterization of Molecular Electronic Junctions

1.6.1 Electrical characterization of molecular electronic Junctions

Electronic characterization of molecular electronics is performed through collecting current-voltage (*i*-*V*) curves. Besides studying the electrical behavior of the junctions, interpretations of *i*-*V* curves reveal information regarding the mechanism of charge transfer (by studying *i*-*V* behavior at various temperatures) and used to extract contact resistance*[96]*. The simplest method of measuring the *i*-*V* curves is to apply a 2-wire configuration, where a voltage bias is applied to one electrode and current is sensed at the other electrode as shown in Figure 1.17. For accurate determination of current-voltage behavior, the contact and lead resistance should be corrected*[147]*. The electrode and lead resistance can add ohmic potential error (*i*R drop), where the applied voltage bias on the electrode is different from the actual bias at the junction. In this case, a 3-wire configuration should be used where a third probe is used to sense the voltage on the electrode. This third probe detects the actual voltage applied to the junction and corrects for iR losses in the PPF lead and probe contact *[147]*. A 4-wire configuration should be used if it is necessary to correct ohmic potential error at both electrodes, as shown in Figure 1.17.

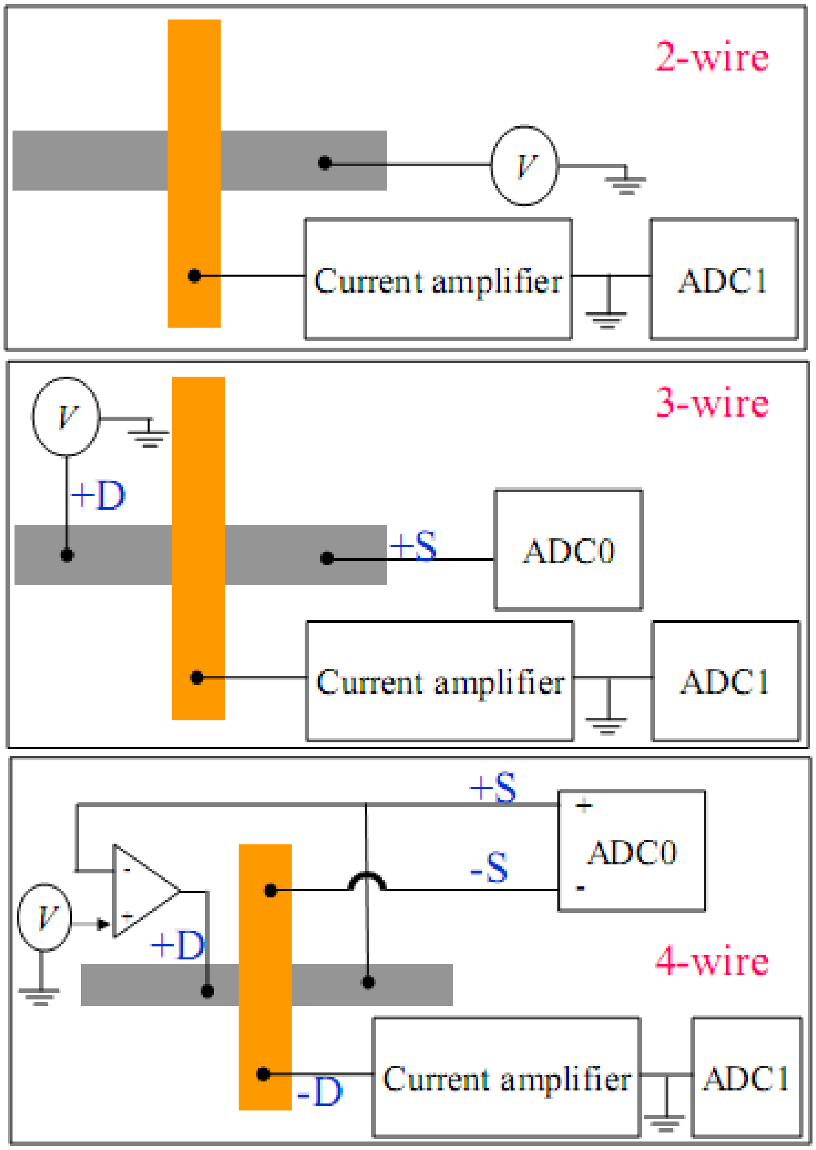

Figure 1.17. Diagrams for 2-, 3- and 4-wire configurations for *i*-*V* curve measurement of molecular electronic devices. *V* refers to the bias voltage; ADC1 represents the analog-to-digital channel for current where ADC0 monitors voltage and has a differential input in case of 4-wire mode. The letters D and S stand for "drive" and "sense".

1.6.2 Spectroscopic characterization of molecular electronic junctions

Spectroscopic characterization of molecular layers within junctions is challenging. First, the molecular layer is ultra-thin (1-10 nm), and a sensitive technique is mandatory to probe such a thin layer. Second, the molecular layer is buried under a top contact that, in most cases, is not optically transparent. As discussed above regarding the formation of metal top contacts, molecular layers can be damaged during fabrication. In-situ spectroscopic characterization of molecular layers provides structural information about the molecular layer during fabrication and while a voltage bias is imposed. Changes in molecular structure may then be correlated with changes in junction electronic properties, to provide insight into charge transport mechanism. Spectroscopic techniques have been used to study molecular layer integrity and molecular changes under bias, such as IR*[66]*, UV-Vis*[148]*, inelastic electron tunneling spectroscopy (IETS)*[65, 113, 149]* and Raman spectroscopy*[117, 118, 150-152]*. In addition, spectroscopic techniques such as ultraviolet photoelectron spectroscopy (UPS) and inverse photoemission spectroscopy (IPES) provide information about the Fermi level of the substrate and HOMO - LUMO position of the molecular layer attached to the surface. Both UPS and IPES spectroscopic data have been utilized to construct energy level band diagram of the modified surface and the results were used to estimate the charge transfer barrier*[41, 92, 119]*.

1.6.2.1 Ultraviolet photoelectron spectroscopy (UPS)

The principle of UPS analysis is the irradiation of a sample with high energy monochromatic radiation (such as helium I line source, 21.2 eV), under vacuum, resulting in emission of an electron from the sample under investigation. The kinetic energy of emitted electrons are recorded and plotted as a UPS spectrum*[153, 154]* as shown in Figure 1.18. Ultraviolet photoelectron spectroscopy analysis can reveal the interfacial electronic states of the electrode substrate, as it detects the occupied electronic state of the sample such as Fermi level E_F of substrate as shown in Figure 1.18. The kinetic energy of the photoelectron (E_K) is the difference between the radiation energy ($h\nu$) and the binding energy (E_b):

$$E_K = h\nu - E_b$$

where h is Plank's constant and ν is the frequency of radiation. So the photoelectron with the maximum kinetic energy E_K^{max} will be emitted from Fermi level excitation, and the work function of the metal can be calculated relative to the vacuum.

In the case of an electrode substrate modified by an organic molecular layer, the photoelectrons are emitted mostly from the organic layer since the technique is surface selective due to the short escape depth of excited electrons*[155]*. In this case, the photoelectron with the maximum kinetic energy E_K^{max} will be emitted from the highest occupied molecular orbital (HOMO) level excitation as shown in Figure 1.18.

The energy offset between the Fermi level of the metal substrate and HOMO of the molecular layer is considered as the tunneling barrier height for hole transport (ϕ_{h+})*[96]*. The calculations of barrier height for charge transfer allow investigating the correlation between the molecular structure and charge transport in molecular electronic junctions.

1.6.2.2 Inverse photoemission spectroscopy (IPES)

IPES involves a beam of electrons of known kinetic energy directed at the sample surface. The electron kinetic energy may be a single value or a range (0-20 eV). Those electrons will occupy the empty energy level in the substrate and radiate the excess energy in the form of photons that collected by the detector and IPES spectrum is obtained*[154, 156-158]*. IPES is used to study the unoccupied/empty electronic states in solid substrates surfaces*[157, 159, 160]*. For substrate surfaces modified with organic molecules, the IPES data represents the unoccupied electronic states of the molecular layer, and permits determination of the lowest unoccupied molecular orbital (LUMO) level of the molecular layer *[41, 119]*. The calculation of the LUMO energy can be used to estimate the barrier height for electrons tunneling (ϕ_{e-})*[41, 120]*.

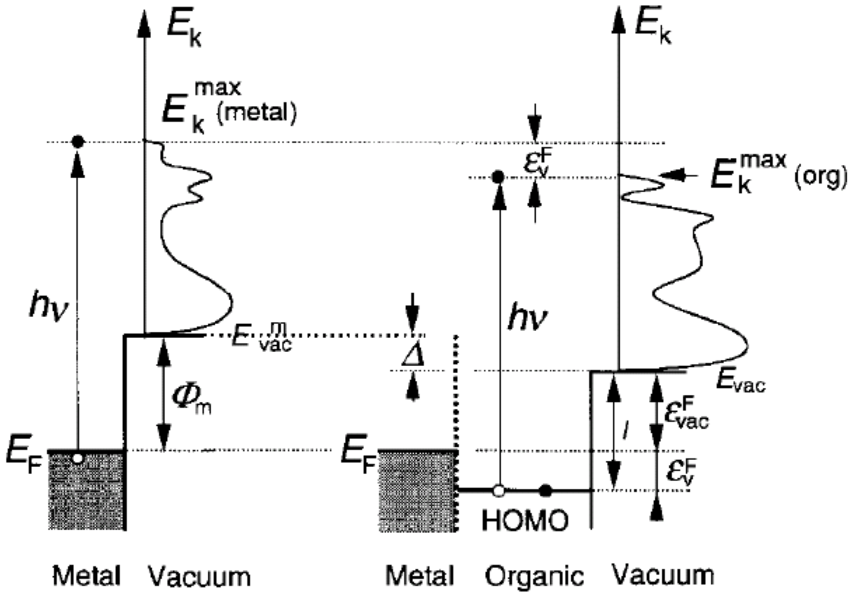

Figure 1.18. Photoemission and UPS spectra of metal (right Figure) and metal modified with organic molecular layer (left Figure). $h\nu$ is photon energy, E_F Fermi level, ϕ_m metal work function, E_{vac}^{m} metal vacuum level, E_K kinetic energy of the photon, ε_v^F energy of HOMO relative to metal Fermi level, ε_{vac}^F vacuum level of organic layer relative to metal Fermi level (Reprinted with permission form reference *[155]*. Copyright 1999 John Wiley and Sons).

1.7 Scope and Research Objective

The overall goal of the research described in this thesis is the investigation of organic molecular layer integrity during fabrication of molecular electronic junctions, and to assess the compatibility of molecular junctions with manufacturing and operating conditions common in the existing microelectronic industry. Optical and photoelectron spectroscopy are used extensively for characterization of molecular electronic devices during fabrication and in operation. In chapter 2, aromatic molecular layer integrity after direct deposition of metals was investigated by “back-side” optical spectroscopy through transparent substrates. To carry out “back-side” spectroscopy, optically transparent substrates were modified by organic molecular layers using ultrathin Titanium (Ti) ~ 5 nm as a primer. Metallic Ti evaporated using electron beam evaporator is very reactive and can provide electrons for electrochemical reduction of aromatic diazonium molecules. The aromatic molecular layer integrity was probed by “back-side” spectroscopic techniques such as Raman and IR spectroscopy.

In chapter 3, the compatibility of molecular electronic junctions based on carbon (PPF) bottom contact with several current microfabrication processes is described. Thermal stability of the molecular layer on modified surface and in the completely finished device was studied. In addition, compatibility with photolithographic processes and different solvents used during the process and direct top contact evaporation of various metals were investigated.

In chapter 4, heavily doped n- and p- type Si (111) substrates were used as the bottom electrode to replace the carbon. Semiconductor Si was used in order to understand the effect of electrode/molecule interface and compare carbon based molecular electronic junctions to similar devices made with a widely-used silicon semiconductor. Furthermore, Si as a substrate can provide information about transport mechanism of the charge carrier within the device, since Si allows the manipulation of the substrate Fermi level through changing either the doping level or type (p vs. n). Comparison of Si- based molecular junctions with similar devices made with carbon substrates permits a more complete picture of the factors that control charge transport in molecular junctions.

1.8 References

[1] H. K. Charles, *Johns Hopkins Apl Technical Digest* **2005**, *26*, 402.

[2] A. Aviram, M. A. Ratner, *Chemical Physics Letters* **1974**, *29*, 277.

[3] B. Fabre, *Accounts of Chemical Research* **2010**, *43*, 1509.

[4] I. Ron, I. Pecht, M. Sheves, D. Cahen, *Accounts of Chemical Research* **2010**, *43*, 945.

[5] J. D. Batteas, C. E. D. Chidsey, C. R. Kagan, T. Seideman, **2007**, ***http://www.wtec.org/MolecularElectronics/MolecularElectronics-enc.pdf***.

[6] H. B. Akkerman, B. De Boer, *Journal of Physics: Condensed Matter* **2008**, *20*, 013001.

[7] R. L. McCreery, *Chem. Mater.* **2004**, *16*, 4477.

[8] H. Haick, D. Cahen, *Accounts of Chemical Research* **2008**, *41*, 359.

[9] H. Haick, D. Cahen, *Progress in Surface Science* **2008**, *83*, 217.

[10] F. Chen, J. Hihath, Z. F. Huang, X. L. Li, N. J. Tao, *Annual Review of Physical Chemistry* **2007**, *58*, 535.

[11] E. A. Weiss, J. K. Kriebel, M. A. Rampi, G. M. Whitesides, *Philosophical Transactions of the Royal Society a-Mathematical Physical and Engineering Sciences* **2007**, *365*, 1509.

[12] R. L. McCreery, A. J. Bergren, *Advanced Materials* **2009**, *21*, 4303.

[13] A. Vilan, O. Yaffe, A. Biller, A. Salomon, A. Kahn, D. Cahen, *Advanced Materials* **2010**, *22*, 140.

[14] D. A. Rider, K. D. Harris, D. Wang, J. Bruce, M. D. Fleischauer, R. T. Tucker, M. J. Brett, J. M. Buriak, *ACS Appl. Mater. Interfaces* **2009**, *1*, 279.

[15] X. Y. Li, D. S. Wang, Q. Z. Luo, J. An, Y. H. Wang, G. X. Cheng, *Journal of Chemical Technology and Biotechnology* **2008**, *83*, 1558.

[16] G. Ashkenasy, D. Cahen, R. Cohen, A. Shanzer, A. Vilan, *Accounts of Chemical Research* **2002**, *35*, 121.

[17] K. Vaik, A. Sarapuu, K. Tammeveski, F. Mirkhalaf, D. J. Schiffrin, *Journal of Electroanalytical Chemistry* **2004**, *564*, 159.

[18] J. N. Chazalviel, P. Allongue, A. C. Gouget-Laemmel, C. H. de Villeneuve, A. Moraillon, F. Ozanam, *Science of Advanced Materials* **2011**, *3*, 332.

[19] L. Touahir, P. Allongue, D. Aureau, R. Boukherroub, J. N. Chazalviel, E. Galopin, A. C. Gouget-Laemmel, C. H. de Villeneuve, A. Moraillon, J. Niedziolka-Jonsson, F. Ozanam, J. S. Andresa, S. Sam, I. Solomon, S. Szunerits, *Bioelectrochemistry* **2010**, *80*, 17.

[20] J. J. Gooding, *Electroanalysis* **2008**, *20*, 573.

[21] X. M. Jiang, L. M. Wang, J. Wang, C. Y. Chen, *Applied Biochemistry and Biotechnology* **2012**, *166*, 1533.

[22] M. F. Juarez, F. A. Soria, E. M. Patrito, P. Paredes-Olivera, *Physical Chemistry Chemical Physics* **2011**, *13*, 21411.

[23] R. M. Metzger, T. Xu, I. R. Peterson, *Journal of Physical Chemistry B* **2001**, *105*, 7280.

[24] A. Ulman, *Chemical Reviews* **1996**, *96*, 1533.

[25] J. M. Lehn, *Angewandte Chemie-International Edition in English* **1990**, *29*, 1304.

[26] D. L. Allara, R. G. Nuzzo, *Langmuir* **1985**, *1*, 52.

[27] D. L. Allara, R. G. Nuzzo, *Langmuir* **1985**, *1*, 45.

[28] N. E. Schlotter, M. D. Porter, T. B. Bright, D. L. Allara, *Chemical Physics Letters* **1986**, *132*, 93.

[29] J. Gun, J. Sagiv, *Journal of Colloid and Interface Science* **1986**, *112*, 457.

[30] S. Brandriss, S. Margel, *Langmuir* **1993**, *9*, 1232.

[31] K. Mathauer, C. W. Frank, *Langmuir* **1993**, *9*, 3446.

[32] J. Gun, R. Iscovici, J. Sagiv, *Journal of Colloid and Interface Science* **1984**, *101*, 201.

[33] J. Lee, B. J. Jung, J. I. Lee, H. Y. Chu, L. M. Do, H. K. Shim, *Journal of Materials Chemistry* **2002**, *12*, 3494.

[34] R. W. Murray, *Accounts of Chemical Research* **1980**, *13*, 135.

[35] J. R. Lenhard, R. W. Murray, *Journal of Electroanalytical Chemistry* **1977**, *78*, 195.

[36] Z. W. Zhang, X. J. Feng, Q. M. Luo, B. F. Liu, *Electrophoresis* **2009**, *30*, 3174.

[37] R. G. Nuzzo, D. L. Allara, *Journal of the American Chemical Society* **1983**, *105*, 4481.

[38] J. C. Love, L. A. Estroff, J. K. Kriebel, R. G. Nuzzo, G. M. Whitesides, *Chemical Reviews* **2005**, *105*, 1103.

[39] H. B. Akkerman, R. C. G. Naber, B. Jongbloed, P. A. van Hal, P. W. M. Blom, D. M. de Leeuw, B. de Boer, *Proceedings of the National Academy of Sciences of the United States of America* **2007**, *104*, 11161.

[40] H. B. Akkerman, P. W. M. Blom, D. M. de Leeuw, B. de Boer, *Nature* **2006**, *441*, 69.

[41] Y. B. Qi, O. Yaffe, E. Tirosh, A. Vilan, D. Cahen, A. Kahn, *Chemical Physics Letters* **2011**, *511*, 344.

[42] H. B. Akkerman, A. J. Kronemeijer, J. Harkema, P. A. van Hal, E. C. P. Smits, D. M. de Leeuw, P. W. M. Blom, *Organic Electronics* **2010**, *11*, 146.

[43] R. S. Deinhammer, M. Ho, J. W. Anderegg, M. D. Porter, *Langmuir* **1994**, *10*, 1306.

[44] G. Herlem, K. Reybier, A. Trokourey, B. Fahys, *Journal of the Electrochemical Society* **2000**, *147*, 597.

[45] G. Herlem, C. Goux, B. Fahys, F. Dominati, A. M. Goncalves, C. Mathieu, E. Sutter, A. Trokourey, J. F. Penneau, *Journal of Electroanalytical Chemistry* **1997**, *435*, 259.

[46] H. Yan, R. L. McCreery, *ACS Applied Materials & Interfaces* **2009**, *1*, 443.

[47] P. A. Brooksby, A. J. Downard, S. S. C. Yu, *Langmuir* **2005**, *21*, 11304.

[48] P. D. Astudillo, A. Galano, F. J. Gonzalez, *Journal of Electroanalytical Chemistry* **2007**, *610*, 137.

[49] H. Maeda, Y. Yamauchi, M. Hosoe, T. X. Li, E. Yamaguchi, M. Kasamatsu, H. Ohmori, *Chemical & Pharmaceutical Bulletin* **1994**, *42*, 1870.

[50] H. Maeda, T. X. Li, M. Hosoe, M. Itami, Y. Yamauchi, H. Ohmori, *Analytical Sciences* **1994**, *10*, 963.

[51] M. Gros-Jean, R. Herino, J. N. Chazalviel, F. Ozanam, D. Lincot, *Materials Science and Engineering B-Solid State Materials for Advanced Technology* **2000**, *69*, 77.

[52] A. Fidelis, F. Ozanam, J. N. Chazalviel, *Surface Science* **2000**, *444*, L7.

[53] G. Lecayon, Y. Bouizem, C. Legressus, C. Reynaud, C. Boiziau, C. Juret, *Chemical Physics Letters* **1982**, *91*, 506.

[54] G. Deniau, G. Lecayon, P. Viel, G. Hennico, J. Delhalle, *Langmuir* **1992**, *8*, 267.

[55] C. H. deVilleneuve, J. Pinson, M. C. Bernard, P. Allongue, *Journal of Physical Chemistry B* **1997**, *101*, 2415.

[56] P. Allongue, M. Delamar, B. Desbat, O. Fagebaume, R. Hitmi, J. Pinson, J. M. Saveant, *Journal of the American Chemical Society* **1997**, *119*, 201.

[57] M. Delamar, R. Hitmi, J. Pinson, J. M. Saveant, *Journal of the American Chemical Society* **1992**, *114*, 5883.

[58] C. Bourdillon, M. Delamar, C. Demaille, R. Hitmi, J. Moiroux, J. Pinson, *Journal of Electroanalytical Chemistry* **1992**, *336*, 113.

[59] E. Coulon, J. Pinson, J. D. Bourzat, A. Commercon, J. P. Pulicani, *Langmuir* **2001**, *17*, 7102.

[60] T.-C. Kuo, R. L. McCreery, G. M. Swain, *Electrochemical and Solid-State Letters* **1999**, *2*, 288.

[61] S. Ranganathan, I. Steidel, F. Anariba, R. L. McCreery, *Nano Lett.* **2001**, *1*, 491.

[62] C. H. deVilleneuve, J. Pinson, F. Ozanam, J. N. Chazalviel, P. Allongue, *Electrochemical Synthesis and Modification of Materials* **1997**, *451*, 185.

[63] P. Allongue, C. H. de Villeneuve, J. Pinson, F. Ozanam, J. N. Chazalviel, X. Wallart, *Electrochimica Acta* **1998**, *43*, 2791.

[64] A. Scott, D. B. Janes, *Journal of Applied Physics* **2009**, *105.*

[65] W. Wang, A. Scott, N. Gergel-Hackett, C. A. Hacker, D. B. Janes, C. A. Richter, *Nano Letters* **2008**, *8*, 478.

[66] A. Scott, C. A. Hacker, D. B. Janes, *Journal of Physical Chemistry C* **2008**, *112*, 14021.

[67] M. P. Stewart, F. Maya, D. V. Kosynkin, S. M. Dirk, J. J. Stapleton, C. L. McGuiness, D. L. Allara, J. M. Tour, *Journal of the American Chemical Society* **2004**, *126*, 370.

[68] B. L. Hurley, R. L. McCreery, *Journal of the Electrochemical Society* **2004**, *151*, B252.

[69] L. Laurentius, S. R. Stoyanov, S. Gusarov, A. Kovalenko, R. B. Du, G. P. Lopinski, M. T. McDermott, *Acs Nano* **2011**, *5*, 4219.

[70] M. Busson, A. Berisha, C. Combellas, F. Kanoufi, J. Pinson, *Chemical Communications* **2011**, *47*, 12631.

[71] A. Adenier, N. Barre, E. Cabet-Deliry, A. Chausse, S. Griveau, F. Mercier, J. Pinson, C. Vautrin-Ul, *Surface Science* **2006**, *600*, 4801.

[72] Q. M. Pan, M. Wang, W. T. Chen, *Chemistry Letters* **2007**, *36*, 1312.

[73] S. Maldonado, T. J. Smith, R. D. Williams, S. Morin, E. Barton, K. J. Stevenson, *Langmuir* **2006**, *22*, 2884.

[74] A. Merson, T. Dittrich, Y. Zidon, J. Rappich, Y. Shapira, *Applied Physics Letters* **2004**, *85*, 1075.

[75] C. Combellas, M. Delamar, F. Kanoufi, J. Pinson, F. I. Podvorica, *Chemistry of Materials* **2005**, *17*, 3968.

[76] A. Adenier, E. Cabet-Deliry, A. Chausse, S. Griveau, F. Mercier, J. Pinson, C. Vautrin-Ul, *Chemistry of Materials* **2005**, *17*, 491.

[77] J. Pinson, F. Podvorica, *Chemical Society Reviews* **2005**, *34*, 429.

[78] P. A. Brooksby, A. J. Downard, *Journal of Physical Chemistry B* **2005**, *109*, 8791.

[79] F. Anariba, S. H. DuVall, R. L. McCreery, *Analytical Chemistry* **2003**, *75*, 3837.

[80] J. K. Kariuki, M. T. McDermott, *Langmuir* **2001**, *17*, 5947.

[81] D. D. M. Wayner, R. A. Wolkow, *Journal of the Chemical Society-Perkin Transactions 2* **2002**, 23.

[82] J. M. Buriak, *Chemical Reviews* **2002**, *102*, 1271.

[83] M. R. Linford, P. Fenter, P. M. Eisenberger, C. E. D. Chidsey, *Journal of the American Chemical Society* **1995**, *117*, 3145.

[84] M. R. Linford, C. E. D. Chidsey, *Journal of the American Chemical Society* **1993**, *115*, 12631.

[85] J. E. Bateman, R. D. Eagling, D. R. Worrall, B. R. Horrocks, A. Houlton, *Angewandte Chemie-International Edition* **1998**, *37*, 2683.

[86] R. Boukherroub, S. Morin, P. Sharpe, D. D. M. Wayner, P. Allongue, *Langmuir* **2000**, *16*, 7429.

[87] F. Effenberger, G. Gotz, B. Bidlingmaier, M. Wezstein, *Angewandte Chemie-International Edition* **1998**, *37*, 2462.

[88] D. J. Wold, C. D. Frisbie, *Journal of the American Chemical Society* **2000**, *122*, 2970.

[89] M. T. Cygan, T. D. Dunbar, J. J. Arnold, L. A. Bumm, N. F. Shedlock, T. P. Burgin, L. Jones, D. L. Allara, J. M. Tour, P. S. Weiss, *Journal of the American Chemical Society* **1998**, *120*, 2721.

[90] Z. F. Huang, F. Chen, P. A. Bennett, N. J. Tao, *Journal of the American Chemical Society* **2007**, *129*, 13225.

[91] B. Q. Xu, N. J. J. Tao, *Science* **2003**, *301*, 1221.

[92] B. Kim, S. H. Choi, X. Y. Zhu, C. D. Frisbie, *Journal of the American Chemical Society* **2011**, *133*, 19864.

[93] V. B. Engelkes, J. M. Beebe, C. D. Frisbie, *Journal of the American Chemical Society* **2004**, *126*, 14287.

[94] L. Luo, C. D. Frisbie, *Journal of the American Chemical Society* **2010**, *132*, 8854.

[95] L. M. Ballesteros, S. Martin, C. Momblona, S. Marques-Gonzalez, M. C. Lopez, R. J. Nichols, P. J. Low, P. Cea, *Journal of Physical Chemistry C* **2012**, *116*, 9142.

[96] B. Kim, J. M. Beebe, Y. Jun, X. Y. Zhu, C. D. Frisbie, *Journal of the American Chemical Society* **2006**, *128*, 4970.

[97] J. Moreland, J. W. Ekin, *Journal of Applied Physics* **1985**, *58,* 3888.

[98] M. A. Reed, C. Zhou, C. J. Muller, T. P. Burgin, J. M. Tour, *Science* **1997**, *278*, 252.

[99] H. Park, A. K. L. Lim, A. P. Alivisatos, J. Park, P. L. McEuen, *Applied Physics Letters* **1999**, *75*, 301.

[100] Y. Noguchi, T. Nagase, T. Kubota, T. Kamikado, S. Mashiko, *Thin Solid Films* **2006**, *499*, 90.

[101] M. T. Gonzalez, S. M. Wu, R. Huber, S. J. van der Molen, C. Schonenberger, M. Calame, *Nano Letters* **2006**, *6*, 2238.

[102] J. G. Kushmerick, D. B. Holt, S. K. Pollack, M. A. Ratner, J. C. Yang, T. L. Schull, J. Naciri, M. H. Moore, R. Shashidhar, *Journal of the American Chemical Society* **2002**, *124*, 10654.

[103] A. P. Bonifas, R. L. McCreery, *Nano Letters* **2011**, *11,* 4725.

[104] H. Haick, O. Niitsoo, J. Ghabboun, D. Cahen, *Journal of Physical Chemistry C* **2007**, *111*, 2318.

[105] Z. H. Zhu, T. A. Daniel, M. Maitani, O. M. Cabarcos, D. L. Allara, N. Winograd, *Journal of the American Chemical Society* **2006**, *128,* 13710.

[106] A. V. Walker, T. B. Tighe, O. M. Cabarcos, M. D. Reinard, B. C. Haynie, S. Uppili, N. Winograd, D. L. Allara, *Journal of the American Chemical Society* **2004**, *126*, 3954.

[107] G. L. Fisher, A. V. Walker, A. E. Hooper, T. B. Tighe, K. B. Bahnck, H. T. Skriba, M. D. Reinard, B. C. Haynie, R. L. Opila, N. Winograd, D. L. Allara, *Journal of the American Chemical Society* **2002**, *124*, 5528.

[108] G. L. Fisher, A. E. Hooper, R. L. Opila, D. L. Allara, N. Winograd, *Journal of Physical Chemistry B* **2000**, *104*, 3267.

[109] G. L. Fisher, A. Hooper, R. L. Opila, D. R. Jung, D. L. Allara, N. Winograd, *Journal of Electron Spectroscopy and Related Phenomena* **1999**, *98*, 139.

[110] B. C. Haynie, A. V. Walker, T. B. Tighe, D. L. Allara, N. Winograd, *Applied Surface Science* **2003**, *203*, 433.

[111] B. de Boer, M. M. Frank, Y. J. Chabal, W. R. Jiang, E. Garfunkel, Z. Bao, *Langmuir* **2004**, *20*, 1539.

[112] A. V. Walker, T. B. Tighe, J. Stapleton, B. C. Haynie, S. Upilli, D. L. Allara, N. Winograd, *Applied Physics Letters* **2004**, *84*, 4008.

[113] D. K. Aswal, C. Petit, G. Salace, A. Guerin, S. Lenfant, J. V. Yakhmi, D. Vuillaume, *Physica Status Solidi a-Applications and Materials Science* **2006**, *203*, 1464.

[114] C. A. Hacker, C. A. Richter, N. Gergel-Hackett, L. J. Richter, *Journal of Physical Chemistry C* **2007**, *111*, 9384.

[115] C. A. Richter, C. A. Hacker, L. J. Richter, *Journal of Physical Chemistry B* **2005**, *109*, 21836.

[116] H. Asanuma, H. Noguchi, Y. F. Huang, K. Uosaki, H. Z. Yu, *Journal of Physical Chemistry C* **2009**, *113*, 21139.

[117] A. M. Nowak, R. L. McCreery, *Analytical Chemistry* **2004**, *76*, 1089.

[118] A. M. Nowak, R. L. McCreery, *Journal of the American Chemical Society* **2004**, *126*, 16621.

[119] O. Yaffe, Y. B. Qi, L. Scheres, S. R. Puniredd, L. Segev, T. Ely, H. Haick, H. Zuilhof, A. Vilan, L. Kronik, A. Kahn, D. Cahen, *Physical Review B* **2012**, *85*.

[120] A. Salomon, T. Boecking, O. Seitz, T. Markus, F. Amy, C. Chan, W. Zhao, D. Cahen, A. Kahn, *Advanced Materials* **2007**, *19*, 445.

[121] A. O. Solak, S. Ranganathan, T. Itoh, R. L. McCreery, *Electrochemical and Solid-State Letters* **2002**, *5*, E43.

[122] L. Cademartiri, M. M. Thuo, C. A. Nijhuis, W. F. Reus, S. Tricard, J. R. Barber, R. N. S. Sodhi, P. Brodersen, C. Kim, R. C. Chiechi, G. M. Whitesides, *Journal of Physical Chemistry C* **2012**, *116*, 10848.

[123] D. Fracasso, H. Valkenier, J. C. Hummelen, G. C. Solomon, R. C. Chiechi, *Journal of the American Chemical Society* **2011**, *133*, 9556.

[124] R. C. Chiechi, E. A. Weiss, M. D. Dickey, G. M. Whitesides, *Angewandte Chemie-International Edition* **2008**, *47*, 142.

[125] H. J. Yoon, N. D. Shapiro, K. M. Park, M. M. Thuo, S. Soh, G. M. Whitesides, *Angewandte Chemie-International Edition* **2012**, *51*, 4658.

[126] H. Shpaisman, R. Har-Lavan, N. Stein, O. Yaffe, R. Korobko, O. Seitz, A. Vilan, D. Cahen, *Advanced Functional Materials* **2010**, *20*, 2181.

[127] H. Haick, J. Ghabboun, O. Niitsoo, H. Cohen, D. Cahen, A. Vilan, J. Y. Hwang, A. Wan, F. Amy, A. Kahn, *Journal of Physical Chemistry B* **2005**, *109*, 9622.

[128] H. Haick, M. Ambrico, J. Ghabboun, T. Ligonzo, D. Cahen, *Physical Chemistry Chemical Physics* **2004**, *6*, 4538.

[129] Y. L. Loo, D. V. Lang, J. A. Rogers, J. W. P. Hsu, *Nano Letters* **2003**, *3*, 913.

[130] A. Vilan, D. Cahen, *Advanced Functional Materials* **2002**, *12*, 795.

[131] K. T. Shimizu, J. D. Fabbri, J. J. Jelincic, N. A. Melosh, *Advanced Materials* **2006**, *18*, 1499.

[132] A. P. Bonifas, R. L. McCreery, *Nature Nanotechnology* **2010**, *5*, 612.

[133] M. Manolova, V. Ivanova, D. M. Kolb, H. G. Boyen, P. Ziemann, M. Buttner, A. Romanyuk, P. Oelhafen, *Surface Science* **2005**, *590*, 146.

[134] V. Ivanova, T. Baunach, D. A. Kolb, *Electrochimica Acta* **2005**, *50*, 4283.

[135] W. Deng, L. Yang, D. Fujita, H. Nejoh, C. Bai, *Applied Physics a-Materials Science & Processing* **2000**, *71*, 639.

[136] D. Y. Qu, K. Uosaki, *Chemistry Letters* **2006**, *35*, 258.

[137] D. Y. Qu, K. Uosaki, *Journal of Electroanalytical Chemistry* **2011**, *662*, 80.

[138] M. Epple, A. M. Bittner, A. Kuhnke, K. Kern, W. Q. Zheng, A. Tadjeddine, *Langmuir* **2002**, *18*, 773.

[139] J. H. Tian, Y. Yang, X. S. Zhou, B. Schollhorn, E. Maisonhaute, Z. B. Chen, F. Z. Yang, Y. Chen, C. Amatore, B. W. Mao, Z. Q. Tian, *Chemphyschem* **2010**, *11*, 2745.

[140] R. P. Kalakodimi, A. M. Nowak, R. L. McCreery, *Chemistry of Materials* **2005**, *17*, 4939.

[141] S. Ranganathan, R. L. McCreery, *Analytical Chemistry* **2001**, *73*, 893.

[142] S. Ranganathan, R. McCreery, S. M. Majji, M. Madou, *Journal of the Electrochemical Society* **2000**, *147*, 277.

[143] R. B. Du, S. Ssenyange, M. Aktary, M. T. McDermott, *Small* **2009**, *5*, 1162.

[144] S. Donner, H. W. Li, E. S. Yeung, M. D. Porter, *Analytical Chemistry* **2006**, *78*, 2816.

[145] Y. Dai, G. M. Swain, M. D. Porter, J. Zak, *Analytical Chemistry* **2008**, *80*, 14.

[146] H. Tian, A. J. Bergren, R. L. McCreery, *Applied Spectroscopy* **2007**, *61*, 1246.

[147] A. J. Bergren, R. L. McCreery, *Annual Review of Analytical Chemistry, Vol 4* **2011**, *4*, 173.

[148] A. P. Bonifas, R. L. McCreery, *Chemistry of Materials* **2008**, *20*, 3849.

[149] L. H. Yu, C. D. Zangmeister, J. G. Kushmerick, *Physical Review Letters* **2007**, *98*, 206803.

[150] D. R. Ward, N. J. Halas, J. W. Ciszek, J. M. Tour, Y. Wu, P. Nordiander, D. Natelson, *Nano Letters* **2008**, *8*, 919.

[151] J. H. Tian, B. Liu, S. Jin, K. Dai, Z. B. Chen, X. L. Li, H. X. Ke, S. T. Wu, Y. Yang, B. Ren, B. W. Mao, N. J. Tao, Z. Q. Tian, *2007 7th Ieee Conference on Nanotechnology, Vol 1-3* **2007**, 1313.

[152] A. Jaiswal, K. G. Tavakoli, S. Z. Zou, *Analytical Chemistry* **2006**, *78*, 120.

[153] D. Cahen, A. Kahn, *Advanced Materials* **2003**, *15*, 271.

[154] Y. L. Gao, *Materials Science & Engineering R-Reports* **2010**, *68*, 39.

[155] H. Ishii, K. Sugiyama, E. Ito, K. Seki, *Advanced Materials* **1999**, *11*, 605.

[156] F. J. Himpsel, *Journal of Physics and Chemistry of Solids* **1988**, *49*, 3.

[157] G. Borstel, G. Thorner, *Surface Science Reports* **1988**, *8*, 1.

[158] P. T. Andrews, *Vacuum* **1988**, *38*, 257.

[159] R. Drube, V. Dose, A. Goldmann, *Surface Science* **1988**, *197*, 317.

[160] I. R. Collins, P. T. Andrews, *Vacuum* **1988**, *38*, 430.

Chapter 2

Modification of Optically Transparent Substrates with Diazonium Reagents for Spectroscopy of Buried Interfaces

2.1 Introduction

The derivatization of a wide variety of surfaces with organic compounds that possess desirable chemical or physical properties is an important technological objective. Furthermore, the characterization of molecular layers on the surface of these substrates is an important consideration for many applications. This is especially important in cases where the molecular layers are incorporated into a more complex structure with a targeted function. For example, in molecular electronics, stratified layers of conductors and molecules are utilized to build devices useful for studying charge transport mechanisms or novel electronic phenomena as a function of molecular structure*[1-6]*. In such investigations, it is critical to establish the influence of molecular structure on the performance of the device. However, it can be difficult to probe molecular species buried in working electronic devices since the contacts and/or substrates must be at least partially transparent in the frequency range under study*[3, 7-9]*. A general pathway to covalently bind a molecular layer to a wide range of surfaces that can be characterized using various optical spectroscopic techniques would therefore be beneficial.

The manipulation of interfaces is important in numerous areas of science and engineering. For example, advances in the design and performance of sensors*[10, 11]*, energy conversion devices*[12]*, catalysts*[13]*, and molecular electronics*[3, 14-16]* all rely, in part, on well-controlled surface modification. To this end, aromatic diazonium salts have been used to modify substrate surfaces having a wide range of conductivity*[17, 18]*, including metals*[18-26]*, carbon*[14, 18, 27-31]*, carbon nanotubes*[32]*, and semiconductors*[33, 34]*. Diazonium-mediated surface modification relies on the generation of a phenyl radical species through reduction of the diazonium group followed by elimination of N_2. The radical species interacts with a surface site, often resulting in a covalent bond, the details of which depend on the surface material*[18]*. In particular, when the surface in question has free electrons and if electron transfer is favourable thermodynamically, a spontaneous reduction of the diazonium ion can take place, resulting in a spontaneous surface modification reaction*[35, 36]*. The resulting molecular layers are generally robust and the modified surfaces can be applied in many different studies. However, it should be noted that the aggressive nature of the radical-mediated bonding pathway readily leads to multi-layer films. The thickness of these films can be controlled by adjusting the appropriate conditions (e.g., diazonium ion concentration and immersion time) and verifying thickness with atomic force mircoscpopy*[28]*.

In order to characterize buried molecular layers in electronic devices, several methods have been reported. Raman spectra have been obtained through thin semi-transparent top contacts*[9, 15, 37, 38]*. Infrared reflection spectroscopy has been carried out through partially IR transparent Si substrates that also act as the support for the molecular layer*[39, 40]*. In this case, thick, reflective top contacts are applied on top of the molecules in order to provide a highly reflective surface*[39, 40]*. Ultraviolet-visible spectroscopy has been reported for characterization of molecular layers through multiple thin layers of a completed molecular electronic device*[7]*. Other reported optical probes include attenuated total internal reflection (ATR) FTIR spectroscopy*[41, 42]*, multiple transmission-reflection infrared (MTR)*[43]*, and infrared reflectance spectroscopy*[44, 45]*. Finally, inelastic electron tunneling spectroscopy (IETS) also provides information about molecular structure and geometry during the course of charge transfer measurements*[46-48]*.

In this chapter, we describe the use of reactive metal primers to modify quartz, Si, glass, and other surfaces so that Raman, IRRAS, *p*-polarized backside IRRAS, and ultraviolet-visible (UV-Vis) spectroscopic measurements can be accommodated in molecular junctions and related structures. Both Ti and Al are known to form strong metal-oxygen and metal-carbon bonds with a variety of materials, and are often used as “adhesion layers.” The thin metal layer also provides a suitable reducing potential at the substrate surface that drives the reduction of diazonium ions, generating radicals that can bind to the surface, leading to the formation of a molecular organic layer. After deposition of top contacts, an analysis of Raman and IR vibrational spectra can be used to test molecular integrity during these often harsh fabrication procedures. The nature of the bond formed between the metal primer and organic layer was investigated using X-ray photoelectron spectroscopy, and the stability of the molecular layer on the surface was studied by subjecting primer-derived molecular layers to heating and immersion in organic solvents and aqueous acid and base. Finally, the variables affecting the characteristics of the molecular layer including immersion time, primer metal thickness, and diazonium salt concentration were also investigated.

2.2 Experimental Section

Acetonitrile, acetone and isopropanol (HPLC grade, Fischer Scientific) were used as received. Water was purified by a Millipore system (18 MΩ, 3 ppb TOC). 4-Nitroazobenzene (NAB) 4'-diazonium tetrafluoroborate salt was prepared as described in detail elsewhere*[37]*. For Raman and UV-Vis spectroscopy, 25 x 25 x 0.22 mm^3 quartz microscope cover slips (Technical Glass Products, Inc.) were used as optically transparent supports. For infrared experiments, infrared transparent Si was used (double-side-polished highly n-doped Si (111) from Cemat Silicon S. A.) after dicing into 18 x 15 mm^2 chips. In addition, glass (22 x 22 x 0.14 mm^3 glass cover slides from Fischer scientific) and high density polyethylene (HDPE) from Nalgene® plastic bottles cut into 20 x 20 mm^2 pieces were used in other experiments. Quartz (Q), glass (G), and Si substrates were cleaned by sonication in acetone, isopropanol and then ultrapure water for 10 min each, and HDPE substrates were cleaned by sonication in ultrapure water only; all substrates were dried after cleaning in a stream of N_2. Substrates were transferred to an electron-beam evaporator (Kurt J. Lesker PVD75), and the chamber evacuated overnight to a pressure of 2.2×10^{-7} Torr before beginning deposition. Metals (Ti, Al, and Cr) were deposited at 0.3 Å/s, as determined from a quartz crystal microbalance near the sample. Metal thicknesses are indicated in nm in sample designations; e.g., Q/Ti(5) indicates 5 nm of Ti deposited on quartz.

Chemical derivatization of the primed surfaces was performed by the spontaneous reduction of diazonium salts in acetonitrile solution. Immediately after removing primed substrates from the evaporation chamber, they were immersed in a freshly prepared solution of the diazonium salt (1 mM) in acetonitrile for 30 min, except for the modification of HDPE, which was done using aqueous 0.1 M H_2SO_4 as the solvent. Following immersion, the substrate was rinsed with neat acetonitrile (or 0.1 M H_2SO_4) and then dried in a stream of N_2. Reflective metal overlayers of Au or Ag were electron-beam deposited at 3 Å s^{-1} and a pressure of 2.6 x 10^{-6} Torr onto Q/primer/NAB or Si/primer/NAB substrates for “backside” Raman and IR, respectively. For XPS experiments, thermally oxidized Si samples primed with Ti were removed from the evaporation chamber and placed into a low vacuum transport chamber before being transferred to the XPS analysis chamber in order to minimize atmospheric exposure. The peak deconvolution and peak fitting was performed with Casa XPS Software version 2.3.5 (Casa Software Ltd., U.K.) and applying both Gaussian and Lorentazian functions to fit the peaks, the G/L ratio equal to 7/3, and the background was modeled as Shirley function.

Raman spectra were collected through the transparent Q/primer substrate using a custom built spectrometer equipped with an Argon ion laser (514.5 nm), a 50 mm f/1.8 Nikon camera collection lens, a 2000 groove/mm holographic reflection grating, and a back scattering geometry that employs an Andor back-thinned charge-coupled device (CCD) detector cooled to -80 °C*[49]*. The incident power was ~19 mW on a 50 μm x 5 mm focal line, and the signal was integrated for 30 s, unless stated otherwise. Infrared spectra were collected using a Bruker optics VERTEX 70 FT-IR spectrometer fitted with a Harrick Seagull reflection accessory and an MCT detector. Each spectrum represents the average of 512 scans and was collected using an incidence angle of 80°, *p*-polarized light, a 1 mm optical aperture, 4 cm^{-1} resolution, Blackman-Harris 3-term apodization, and a zero-filling factor of 2. Data collection was initiated after a 20 min purge with dry N_2. UV-Vis spectra were recorded using a Perkin-Elmer Lambda 900 spectrometer.

2.3 Results and Discussion

Titanium is a highly reactive metal that is easily oxidized in ambient conditions*[50]*. This reactivity can be utilized to initiate the reduction of a diazonium salt in solution, which, in turn, forms free aryl radicals that bind to the Ti surface, resulting in a chemisorbed molecular layer. Figure 2-1 shows Raman spectra of quartz (Q) and Q/Ti (5 nm), before and after immersion in a solution of 1 mM NAB diazonium ion in acetonitrile for 30 minutes. Analysis of Figure 2-1 shows the ultrathin Ti layer does not contribute significantly to Raman scattering since both Q and Q/Ti(5) have very similar spectra. The only features in these spectra are those expected for bare quartz, and include a longitudinal optical (LO) mode at ~807 cm^{-1} and a transverse optical (TO) mode at ~795 cm^{-1} which appear as a broad unresolved peak, and a TO mode at 1073 cm^{-1} *[51]*. Moreover, the absence of the molecular vibrational spectrum for NAB after immersion of Q in NAB DS shows that without the reactive metal primer, NAB is not detectable on this surface using Raman spectroscopy. On the other hand, Figure 2.1 shows that the NAB spectrum is quite strong when the Q substrate is primed with a 5 nm layer of Ti (the characteristic Raman frequencies and peaks assignment for NAB on Q/Ti surface are given in Table 2-1). Furthermore, attempts to modify Q without a Ti primer layer but with a solution of a diazonium ion and reducing agent such as $NaBH_4$ or hypophosphorous acid, as reported for Au and carbon nanotubes*[19, 52]* respectively, did not result in an observable NAB Raman spectrum on the treated quartz sample. However, in order to use the reactivity of Ti metal as a surface primer, it is critical that primer exposure to air is minimized. Figure 2-2 shows an attempt to modify a Q substrate primed with Ti metal after exposure to ambient atmospheric conditions for three days prior to immersion in NAB DS, the intensity of the Raman signal for NAB was reduced by ~92% relative to that observed in Figure 2-1. Additional characterization of the chemisorbed NAB layer is described below, but first the generality of the approach to a variety of surfaces is discussed.

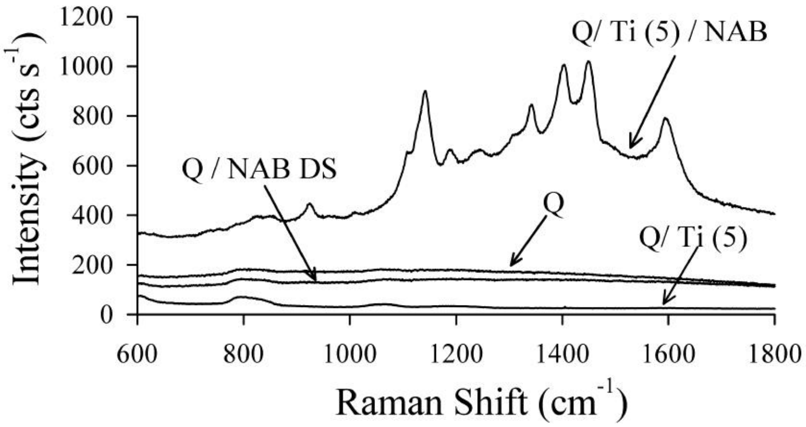

Figure 2-1. "Frontside" Raman spectra of four samples: un-primed quartz (Q) and Ti-primed quartz (Q/Ti(5)) are shown, also both types of samples after a 30 min immersion in a 1 mM solution of NAB diazonium salt (Q/NAB DS and Q/Ti(5)/NAB.

Table 2-1. Characteristic Raman frequencies and corresponding assignments for NAB molecular layer on Ti and Al.

NAB in CCl_4	**Ti / NAB**	**Al / NAB**	**Assignment**
933	927	922	CH bend
1112	--	--	Ph-NO_2 stretch
1147	1139	1141	Ph-N=N stretch
1183	1191	1191	CH bend
1347	1344	1341	NO_2 sym stretch
1412	1406	1401	N=N stretch
1449	1451	1448	N=N stretch
1594	1598	1596	C=C ring stretch

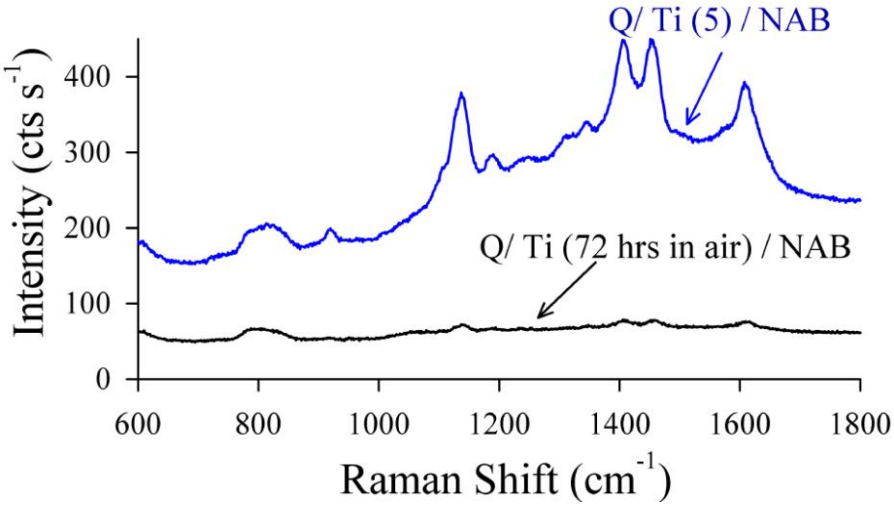

Figure 2-2. Raman spectra of Q/Ti (5)/NAB, just out of e-beam (blue curve) and Q/ Ti (5)/NAB after setting in air for 3 days prior to surface modification by NAB DS (black curve).

The Ti primer provides a platform for the spontaneous modification of various surfaces including quartz and Si (see below). Since Ti is known to adhere to numerous materials possessing a wide range of conductivity*[50, 53, 54]*, several different substrates were tested: Au, Al foil, SiO_x, glass, and high density polyethylene (HDPE). Raman spectroscopy confirmed bonding of NAB to Ti primer layers on glass and Al foil as shown in Figure 2-3, and modification of Au is shown in Figure 2-4. Since Raman spectroscopy was not suitable for monitoring bonding to HDPE due to a large substrate Raman signal, XPS was used to analyze HPDE after modification. Figure 2-5 shows XPS of HDPE following deposition of a 5 nm Ti primer layer and exposure to NAB DS solution in 0.1 M H_2SO_4, which exhibits characteristic N(1*s*) peaks in both low- and high-resolution XPS spectra.

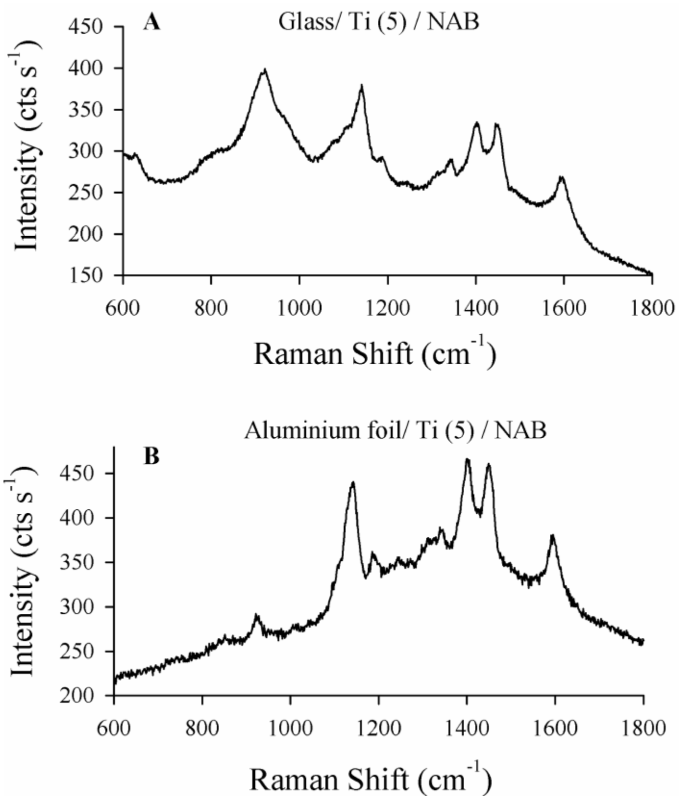

Figure 2-3. A) Raman Spectrum of Glass/ Ti (5) /NAB, B) Raman Spectrum of Al foil/ Ti (5) /NAB.

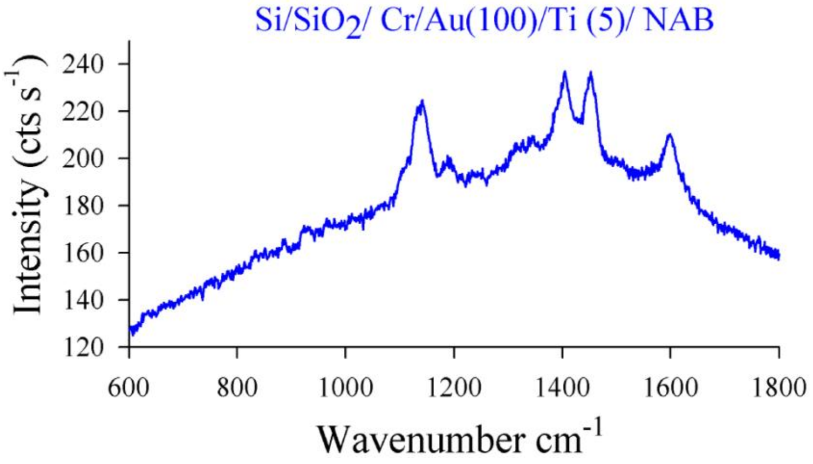

Figure 2-4. Raman Spectrum of Si/SiO_2/Cr(5)/Au(100)/Ti(5)/NAB.

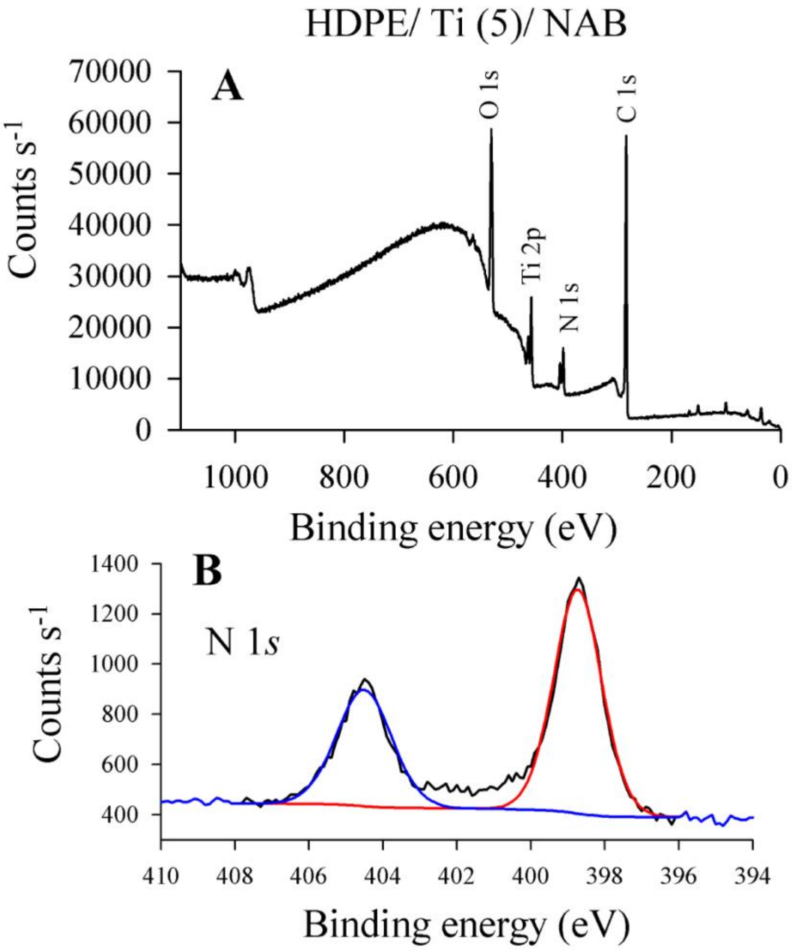

Figure 2-5. (A) XPS spectrum for High Density Polyethylene (HDPE)/ Ti(5) / NAB. (B) High-resolution spectrum in the nitrogen region showing an azo N(1*s*) peak (red curve) and a nitro N(1*s*) peak (blue curve) characteristic for NAB molecular layer.

Aluminium and Chromium are also widely used as adhesion layers as alternatives to Ti, and bulk Al alloy surfaces have been modified electrochemically with molecular layers through diazonium chemistry*[26]*. Using a 5 nm layer of metallic Al as a primer to modify a quartz surface spontaneously with NAB resulted in a Raman spectrum comparable to that observed when using Ti as the primer metal, as shown in Figure 2-6. However, the intensity when using

Al was ~85% that observed when using Ti as a primer. On the other hand, the NAB spectrum on a similarly freshly prepared Cr film on quartz was below the Raman detection limit as shown in Figure 2-7.

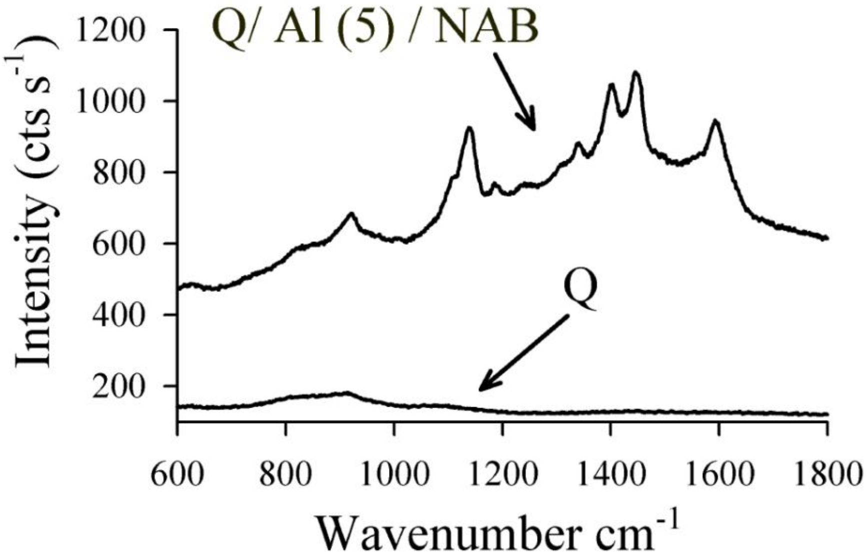

Figure 2-6. Raman Spectra for Q/ Al (5)/ NAB and bare quartz cover.

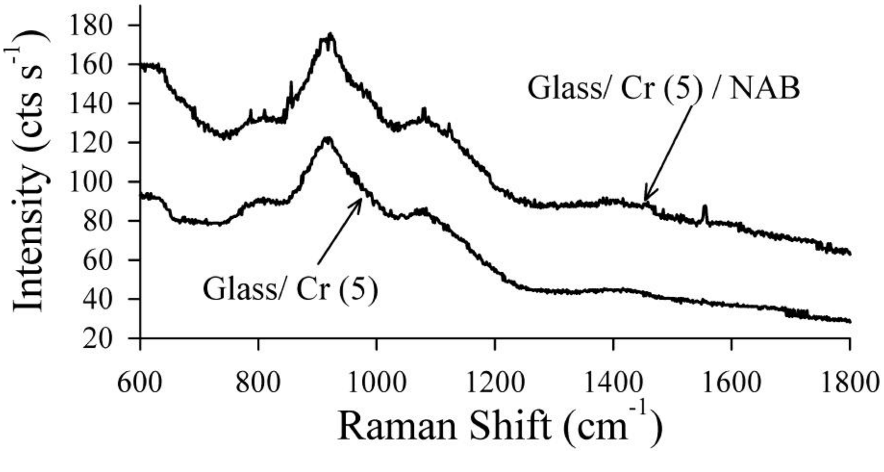

Figure 2-7. Raman Spectra of Glass/ Cr (5) and Glass/ Cr (5)/ NAB.

Quartz has a very low infrared transparency; however, silicon can be highly IR-transparent, depending on the details of doping*[55]*. Recently, a "backside" infrared reflection technique was developed in order to characterize aromatic molecular layers adsorbed directly on Si*[40]*. The method relies on the deposition of a metallic overlayer on top of the molecules in order to provide a reflective surface, and the spectrum is then acquired through the IR-transparent substrate. Instead of using this method for substrates in which the derivatization is carried out directly on Si, we have used metal-primed IR-transparent Si substrates. A significant portion of the infrared light incident from air onto the backside of the Si substrate passes through the Si, Ti, and molecule phases, and is reflected from the surface of the thick metal overlayer, enabling *p*-polarized backside infrared reflection absorption spectra (*p*-b IRRAS) to be obtained.

Figure 2-8 shows IRRAS spectra for several samples in two different geometries (as illustrated in Scheme 2-1) and illustrates the utility of an ultrathin metal primer in mediating the modification of Si with an organic layer. Figure 2-8A shows an IRRAS spectrum of NAB in the "backside" geometry, while Figure 2-8B shows conventional IRRAS spectra of Si/SiO_x/Cr(5)/Au(100 nm)/Ti(5) and Si/SiO_x/Cr(5)/Au(100 nm)/Ti(5)/NAB obtained in a conventional geometry (i.e., "frontside" spectra). These data illustrate two important points. First, the molecular layer survives the "direct" e-beam deposition of 100 nm of Au on the Si/Ti/NAB surface as shown in Figure 2-8A. Second, ultrathin Ti metal can be used to prime Si surfaces in order to derivatize the substrate with an organic layer, and the Ti does not significantly interfere with the IR spectral signature of the molecule. The characteristic vibrational spectrum for NAB appeared only when the Ti primer was present, indicating that the metal primer is responsible for binding the molecular layer to Au surface (the characteristic IR frequencies and peaks assignment for NAB on Ti surface are given in Table 2-2). Although the peak intensities for NAB in Figure 2-8B (Si/SiO$_x$/Cr/Au(100 nm)/Ti(5)/NAB front-side spectrum) are ~2-3x higher than that observed in Figure 2-8A (Si/Ti(5)/NAB/Au(100 nm) back-side spectrum), the absolute intensities cannot be directly compared due to differences in geometry and losses in the Si. However, the fact that the relative intensities of several different bands are unaltered by Au deposition provides strong evidence that the NAB layer survives metal deposition without significant changes in structure.

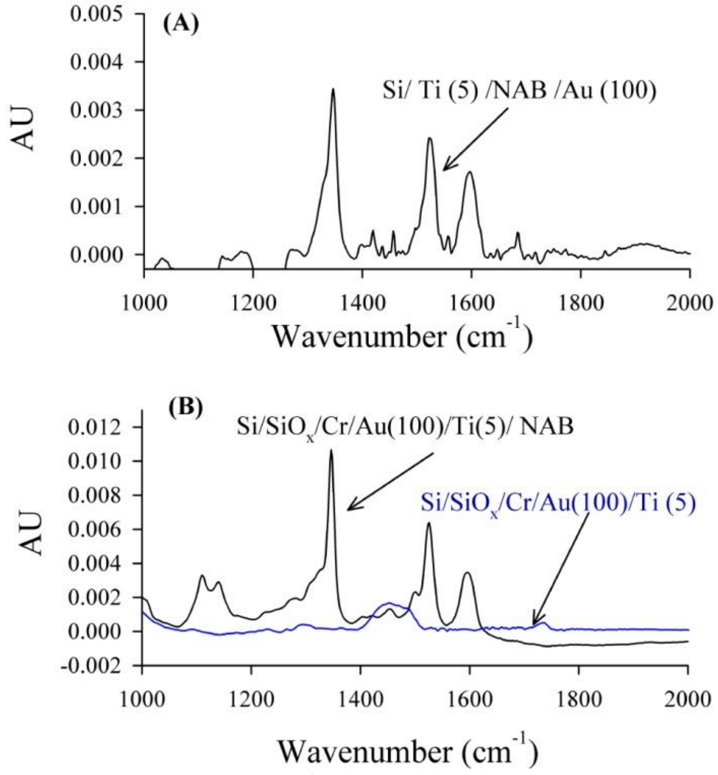

Figure 2-8. (A) Backside IRRAS for Si/Ti(5)/NAB/Au(100 nm), showing the molecular signature for NAB is clearly observed (see Scheme 2-1A) (B) Corresponding frontside IRRAS spectra for Au/Ti(5) (blue curve) and Au/Ti(5)/NAB (black curve), showing that the Ti primer does not have significant IR bands in this wavelength range and that the metal primer can be used to modify a gold surface (see Scheme 2-1B).

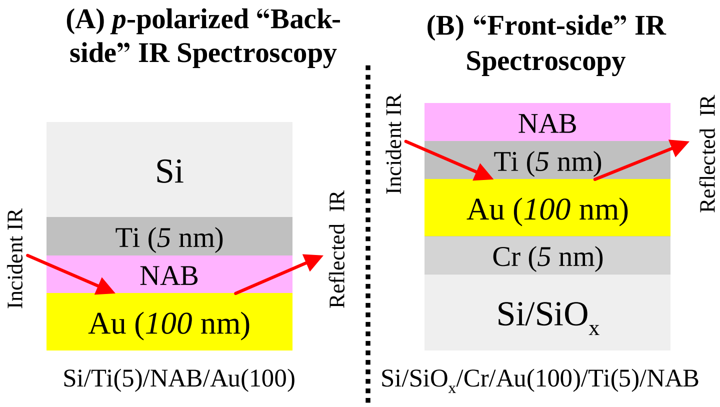

Scheme 2-1. Diagram of experimental set-up used to obtain IRRAS spectra. (A) In the "back-side" method, light passes through an IR-transparent Si, which is used at the substrate support, and is reflected from an optically dense layer of metal deposited directly onto the molecular layer. (B) In the "front-side" or conventional geometry, light must pass through any top contact materials in order to obtain a spectrum (no top layer is shown in Figure).

Ti/NAB	Assignment
1107	C-H/ NO_2
1136	Ph-N=N stretch
1346	NO_2 sym
1524	NO_2 asym+ C=C ring
1591	NO_2 + C=C ring

Table 2-2. IR frequencies and peak assignments for NAB.

In addition to Raman and IR spectroscopy, we have also used ultrathin primer metals to modify quartz substrates for use in UV/vis measurements. Figure 2-9A shows UV/vis absorbance spectra for quartz (Q), Q/Ti(5), Q/TiO_2(5) and Q/Ti(5)/NAB, all obtained in transmission geometry and referenced to air (as illustrated in Scheme 2-2). The TiO_2 layer was deposited directly from rutile as described previously[56], and is provided for comparison. The spectrum for Q shows a uniform and low absorbance throughout the wavelength range, with a slight increase in absorbance below 275 nm. When the Ti primer layer is deposited onto Q, the absorbance increases markedly throughout the UV/vis range, and a broad feature is observed between 200 and 325 nm. This indicates that the metal is reflective and increases the optical density of the substrate, but nevertheless the sample still maintains significant optical transparency. For comparison, when oxidized TiO_2 is deposited (from rutile) onto Q, the absorbance remains close to that for unmodified Q above 400 nm, but a band is observed at 285 nm, consistent with the literature for UV absorption by TiO_2 [57]. Oxidation of Ti metal can therefore be monitored by tracking the changes in UV-Vis spectrum of Q/Ti. After oxidation of a Q/Ti sample at 100 ^{o}C in oxygen for one day, the UV-Vis spectrum resembles that for Q/TiO_2 (from rutile), indicating that the thin layer of Ti metal can be oxidized to a passive layer of TiOx as shown in *Appendix 1 Figure 1A*. Oxidation of the Ti primer layer was studied in more detail using XPS, as discussed below. Finally, the Q/Ti(5)/NAB sample shows additional absorbance below 600 nm when compared to a Q/Ti(5) sample. In order to enhance the differences in absorbance between these two samples, a difference spectrum is plotted in Figure 2-9B as a subtraction of the Q/Ti(5) absorbance from that for Q/Ti(5)/NAB. As shown, a broad band is observed with a maximum at 340 nm, which has been attributed to chemisorbed NAB in previous studies[58].

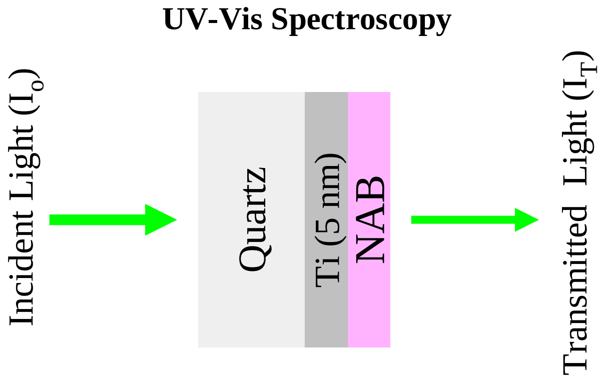

Scheme 2-2. In UV-vis, light passes through the transparent substrate and the transmitted light detected.

Comparison of λ_{max} of Q/Ti(5)/NAB from Figure 2-9B (340 nm) with that for NAB in hexane (λ_{max} = 330 nm)*[58]* and NAB adsorbed on optically transparent carbon (λ_{max} = 356)*[58]* indicates that a red-shift occurs when NAB is bonded to a substrate. This shift is most pronounced for carbon, but is still apparent for films deposited onto quartz via a Ti primer. The band broadening and red shift of the NAB spectrum can be attributed to either an electronic interaction between the substrate and NAB molecular layer or to lateral intermolecular interactions between chemisorbed NAB molecules on the surface.

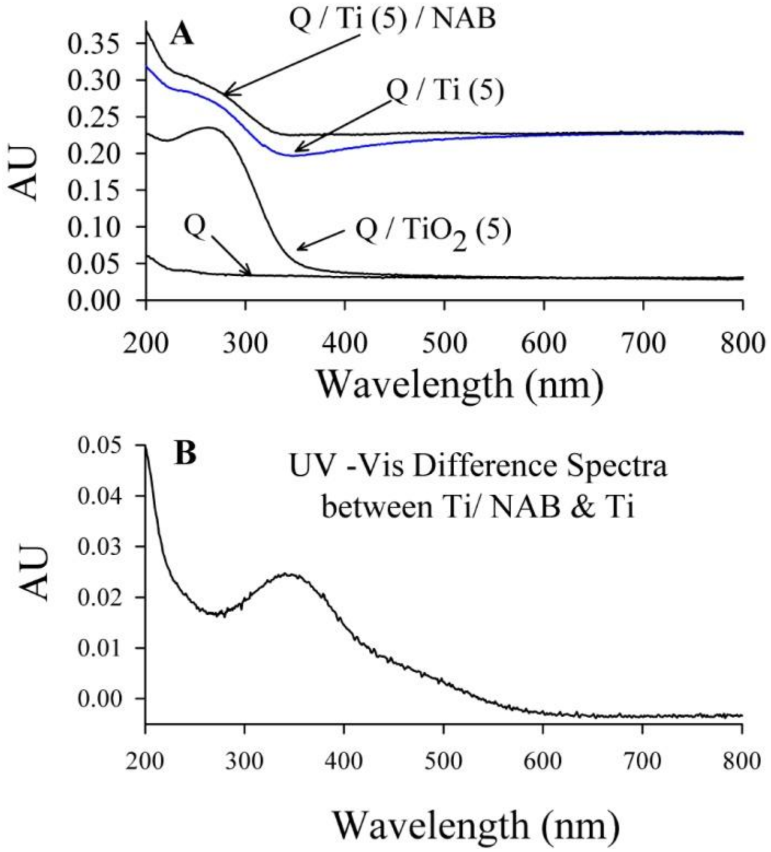

Figure 2-9. (A) Transmission UV-Vis spectra referenced to air for several samples, as indicated (see Scheme 2-2) (B) Difference spectrum plotted as the absorbance for Q/Ti(5)/NAB after subtracting the absorbance for Q/Ti(5), showing the absorbance band for NAB with a maximum at 340 nm.

In order to characterize the oxidation state of the Ti in the primer layer and to probe the nature of any chemical bonds between the molecule and the Ti primer, XPS was carried out on modified surfaces. A survey spectrum of Si/SiO$_x$/Ti is shown in Figure 2-10. Two prominent peaks are apparent: Ti(2*p*) and O(1*s*). The much smaller features such as Si(1*s*) at 102.8 eV are attributed to the SiO$_x$ substrate, while peaks for species such as C(1*s*) at 284.8 eV can generally be attributed to adventitiously adsorbed contaminants. Figure 2-11 shows a high resolution spectrum for this sample in the Ti region, where a deconvolution analysis was carried out that revealed five observable features. The deconovoluted bands correspond to TiO_2 [Ti($2p_{1/2}$) at 464.7 eV and Ti($2p_{3/2}$) at 459.2 eV]; TiO [454.6 eV and 460.8 eV]; and Ti_2O_3 [457.9 eV]*[37, 59]*. Importantly, no peak corresponding to fully reduced Ti (i.e. 453.8 eV)*[50, 60]* was observed. This result is attributed to the high reactivity of Ti with both residual chamber gases during deposition and reaction with atmospheric oxygen upon removal of the primed substrate from the evaporation chamber. In order to examine the oxidation process of the Ti primer layer, several samples were treated with oxygen and heat, and the oxidation state of the layers was again evaluated using XPS.

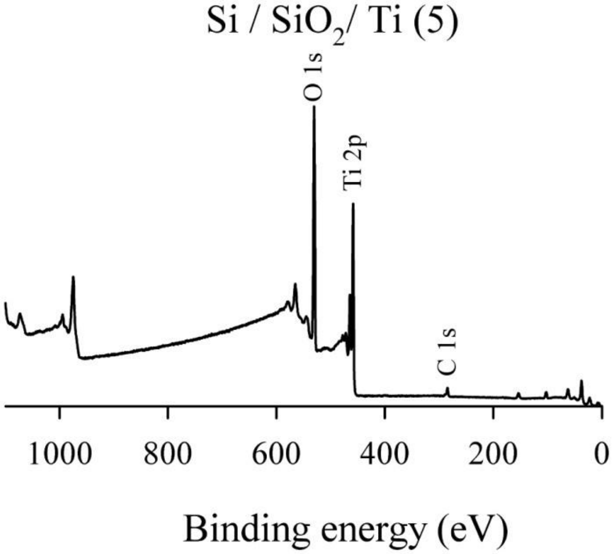

Figure 2-10. XPS survey spectrum of a $Si/SiO_2/Ti$ sample.

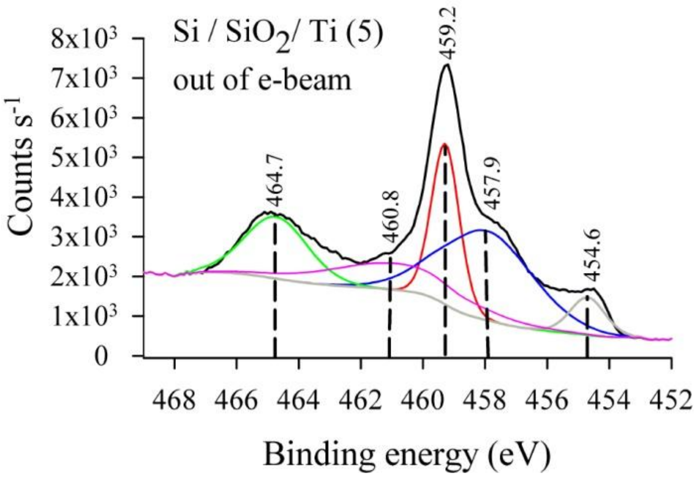

Figure 2-11. High-resolution XPS spectrum for Si/SiO_2/Ti with several species represented as best-fit curves from a deconvolution analysis. TiO_2: Ti($2p_{1/2}$) at 464.7 eV (green curve), Ti($2p_{3/2}$) at 459.2 eV (red curve); TiO: 454.6 eV (grey curve) and 460.8 eV (pink curve); and Ti_2O_3 peak at 457.9 (blue curve).

Figure 2-12 shows a high-resolution XPS spectrum of Si/SiO_2/Ti after exposure to pure oxygen (1 atm) for 24 h at 100 °C. Comparison of Figures 2-10 and 2-11 shows that after the treatment, most of the TiO_x is fully oxidized (i.e., occurs as TiO_2). For example, the peaks indicative of TiO_2, Ti($2_{p1/2}$) at 464.6 eV and Ti($2_{p3/2}$) at 459.0 eV, increase in intensity while those for less oxidized states of Ti are greatly diminished. In fact, only a small amount of Ti_2O_3 (indicated by the small peak at 457.3 eV) is indicated by the XPS data. Collectively, the results from analysis of the XPS spectra shown in Figures 2-10 – 2-12 indicate that a Ti metal primer layer is composed of a mixture of oxides of titanium, but that the film can be almost completely oxidized to TiO_2 by treatment at elevated temperatures in pure oxygen. In order to determine the nature of NAB bonding to the primer layer, XPS analysis was carried out on samples after deposition of the molecular layer.

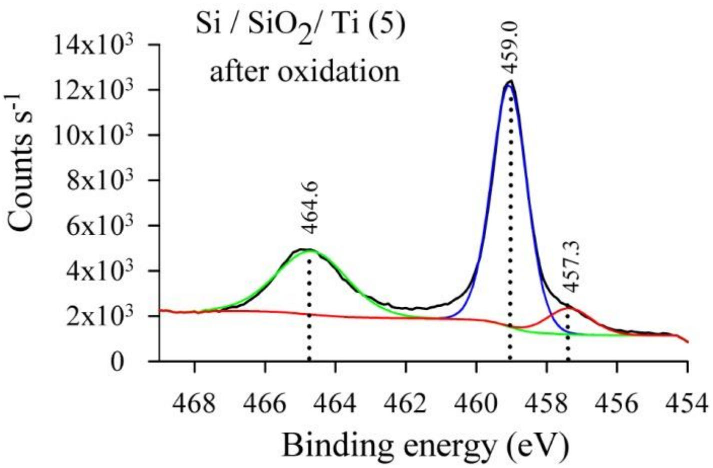

Figure 2-12. High-resolution XPS spectrum for Si/SiO$_2$/Ti after exposure to a pure oxygen atmosphere for 24 h at 100 °C. Ti(2$p_{1/2}$) at 464.6 eV (green curve) and Ti(2$p_{3/2}$) at 459.0 eV (blue curve) , Ti$_2$O$_3$ peak at 457.3 eV (red curve).

Figure 2-13A shows an XPS survey spectrum of Si/SiOx/Ti(5)/NAB (the SiOx is thermally grown) after treating the sample in a pure O$_2$ atmosphere for 24 hrs at 100 ^{o}C (treatment carried out after NAB modification). High-resolution scans of the Ti, N, and C regions are shown in Figures 2-13B, 2-13C, and 2-13D, respectively. First, the analysis of the Ti region shown in Figure 2-13B shows that the Ti is present mainly as TiO$_2$, as indicated by the peaks for Ti(2$p_{1/2}$) at 464.5 eV and Ti(2$p_{3/2}$) at 458.8 eV. Small peaks at 457.1 eV and 455.2 eV are attributable to residual Ti$_2$O$_3$ and TiO, respectively*[61]*. Moreover, no distinct peak for Ti bonded directly to carbon at 454.6 eV*[62]* was observed after careful analysis of the high resolution spectra. Second, strong N(1*s*) peaks are observed in Figure 2-13C centered at 400.1 eV (corresponding to the azo group of the NAB molecule), and 405.9 eV (representing the nitro group of NAB). The integrated peak areas for the azo and nitro peaks are 67.25 and 32.75, respectively, which closely corresponds to the 2/1 ratio expected for the NAB molecule. Third, the C(1*s*) peak in Figure 2-13D was deconvoluted by curve fitting (as shown in the

Figure) into two distinct peaks: one centered at 284.7 eV that corresponds to C(1*s*) of *sp*$_2$ hybridized carbon in the aromatic rings of the NAB molecule*[26, 63]*, and the other at 285.6 eV, which represents a phenyl carbon atom attached to either nitrogen or oxygen atoms*[64]*. It worth noting that the C(1*s*) peak in Figure 2-13A is much more intense that the adventitious carbon peak C(1*s*) in Figure 2-10. No evidence of a C-Ti bond at 281.5 eV*[63, 65]* was found. Although diazonium salt modification of Ti nanoparticles in solution reportedly results in formation of a Ti-C bond*[66]*, high resolution XPS analysis of Figure 2-13B and 2-13D did not provide any evidence for a Ti-C bond in the present case. Given the exposure of the Ti primer layer to the atmosphere before reaction with the diazonium reagent, the most likely surface bond is Ti-O-C rather than Ti-C.

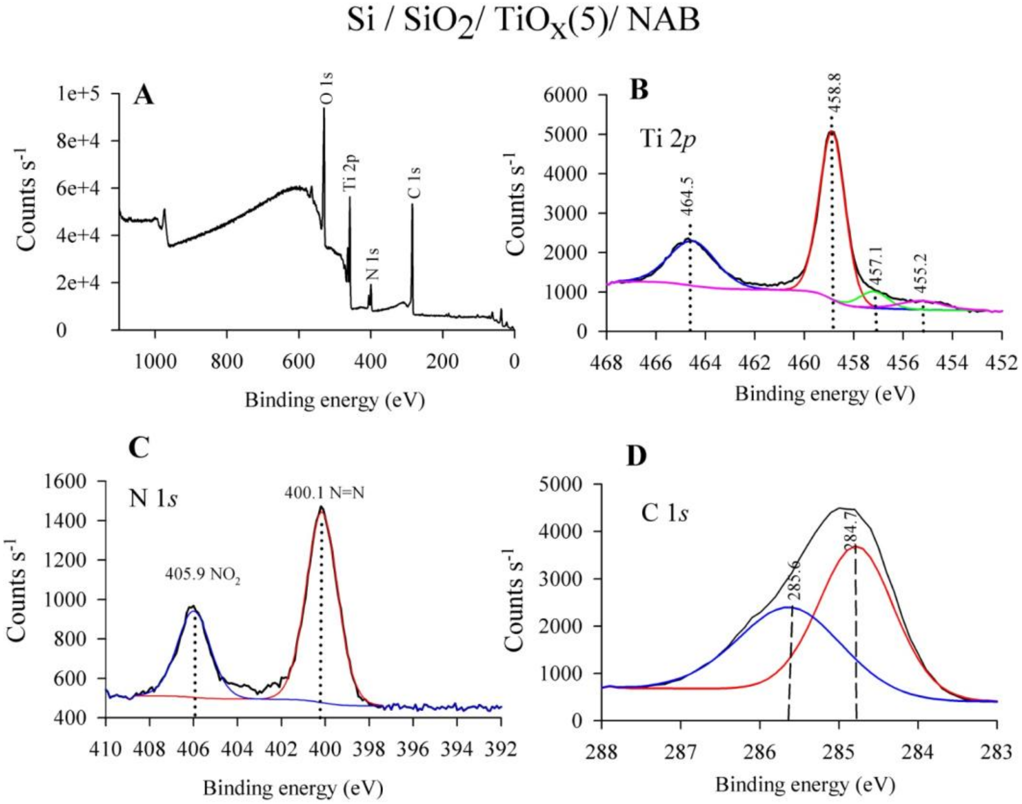

Figure 2-13. (A) Survey spectrum of a thermally oxidized Si wafer with a molecular layer of NAB deposited using a 5 nm Ti primer layer. **(B)** High-resolution spectrum in the Ti region showing peaks that correspond to Ti($2p_{1/2}$) at 464.5 eV (blue curve), Ti($2p_{3/2}$) at 458.8 eV (red curve), Ti_2O_3 peak at 457.1 eV (green curve), and Ti^{2+} at 455.2 eV (pink curve). **(C)** High-resolution spectrum in the nitrogen region showing an azo N(1*s*) peak at 400.1 eV (red curve) and a nitro N(1*s*) peak at 405.9 eV (blue curve). **(D)** High-resolution spectrum in the carbon region showing peaks that represent C(1*s*) bonded to either O or N at 285.6 eV (blue curve) and C(1*s*) in a phenyl group at 284.7 eV (red curve).

Various experimental conditions were tested in order to assess their impact on the amount of modifier obtained at the surface of the substrate. To this end, the intensity of the Raman signal was followed as several variables were altered, including the thickness of the Ti, the concentration of the NAB diazonium salt in solution, and the immersion time of the primed substrate. In general, the Raman signal increased monotonically with Ti thickness as shown in Figure 2-14, NAB concentration as shown in Figure 2-15, and immersion time as shown in Figure 2-16. For a 5 nm Ti thickness and 30 minutes immersion time (1 mM NAB DS), the NAB film thickness was estimated (using AFM scratching) to be 5.8 nm, indicating the formation of multilayers. Thus, the increase in the Raman signal as a function of Ti thickness, NAB concentration, and immersion time can tentatively be attributed to increases in the total amount of NAB on the substrate surface. Thus, the deposition conditions (and Ti thickness) should be optimized in order to achieve the desired thickness for a given application.

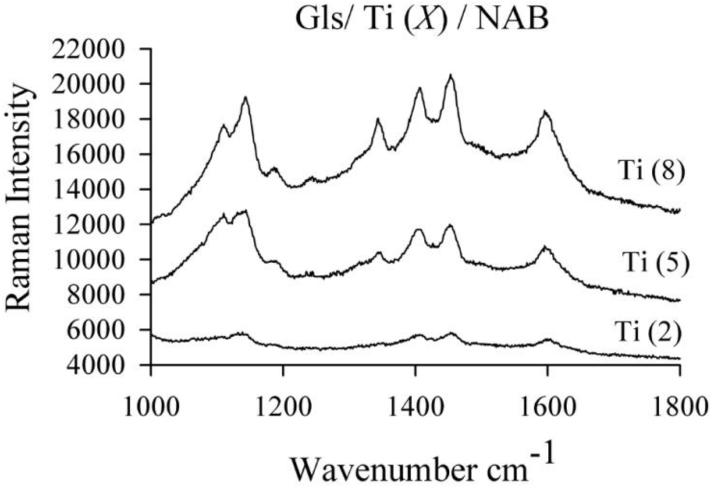

Figure 2-14. Raman Spectra of Glass/Ti (*x*)/NAB, where *x* is the thickness of Ti in nm.

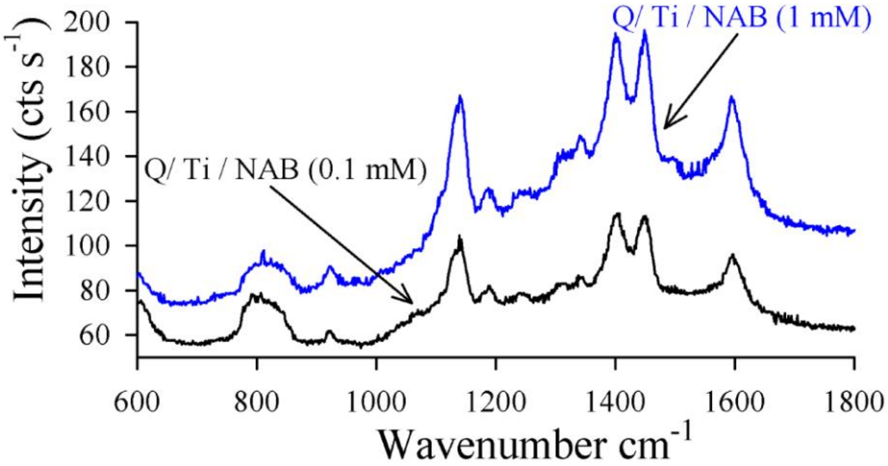

Figure 2-15. Raman Spectra of Q/ Ti / NAB, after immersion in 1 mM NAB DS in ACN (blue curve) and 0.1 mM NAB DS in ACN (black curve).

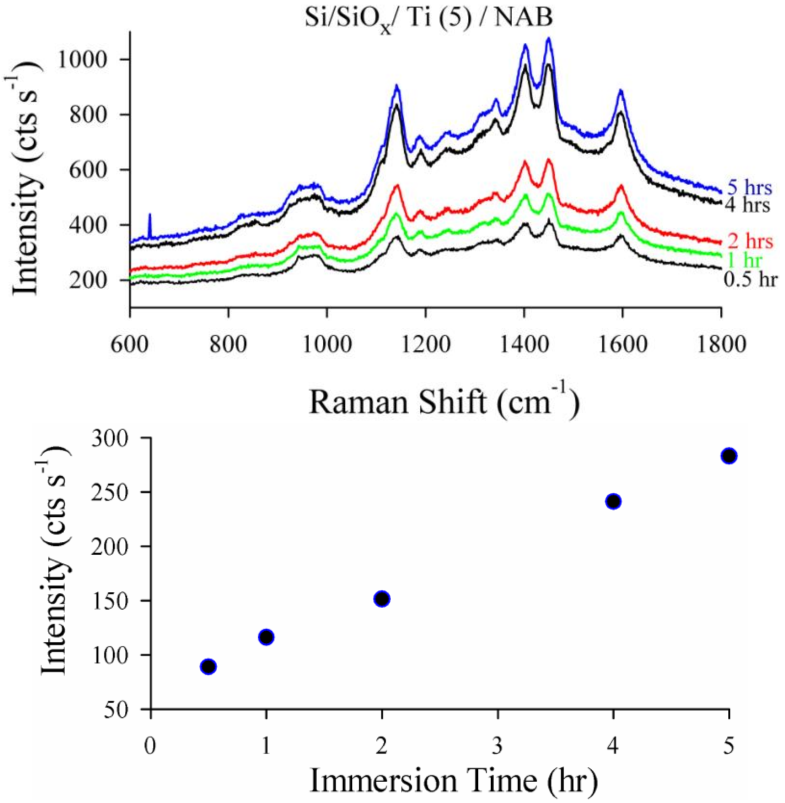

Figure 2-16. Top Figure is raw data of Raman Spectra of Q/ Ti /NAB, at different immersion time in 1mM NAB DS. Bottom Figure is Raman peak intensity of NAB molecular layer at 1600 cm^{-1} versus immersion time per hour in 1mM NAB DS solution.

The stability of the molecular layers deposited using a metal primer was tested by subjecting modified samples to different treatments and tracking any changes in the Raman spectral intensity. Samples of either Si/SiO_x/Ti(5)/NAB or Glass/Ti(5)/NAB were sonicated in various solvents, boiled in water, immersed into dilute acid or base, and heated. The experimental results are summarized in Table 2-3 and spectra are provided in Figure 2-17 to 2-22). As shown in the Table, the peak height for the Raman band at 1600 cm^{-1} (C=C stretch) decreased in all cases, but for many conditions the loss of intensity was small. For example, sonication in acetone or immersion in weak acids or base resulted in a decrease of less than 10%. A slightly larger decrease (12%) occurred after heating the sample at 200 °C in a low vacuum (~75 torr), and moderate decreases are noted for sonication in ACN for 30 min or immersion in boiling water for 60 min. The results in Table 2-3 indicate that the molecular layer adsorbed onto the substrate through the Ti metal primer can withstand moderately concentrated alkaline and acidic solutions. Moreover, the layers show good heat resistance, consistent with a similar study in which layers of NAB bound by covalent C–C bonds formed by modification of carbon surfaces using the spontaneous reduction of aryl diazonium salts were thermally stable up to 200 °C*[67]*. However, for the present case, a larger reduction in intensity was observed, indicating that the Ti-O-C bond appears to be less thermally stable than the C–C covalent bond.

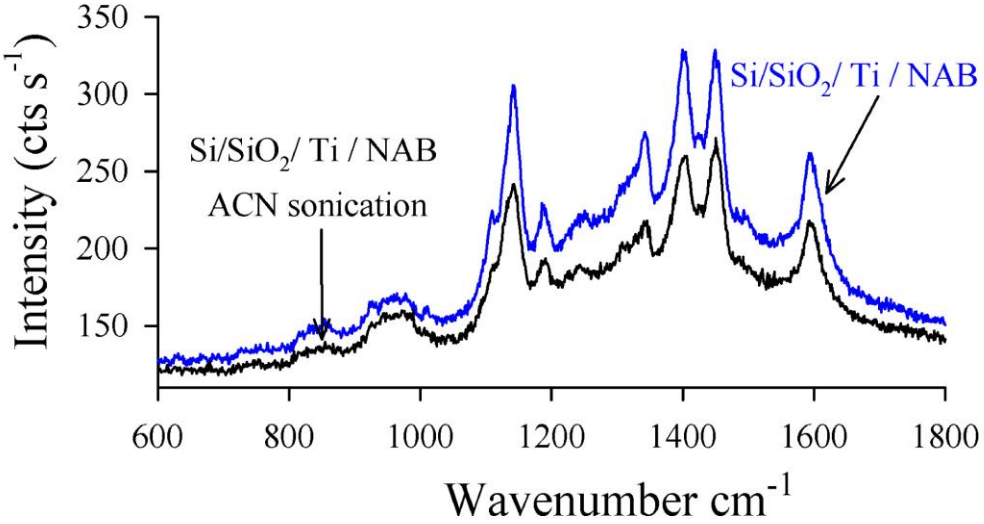

Figure 2-17. Raman spectra of NAB molecular layers deposited onto a glass substrate using a 5 nm Ti primer layer before and after sonication in acetone for 30 min.

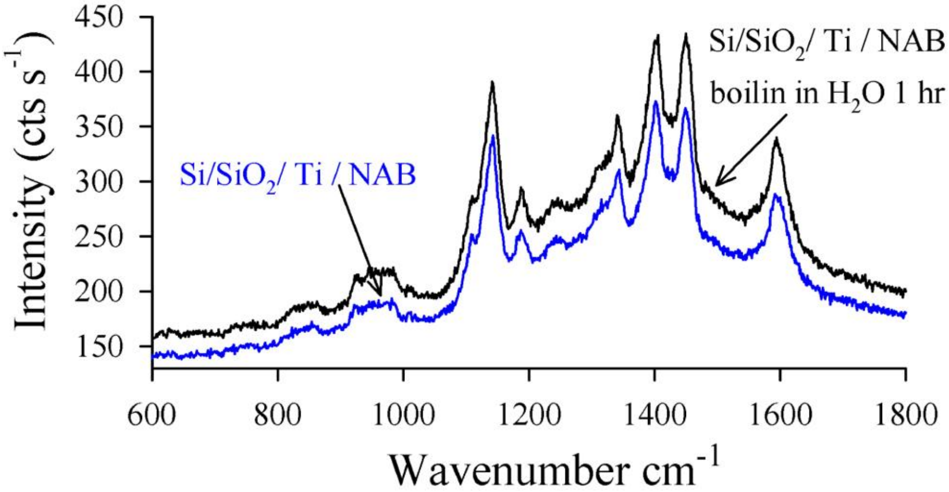

Figure 2-18. Raman Spectra of Si/SiO$_2$/ Ti / NAB, before (blue curve) and after (black curve) immersion in boiling water for 60 minutes.

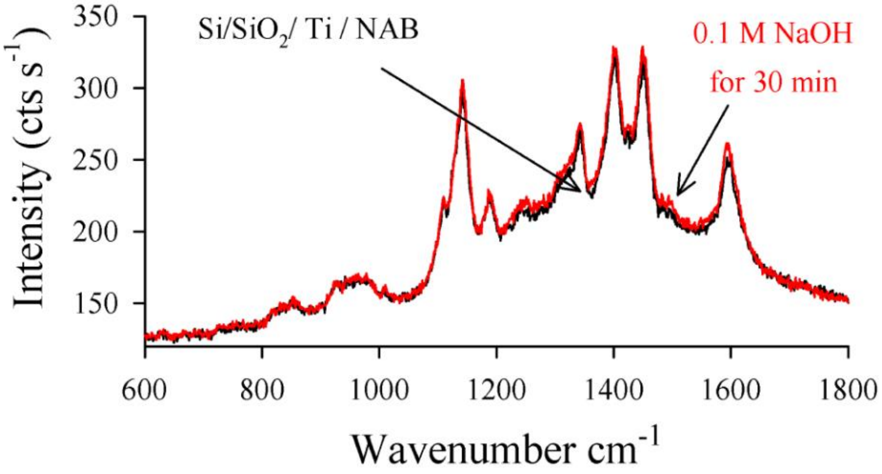

Figure 2-19. Raman Spectra of Si/SiO$_2$/ Ti /NAB (black curve), and same sample after immersion in 0.1 M NaOH for 30 minutes (red curve).

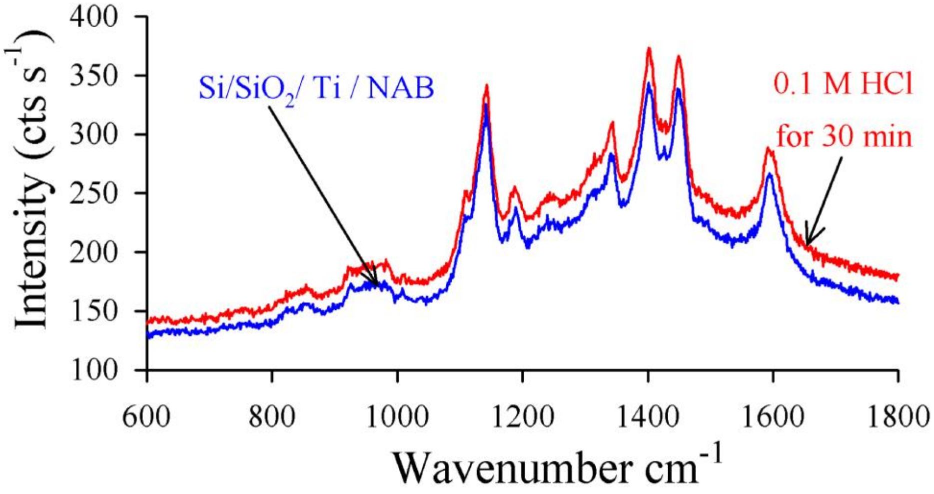

Figure 2-20. Raman Spectra of Si/SiO$_2$/ Ti /NAB (blue curve), and same sample after immersion in 0.1 M HCl for 30 minutes (red curve).

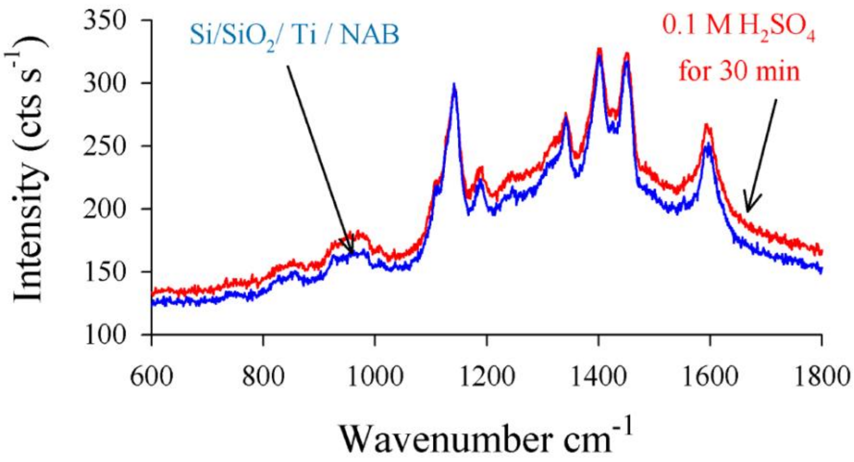

Figure 2-21. Raman Spectra of Si/SiO$_2$/ Ti /NAB (blue curve), and same sample after immersion in 0.1 M H_2SO_4 for 30 minutes (red curve).

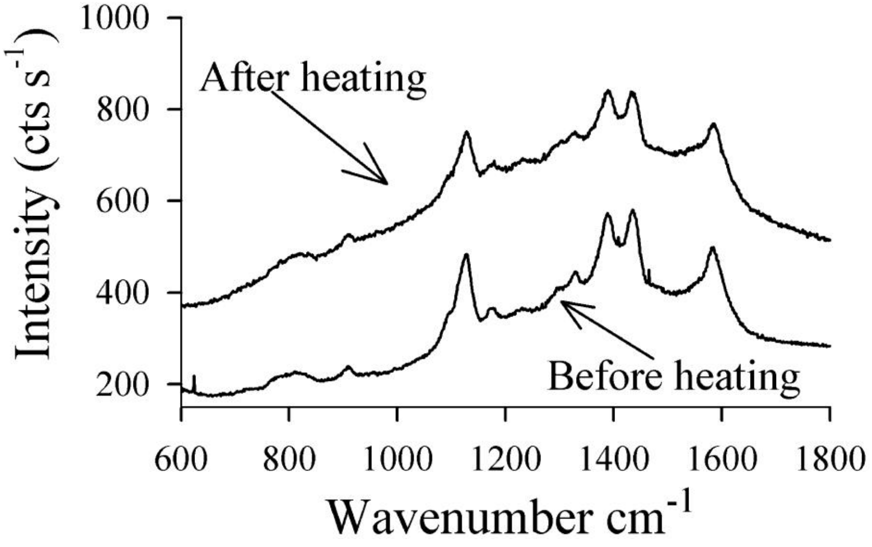

Figure 2-22. Raman Spectra of Q/ Ti /NAB before heating and the same sample after heating at 200 °C for 2 hours.

Table 2-3. Summary of Raman intensity changes for NAB after different treatments. The intensity of the band at ~1600 cm^{-1} (C=C ring stretch) was used as a diagnostic.

	Before treatment	**After treatment**	**% change**
Sonication in acetone	32.6 (cts s^{-1})	30.2 (cts s^{-1})	-7.3%
Sonication in ACN	89.4 (cts s^{-1})	61.9 (cts s^{-1})	-30.7%
Boiling water	119.8 (cts s^{-1})	91.4 (cts s^{-1})	-23.7%
0.1M NaOH	87.7 (cts s^{-1})	83 (cts s^{-1})	-5.3%
0.1M HCl	93.6 (cts s^{-1})	90.1 (cts s^{-1})	-3.7%
0.1M H_2SO_4	85.6 (cts s^{-1})	81.1 (cts s^{-1})	-5.2%
Heating at 200 ^oC	192.8 (cts s^{-1})	169.7 (cts s^{-1})	-12%

As noted earlier, Raman spectroscopy has been reported previously for characterization of molecular layers at buried interfaces and in molecular electronic junctions by using thin, partially transparent top metal contacts*[8, 9, 37, 68]*. In order to increase the versatility of these experiments, we have applied Ti primer-derived adlayers to study the effect of depositing top contact materials on the structural integrity of the molecular layer. Figure 2-23A shows Raman spectra of Q/Ti(5)/NAB obtained from both the front-side (red curve) and from the back-side (through the primed quartz substrate, blue curve). Figure 2-23B shows Raman spectra of Q/Ti(5)/NAB after deposition of a thin (10 nm) transparent top metal (Au) obtained from both the front-side (through the 10 nm Au, red curve) and from the back-side (through the primed quartz substrate, blue curve). As shown, the molecular signature for NAB (see Figure 2-1 and Table 2-1) is apparent in both cases, indicating that the molecular layer is not seriously damaged by metal deposition. In Figure 2-23B, The Raman peak intensity for

NAB (and the quartz feature at 807 cm^{-1}) obtained in front-side mode is less than that observed in back-side mode, due to attenuation of the incident and scattered light by the Au layer in frontside mode. Thus, it is apparent there is a sensitivity advantage in collecting the spectrum through the "backside" (i.e., the quartz layer), of ~ 40%.

Recall that in Figure 2-8, the IRRAS spectrum obtained from the backside of a Si/Ti(5)/NAB/Au(100 nm) substrate also showed that the NAB layer can easily be detected, supporting the Raman results that Au deposition does not destroy the molecular layer. A further demonstration of the utility of back-side Raman is demonstrated in Figure 2-23C, where both front- and back-side Raman spectra are shown for a Q/Ti(5)/NAB sample with 100 nm of Au deposited directly onto the molecular layer (as illustrated in Scheme 2-3). The backside spectrum obtained through the Q substrate (blue curve) is similar to that observed for only 10 nm of Au (Figure 2-23B, blue curve), in both structure and intensity. However, the front-side spectrum obtained (Figure 2-23C, red curve) shows that no molecular signature for the molecular layer was obtained. Since the backside spectrum (blue curve) shows a clear Raman spectrum for NAB, the "disappearance" of the spectrum in front-side mode (for the same sample) must be due to minimal transmission through the 100 nm thick Au layer. Thus, molecular layers buried under relatively thick top contact materials and minimal optical transparencies can be characterized using the back-side method if an appropriate substrate support is used (e.g., quartz for Raman or Si for IR).

In order to test the generality of these observations, a different top contact material was chosen. Figure 2-24 compares the backside spectra of Q/Ti(5)/NAB before and after deposition of 50 nm of Ag. Metals such as Ag, Cu, and Ti can reduce NAB, as evidenced by a reduction in the ratio of the peak intensity at 1406 cm^{-1} to that at 1451 cm^{-1} (N=N stretches)*[3, 9]*. Indeed, in Figure 2-24, the ratio decreases from 1.1 to 0.99 after Ag deposition. A detailed analysis of metal deposition effects on molecular layers will be reported in the next chapter.

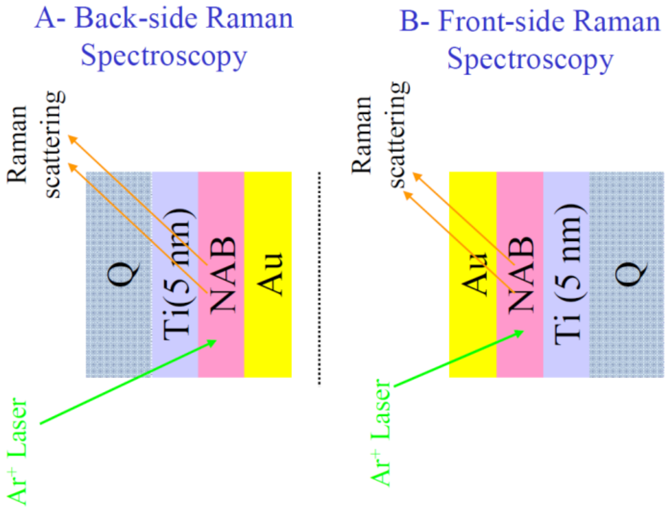

Scheme 2-3. Schematic diagram of geometries employed in obtaining Raman spectra. (A) “Back-side” geometry, where the incident light passes through the substrate support (Quartz) before exciting the molecule. (B) “Front-side” geometry where light must pass through a metallic top layer.

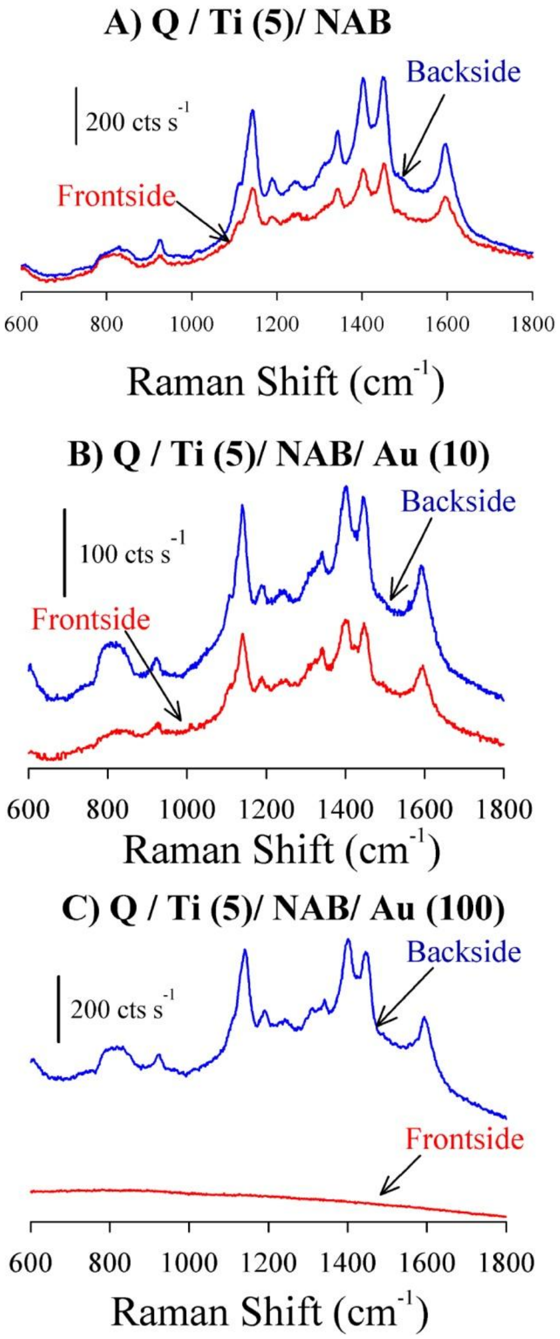

Figure 2-23. (A) Raman Spectra of Q/Ti(5)/NAB collected from top side (red curve), and quartz or "backside" (blue curve). **(B)** Raman spectra of Q/Ti (5)/NAB after deposition of 10 nm Au metal directly on top of the molecular layer, collected from top side (red curve), and quartz or "backside" (blue curve). (**C**) Raman spectra of Q/Ti (5)/NAB after deposition of 100 nm Au metal, collected from top-side (red curve), and backside (blue curve).

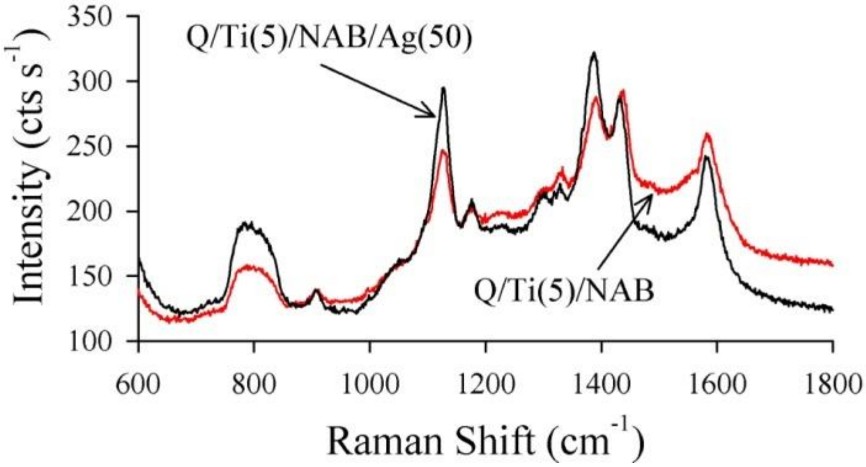

Figure 2-24. Raman spectrum of Q/Ti (5)/NAB obtained from the backside before (red curve) and after (black curve) deposition of 50 nm Ag.

2.4 Summary

This work has shown that ultrathin layers of reactive metals can be used as primers to prepare a variety of substrate materials for modification via the reduction of aryl diazonium ions. The molecular layers bonded to the surface of the Ti primer are stable to sonication, aqueous acids and bases and moderate heating. Diazonium reagents can be made from a wide variety of aromatic amines, and the Ti primer was shown to enable bonding of diazonium-derived radicals to glass, quartz, Au, Al, and polyethylene. Since Ti is quite reactive and bonds to both conducting and insulating surfaces, its use as a primer should be applicable to a wide variety of materials. Modification of transparent substrates enables UV-Vis, FTIR, and Raman spectroscopy for characterization of the molecular layer at buried interfaces after deposition of a top contact regardless of its thickness. An NAB molecular layer bonded to quartz through a Ti primer layer shows minimal changes to its Raman spectrum following deposition of up to 100 nm of Au by direct electron-beam deposition.

2.5 Endnotes

A version of chapter II has been published. Amr M. Mahmoud, Adam J. Bergren, Richard L. McCreery, *Analytical Chemistry* **2009**, 81, 6972.

2.6 References

[1] H. B. Akkerman, B. De Boer, *Journal of Physics: Condensed Matter* **2008**, *20*, 013001.

[2] R. McCreery, *Chemistry of Materials* **2004**, *16*, 4477.

[3] R. L. McCreery, *Analytical Chemistry* **2006**, *78*, 3490.

[4] B. de Boer, M. M. Frank, Y. J. Chabal, W. R. Jiang, E. Garfunkel, Z. Bao, *Langmuir* **2004**, *20*, 1539.

[5] W. Wang, T. Lee, M. Kamdar, M. A. Reed, M. P. Stewart, J. J. Hwang, J. M. Tour, *Molecular Electronics Iii* **2003**, *1006*, 36.

[6] Y. Selzer, D. Allara, *Annual Reviews of Physical Chemistry* **2006**, *57*, 593.

[7] A. P. Bonifas, R. L. McCreery, *Chemistry of Materials* **2008**, *20*, 3849.

[8] K. W. Hipps, J. Dowdy, J. J. Hoagland, *Langmuir* **1991**, *7*, 5.

[9] A. M. Nowak, R. L. McCreery, *Journal of the American Chemical Society* **2004**, *126*, 16621.

[10] A. J. Bergren, M. D. Porter, *Journal of Electroanalytical Chemistry* **2007**, *599*, 12.

[11] G. A. Edwards, A. J. Bergren, M. D. Porter, (Ed: C. G. Zoski), Elsevier, New York **2007**, 295.

[12] D. A. Rider, K. D. Harris, D. Wang, J. Bruce, M. D. Fleischauer, R. T. Tucker, M. J. Brett, J. M. Buriak, *ACS Appl. Mater. Interfaces* **2009**, *1*, 279.

[13] Z. Q. Xu, Z. G. Qi, A. Kaufman, *Electrochemical and Solid State Letters* **2003**, *6*, A171.

[14] A. J. Bergren, K. D. Harris, F. J. Deng, R. L. McCreery, *Journal of Physics-Condensed Matter* **2008**, *20*, 374117.

[15] R. P. Kalakodimi, A. M. Nowak, R. L. McCreery, *Chemistry of Materials* **2005**, *17*, 4939.

[16] F. Anariba, J. K. Steach, R. L. McCreery, *Journal of Physical Chemistry B* **2005**, *109*, 11163.

[17] J. Pinson, F. Podvorica, *Chemical Society Reviews* **2005**, *34*, 429.

[18] A. Adenier, E. Cabet-Deliry, A. Chausse, S. Griveau, F. Mercier, J. Pinson, C. Vautrin-Ul, *Chemistry of Materials* **2005**, *17*, 491.

[19] F. Mirkhalaf, J. Paprotny, D. J. Schiffrin, *Journal of the American Chemical Society* **2006**, *128*, 7400.

[20] A. Ricci, C. Bonazzola, E. J. Calvo, *Physical Chemistry Chemical Physics* **2006**, *8*, 4297.

[21] G. Chamoulaud, D. Belanger, *Journal of Physical Chemistry C* **2007**, *111*, 7501.

[22] G. Z. Liu, T. Bocking, J. J. Gooding, *Journal of Electroanalytical Chemistry* **2007**, *600*, 335.

[23] Q. M. Pan, M. Wang, W. T. Chen, *Chemistry Letters* **2007**, *36*, 1312.

[24] A. Adenier, N. Barre, E. Cabet-Deliry, A. Chausse, S. Griveau, F. Mercier, J. Pinson, C. Vautrin-Ul, *Surface Science* **2006**, *600*, 4801.

[25] J. Ghilane, M. Delamar, M. Guilloux-Viry, C. Lagrost, C. Mangeney, P. Hapiot, *Langmuir* **2005**, *21*, 6422.

[26] B. L. Hurley, R. L. McCreery, *Journal of the Electrochemical Society* **2004**, *151*, B252.

[27] P. Allongue, M. Delamar, B. Desbat, O. Fagebaume, R. Hitmi, J. Pinson, J. M. Saveant, *Journal of the American Chemical Society* **1997**, *119*, 201.

[28] F. Anariba, S. H. DuVall, R. L. McCreery, *Analytical Chemistry* **2003**, *75*, 3837.

[29] S. Baranton, D. Belanger, *Journal of Physical Chemistry B* **2005**, *109*, 24401.

[30] M. Delamar, R. Hitmi, J. Pinson, J. M. Saveant, *Journal of the American Chemical Society* **1992**, *114*, 5883.

[31] R. L. McCreery, *Chemical Reviews* **2008**, *108*, 2646.

[32] P. Abiman, G. G. Wildgoose, R. G. Compton, *International Journal of Electrochemical Science* **2008**, *3*, 104.

[33] M. P. Stewart, F. Maya, D. V. Kosynkin, S. M. Dirk, J. J. Stapleton, C. L. McGuiness, D. L. Allara, J. M. Tour, *Journal of the American Chemical Society* **2004**, *126*, 370.

[34] A. Scott, D. B. Janes, C. Risko, M. A. Ratner, *Applied Physics Letters* **2007**, *91*, 033508.

[35] C. Combellas, M. Delamar, F. Kanoufi, J. Pinson, F. I. Podvorica, *Chemistry of Materials* **2005**, *17*, 3968.

[36] D. J. Garrett, J. Lehr, G. M. Miskelly, A. J. Downard, *Journal of the American Chemical Society* **2007**, *129*, 15456.

[37] A. M. Nowak, R. L. McCreery, *Analytical Chemistry* **2004**, *76*, 1089.

[38] A. Jaiswal, K. G. Tavakoli, S. Z. Zou, *Analytical Chemistry* **2006**, *78*, 120.

[39] C. A. Richter, C. A. Hacker, L. J. Richter, O. A. Kirillov, J. S. Suehle, E. M. Vogel, *Solid-State Electronics* **2006**, *50,* 1088.

[40] A. Scott, C. A. Hacker, D. B. Janes, *Journal of Physical Chemistry C* **2008**, *112*, 14021.

[41] F. Anariba, U. Viswanathan, D. F. Bocian, R. L. McCreery, *Analytical Chemistry* **2006**, *78*, 3104.

[42] Y. S. Jun, X. Y. Zhu, *Journal of the American Chemical Society* **2004**, *126*, 13224.

[43] H. B. Liu, N. V. Venkataraman, T. E. Bauert, M. Textor, S. J. Xiao, *Journal of Physical Chemistry A* **2008**, *112*, 12372.

[44] G. L. Fisher, A. V. Walker, A. E. Hooper, T. B. Tighe, K. B. Bahnck, H. T. Skriba, M. D. Reinard, B. C. Haynie, R. L. Opila, N. Winograd, D. L. Allara, *Journal of the American Chemical Society* **2002**, *124*, 5528.

[45] A. V. Walker, T. B. Tighe, O. M. Cabarcos, M. D. Reinard, B. C. Haynie, S. Uppili, N. Winograd, D. L. Allara, *Journal of the American Chemical Society* **2004**, *126*, 3954.

[46] D. K. James, J. M. Tour, *Analytica Chimica Acta* **2006**, *568*, 2.

[47] A. Troisi, M. A. Ratner, *Journal of Chemical Physics* **2006**, *125*, 214709.

[48] L. H. Yu, C. D. Zangmeister, J. G. Kushmerick, *Physical Review Letters* **2007**, *98*, 206803.

[49] J. Ramsey, S. Ranganathan, R. L. McCreery, J. Zhao, *Applied Spectroscopy* **2001**, *55*, 767.

[50] K. W. Vogt, P. A. Kohl, W. B. Carter, R. A. Bell, L. A. Bottomley, *Surface Science* **1994**, *301*, 203.

[51] J. F. Scott, S. P. S. Porto, *Physical Review* **1967**, *161*, 903.

[52] C. G. R. Heald, G. G. Wildgoose, L. Jiang, T. G. J. Jones, R. G. Compton, *ChemPhysChem* **2004**, *5*, 1794.

[53] Y. L. Brama, Y. Sun, S. R. K. Dangeti, M. Mujahid, *Surface & Coatings Technology* **2005**, *195*, 189.

[54] Mária Péter, François Furthner, Jochem Deen, Wim J.M. de Laat, E. R. Meinders, *Thin Solid Films* **2009**, *517*, 3081.

[55] S. Hilbrich, W. Theiss, R. ArensFischer, O. Gluck, M. G. Berger, *Thin Solid Films* **1996**, *276*, 231.

[56] J. Wu, K. Mobley, R. L. McCreery, *Journal of Chemical Physics* **2007**, *126*, 024704.

[57] X. Y. Li, D. S. Wang, Q. Z. Luo, J. An, Y. H. Wang, G. X. Cheng, *Journal of Chemical Technology and Biotechnology* **2008**, *83*, 1558.

[58] H. Tian, A. J. Bergren, R. L. McCreery, *Applied Spectroscopy* **2007**, *61*, 1246.

[59] S. O. Saied, J. L. Sullivan, T. Choudhury, C. G. Pearce, *Vacuum* **1988**, *38*, 917.

[60] A. Lebugle, U. Axelsson, R. Nyholm, N. Martensson, *Physica Scripta* **1981**, *23*, 825.

[61] A. R. Gonzalezelipe, G. Munuera, J. P. Espinos, J. M. Sanz, *Surface Science* **1989**, *220*, 368.

[62] C. D. Wagner, L. H. Gale, R. H. Raymond, *Analytical Chemistry* **1979**, *51*, 466.

[63] A. N. Macinnes, A. R. Barron, J. J. Li, T. R. Gilbert, *Polyhedron* **1994**, *13*, 1315.

[64] J. L. Jordan, P. N. Sanda, J. F. Morar, C. A. Kovac, F. J. Himpsel, R. A. Pollak, *Journal of Vacuum Science & Technology a-Vacuum Surfaces and Films* **1986**, *4*, 1046.

[65] H. Ihara, Kumashir.Y, A. Itoh, K. Maeda, *Japanese Journal of Applied Physics* **1973**, *12*, 1462.

[66] D. Ghosh, S. Pradhan, W. Chen, S. W. Chen, *Chemistry of Materials* **2008**, *20*, 1248.

[67] M. Toupin, D. Belanger, *Journal of Physical Chemistry C* **2007**, *111*, 5394.

[68] J. J. Hoagland, J. Dowdy, K. W. Hipps, *Journal of Physical Chemistry* **1991**, *95*, 2246.

Chapter 3

Towards Integrated Molecular Electronic Devices: Characterization of Molecular Layer Integrity during Fabrication Processes

3.1 Introduction

Integration of electronic components into miniaturized platforms that can accomplish targeted functions has led to the ubiquitous implementation of integrated circuits (ICs). The low cost, high device density and ability to package microchips and incorporate them into durable products has led to a thriving semiconductor industry with sales exceeding $225 billion (USD) in 2009. This level of success relies largely on the ability to fabricate the electronic circuits in a highly parallel fashion. The performance of the various electronic devices is also linked to density: the ability to fit an ever larger number of transistors in a given area leads to increased computing power, larger memory capacities, etc. However, it has been long recognized that Moore's law cannot be continued indefinitely: the actual size of a single device will approach nanoscopic and then molecular and atomic scale dimensions. There is a high degree of uncertainty in the behaviour of nanoscale devices, as the properties of such systems can deviate significantly from those of bulk materials. For these reasons and others, there has been a strong interest in the developing field of molecular electronics*[1-7]*, which investigates charge transport through molecules that are configured as circuit components. In addition to serving as a guide for understanding the electronic behaviour of molecules, there is also the possibility of using the electronic properties of the molecules themselves in new and interesting ways. Thus, the development of molecular electronic devices may result in enhancements in performance or functions that are not possible with current semiconductor technology.

For any embodiment of molecular electronics to serve a real-world function, integration of molecular and semiconductor devices is essential. However, conventional semiconductor processing often involves the use of harsh fabrication conditions that are acceptable for inorganic materials, but pose potential problems for the “soft” organic molecules used in molecular devices. Thus, any practical molecular electronics platform must be amenable to the necessary procedures required to produce a fully integrated electronic chip. To this end, there are two possibilities: 1. integration of molecular devices into a hybrid circuit composed of both the molecular device and traditional semiconductor-based circuits, and, 2. the production of a fully molecular circuit in a massively parallel fashion. In either case, there are numerous fundamental issues that require investigation. In the case of a hybrid chip consisting of both traditional and molecular devices, it is critical to ensure that the molecular device can withstand the conditions required for integration.

Various platforms have been developed to study the electrical characteristics and charge transport mechanism in molecular junctions*[8-12]*. In many cases, these studies have greatly contributed to our understanding of charge transport in molecular devices, but are currently limited to research labs. For example, liquid metal top contacts*[8, 13-15]* and STM*[9]* or AFM tips*[12]* have been used to avoid the harsh conditions associated with vapour deposition of metallic contacts. These techniques have enabled the construction of molecular junctions using labile molecular self-assemblies, but are not readily adaptable to massively parallel fabrication. In order to overcome these limitations, a method using conducting polymer top contacts that is capable of producing devices based on Au/thiol self assembled monolayers (SAM) on a massively parallel scale (i.e., 20,000 molecular junctions on one wafer) has been demonstrated*[10]*. However, SAM-based devices have limited thermal stability. In two different studies, the upper limit of the temperature process window of SAM-based molecular junctions on gold and Si has been determined to be 50 °C and 100 °C, respectively*[16, 17]*. Another critical requirement is making contact with the molecular layers without inducing structural damage. Various techniques for avoiding damage to SAM-based devices have been published*[4, 18]* and numerous reports exist that discuss post-deposition damage to molecular layers*[19-22]*.

Our research group has pursued an alternative approach for junction fabrication that relies on covalent modification of carbon electrodes through the electrochemical reduction of aryl diazonium salts*[11, 14, 23-27]*. There are several advantages to this method: the layers are anchored by a carbon-carbon bond that is much stronger (~3.5 eV) than Au-S linkages (~1.9 eV)*[3]*, the thickness can be controlled in the 1-5 nm range by changing the conditions during the electrochemical reduction step*[24, 28-30]*, and a variety of aromatic structures can be accommodated*[11]*. To complete the circuit, metallic copper*[11, 23, 27, 31]* is deposited to form a cross-junction through direct electron-beam evaporation. These devices display yields exceeding 90% and have excellent reproducibility. In addition, they survive at least 10^9 potential cycles in ambient air*[24],* and they are scalable (i.e., the current scales with junction dimension from at least 400 x 400 μm to 16 x 16 μm*[32]*).

In this chapter, we describe analytical techniques to investigate the stability of diazonium-derived molecular layers on carbon undergoing various fabrication procedures, including metal deposition, lithography, etching, and temperature excursions. Several top contact metals were deposited using direct electron beam evaporation, and the integrity of the molecular layer was investigated by performing spectroscopic characterization through a partially transparent support, as described in chapter 2. In addition, the molecular layer was examined with Raman spectroscopy and X-ray photoelectron spectroscopy (XPS) after removal of the top contact by etching with appropriate etchants for each metal used. Using similar procedures, the layer integrity was investigated after subjecting the samples to conditions that are commonly encountered in semiconductor integration such as UV lithography and packaging procedures. Finally, the thermal stability of finished molecular junctions was investigated.

3.2 Experimental Section

Acetonitrile, acetone, and isopropanol (HPLC grade, Fischer Scientific) were used as received. Water was purified by a Millipore system (18 MΩ, < 3 ppb TOC). 4-nitroazobenzene (NAB) 4'-diazonium tetrafluoroborate salt and 4-trifluoromethylphenyl (TFMP) diazonium tetrafluoroborate salt were prepared as described in detail elsewhere*[33-35]*. Diced Si/SiO_2 chips (18 x 15 mm^2 chips, 300 nm of thermally grown SiO_2) were used as substrates for all experiments except "back-side" Raman spectroscopy. In the later case, 25 x 25 x 0.22 mm^3 quartz microscope cover slips (Technical Glass Products, Inc.) were used as an optically transparent support. Si/SiO_2 and Quartz (Q) substrates were cleaned by sonication in acetone, isopropanol and finally ultrapure water for 10 minutes each, and then dried in a directed stream of N_2. Pyrolyzed photoresist film (PPF) was prepared as outlined previously*[11, 36]*. Briefly, a positive photoresist (AZ P4330-RS, AZ Electronic Materials, Somerville, NJ) was spun onto clean substrates at 6000 rpm for 40 seconds (two coats) followed by soft baking at 90 ^{o}C for 15 minutes. The photoresist was then pyrolyzed by heating the samples in a tube furnace to 1025 °C (held for 60 min) under a constant flow of forming gas (5% H_2 in N_2 at 100 mL/min). For XPS and AFM analysis, a blanket sheet of PPF was used. Optically transparent PPF (OTPPF) was prepared on quartz (Q) using diluted photoresist (5% v/v photoresist in propylene glycol methyl ether acetate as solvent)*[37, 38]*. For junction fabrication, PPF was patterned prior to pyrolysis using standard photolithography: exposure to UV radiation for 120 s through a Cr photo-mask with 0.5 mm stripes followed by development with diluted (1:2) AZ 400K developer.

Electrochemical modification of both PPF and Q/OTPPF with either NAB or TFMP diazonium salts were carried out using a 1 mM diazonium salt solution in acetonitrile with 0.1 M tetrabutylammonium tetrafluoroborate ($TBABF_4$) as the supporting electrolyte. Surface modification was carried out using four cyclic scans from +0.4 to -0.6 V versus Ag/Ag^+ at a sweep rate of 0.2 V s^{-1}. We reported previously*[11]* that this procedure yields an NAB film with a thickness of 4.5 ± 0.3 nm, as determined with an AFM "scratching" technique*[28]*, and the same NAB deposition conditions were used for all of the junctions reported herein. TFMP was bonded to PPF using the same procedure for XPS samples, but the molecular layer thickness was not verified independently. Following modification, PPF/NAB and Q/OTPPF/NAB samples were rinsed with acetonitrile and then dried in a directed stream of N_2. Modified PPF substrates were then transferred to an electron-beam evaporator (Kurt J. Lesker PVD75), where various metals were deposited directly onto the surface of the molecular layer. For metals other than Ti, the chamber was evacuated to ~ 2.2 x 10^{-6} Torr before beginning deposition. For Ti, a lower pressure (2.2 x 10^{-7} Torr) was used to minimize its oxidation with residual gases in the chamber. For junction fabrication, metal was deposited through shadow mask (0.6 mm) oriented perpendicular to PPF strips to result in a cross-bar junction. The deposition rate was 3 Å/s, except for Pt (0.1 Å/s), and the metal thickness was measured by a quartz crystal microbalance (QCM). Junctions are designated from bottom to top with the metal layer thicknesses in nm in parentheses. For example, PPF/NAB/Cu(45) indicates a 4.5 nm NAB layer on 1-2 μm thick PPF with a Cu top contact 45 nm thick. In all cases where current-voltage behavior was determined, the junction area was 3.0×10^{-3} cm^2.

Electrical characterization of molecular junctions utilized a three- or four-wire configuration*[11, 23]* where the top contact is the virtual ground, with the drive voltage (V_{drive}) applied to PPF (thus, all voltages reported herein indicate the voltage of the PPF relative to the top contact). The third and fourth probes are used to sense voltages on the PPF and top contact in order to compensate for ohmic losses (*iR* drop) due to the resistances of the leads. Data collection was done using a National Instruments 6111 or 6120 DAQ board controlled by LabView software to execute voltage sweeps and record the resulting current after amplification by an SRS 570 current amplifier.

Raman spectra were collected using a custom built spectrometer*[39]* equipped with an Argon ion laser (514.5 nm), a 50 mm f/1.8 Nikon camera collection lens, a 2000 groove/mm holographic reflection grating, and a back scattering geometry that employs an Andor back-thinned charge-coupled device (CCD) detector cooled to -80° C*[40]*. Incident power is ~19 mW and the signal is integrated for 30 s (unless stated otherwise). In order to perform characterization of NAB after metal deposition by XPS and AFM, the NAB molecular layer was exposed through wet chemical etching of the top metal. 0.5 M $FeCl_3$, KI/I_2 solution (100 g KI + 25 g I_2 dissolved in 1L deionized H_2O), and 5% w/w HF were applied for a maximum of 10 s to etch Cu, Au, and Ti, respectively. The thermal stability of modified PPF was investigated by heating PPF/NAB in Ar gas (Praxair 4.8 grade, 99.998% pure with O_2 < 0.5 ppm) or vacuum (~2 x 10^{-6} torr) for 30 minutes (room temperature to 500 ^{o}C) followed by Raman spectroscopy. Completed electronic junctions were heated under vacuum for 5 minutes at temperatures ranging from 25 to 400 ^{o}C and then removed from vacuum and tested at room temperature.

To study the compatibility of modified PPF with photolithographic processes, a standard photoresist (HPR 504) was spun onto PPF/NAB and PPF/TFMP samples at 4000 rpm for 40 seconds, followed by UV exposure for 3 seconds (365 nm and 404 nm, total intensity 65.3 mW/cm^2), and developer (Microposit 354). After developing, the sample was rinsed with deionized water and dried in a stream of N_2. Modified PPF samples were characterized by Raman and XPS before and after this procedure. Finally, encapsulation of a separate set of completed devices with parylene was carried out. First, the junction was wired using silver epoxy so that the electrical properties could be probed before and after coating with 0.3 μm parylene N (PDS-2010 LABCOTER® 2, Speciality Coating System). To ensure effective encapsulation, the electrical characterization was measured after immersing coated samples in water and 0.5 M $FeCl_3$ solution for 10 minutes.

3.3 Results and Discussion

3.3.1 Electrical Characterization Using Different Top Contacts

Figure 3-1 shows current density-voltage (*J-V*) curves for PPF/NAB junctions made using four different top metal contacts: Cu (blue curve), Au (red curve), Ti (black curve), and Pt (green curve). There are significant differences among junctions made with different metals. First, when Pt is used as the top contact, the *J-V* response is linear and behaves similar to a short circuit with direct metal to PPF contact, while all of the other curves show some degree of non-linearity. Second, as shown in Figures 3-2 and 3-3, there are significant differences in the reproducibility of the junctions made using Cu and Au. The electrical behaviour of Cu devices has been shown in the past to depend on molecular structure and molecular layer thickness*[11, 23, 24]*. In addition, reproducibility is typically very high and yields exceed 90%*[11, 24, 32]*. The present results are comparable to previous reports in terms of curve shape and magnitude, yield, and reproducibility (the rsd for $J_{0.5\ \mathrm{V}}$ for 12 PPF/NAB/Cu junctions is 12%). Furthermore, these results are similar to those obtained with "soft" deposition through surface diffusion of copper on NAB molecular layer*[41]*. However, the electrical behaviour of PPF/NAB/Au junctions is less reproducible than that of the Cu devices (Figure 3-3 shows the rsd for $J_{0.5\mathrm{V}}$ is ~55% for Au devices). These results may be attributed to partial penetration of Au into the NAB molecular layer as discussed below.

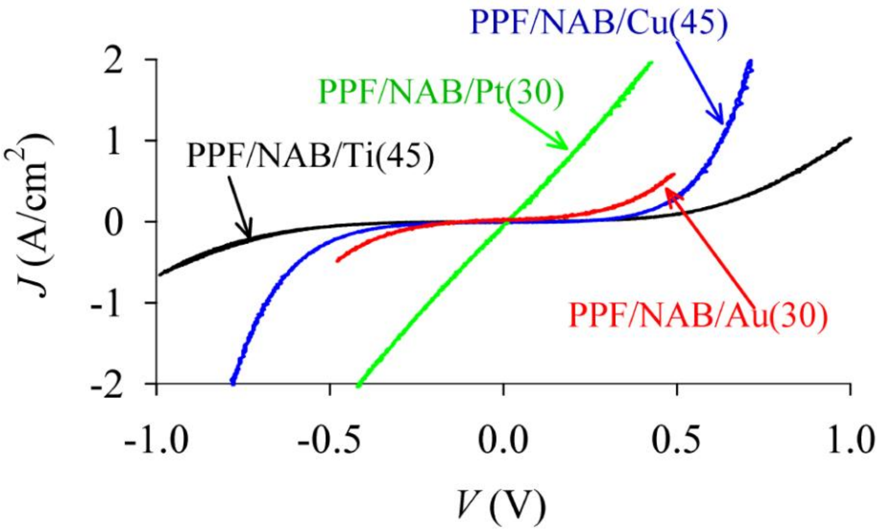

Figure 3-1. J-V curves of Si/SiO$_2$/PPF/NAB/metal junctions for four different top metals contact (Cu, Au, Ti, and Pt). Scan rate 1000 V/s.

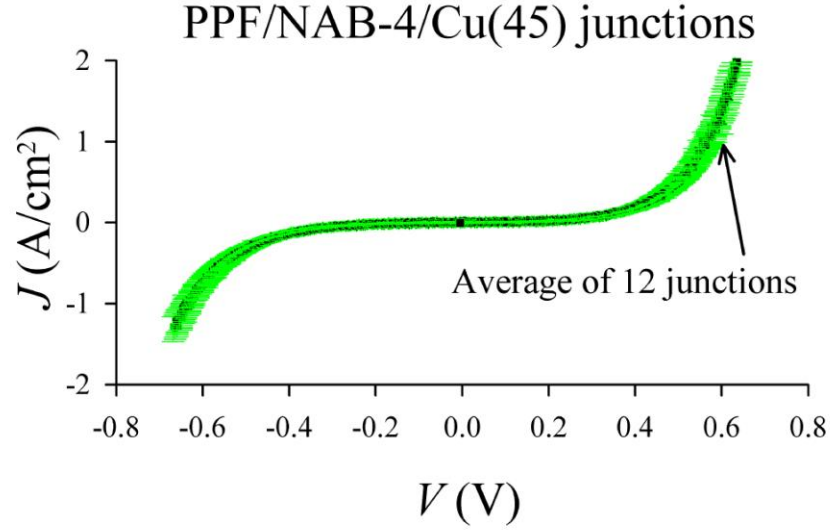

Figure 3-2. The average J-V curve of 12 Si/SiO$_2$/PPF/NAB/Cu(45) junctions (black curve) with the error bar (± 1 standard deviation) shown.

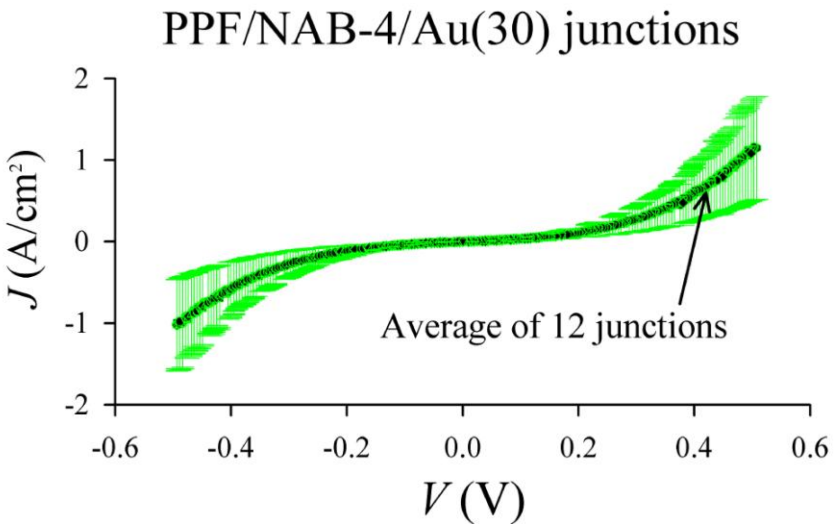

Figure 3-3. The average *J*-*V* curve of 12 Si/SiO_2/PPF/NAB/Au(30) junctions (black curve) with the error bar (± 1 standard deviation) shown.

Third, Ti metal is a highly reactive species that can react with residual gases in the evaporation chamber, forming, for example, titanium oxides*[42-44]* which are less conductive than Ti metal. This leads to the junction conductance being at least partially controlled by the oxidized Ti, complicating the analysis. In addition, the highly reactive Ti metal can undergo reactions with the molecular layer itself, possibly altering or destroying it*[19, 21, 45]*. In order to address these various possibilities, we have determined the thermal stability of NAB chemisorbed on PPF, determined the temperature rise at the location of the substrate in the vacuum chamber during deposition, used spectroscopic characterization through transparent supports to track any structural changes in the molecular layer during fabrication processes, and used XPS and AFM to characterize structural and morphological changes to the molecular layer after removal of the top contact metals.

3.3.2 Temperature Stability of NAB on PPF

In order to determine the thermal stability of a diazonium-derived molecular layer on carbon, a sample of PPF/NAB was heated to 400 °C in vacuum (~2 x 10^{-6} torr) for 30 minutes. Figure 3-4 shows Raman spectra for this sample before and after heating, and Table 3-1 lists the relative peak intensities. The absence of a significant change in absolute or relative Raman intensities indicates that no observable structural change occurred at 400 ^{o}C for 30 minutes in vacuum. This indicates that any procedure that results in a temperature rise of ~400 ^{o}C or less in vacuum is not expected to cause thermally-induced damage to an NAB layer bonded to PPF.

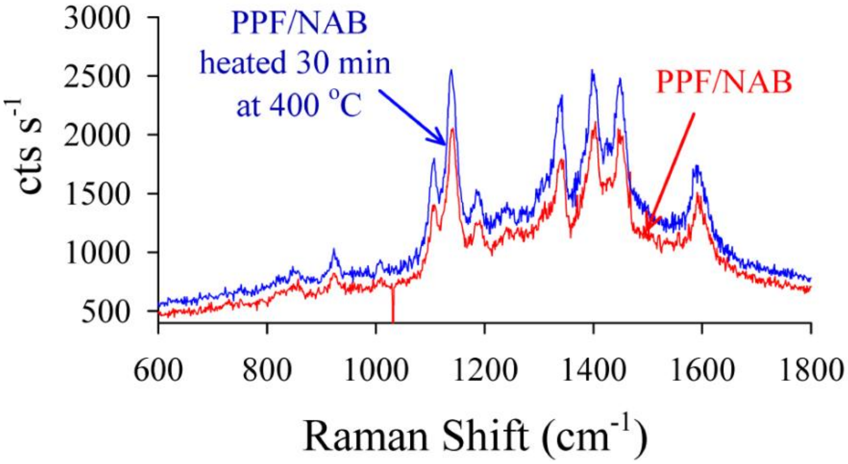

Figure 3-4. Raman Spectra for PPF/NAB before (red curve), and after (blue curve) heating for 30 minutes to 400 ^{o}C in a ~ 2 x10^{-6} torr vacuum.

Raman peak(cm^{-1})	**Peak Ratio Initially Relative to Raman Peak at 1600 cm^{-1}**	**Peak Ratio after Heating Relative to Raman Peak at 1600 cm^{-1}**
1140	1.32	1.39
1339	0.77	0.95
1401	0.83	0.72
1450	1.22	1.33

Table 3-1. Ratio of Raman peaks heights relative to the Raman peak height at 1600 cm^{-1} of PPF/NAB sample initially and after heating the sample to 400 ^{o}C in vacuum (~2 x 10^{-6} torr).

While stability may vary with molecular structure, the current results indicate that the surface C-C bond of diazonium-derived adlayers on PPF is stable to > 400 ^{o}C in vacuum. However, we note that the NAB film is less stable in an Argon atmosphere than in vacuum, with changes in the Raman spectrum observable above 250 ^{o}C as shown in Figure 3-5. The structural changes in Ar are presumably due to Ar collisions with the NAB surface or reactions with residual oxygen in the Ar atmosphere. These results are consistent with those of Toupin and Belanger*[46]*, who reported thermal stability of similar molecular layers up to 250-500 ^{o}C, depending on atmosphere and exposure time.

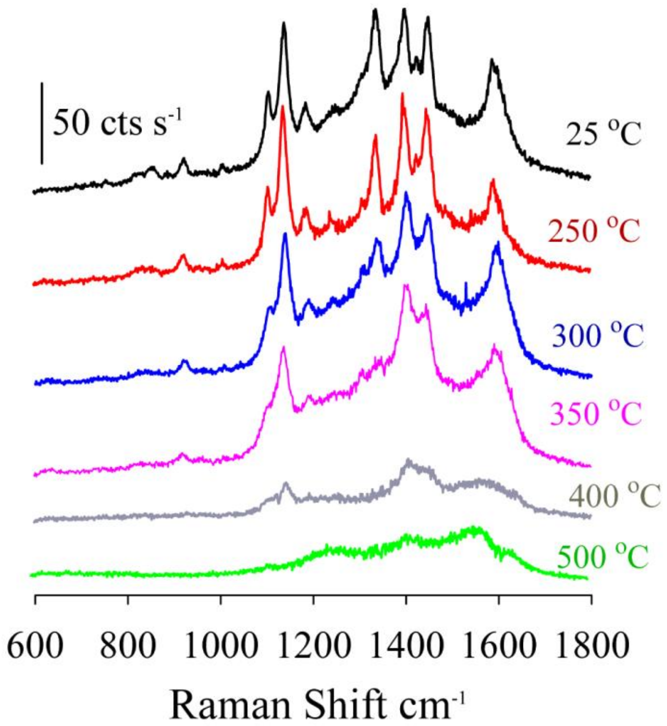

Figure 3-5. Raman Spectra of Si/SiO$_2$/PPF/NAB after heating the sample for 30 min in Ar gas for the indicated temperature.

3.3.3 Spectroscopic Characterization of Molecular Layer Integrity

Chapter 2 described “backside” Raman spectroscopy to investigate the integrity of an NAB molecular layer on an ultrathin titanium primer layer supported on quartz after deposition of Au and Ag metals*[47]*. Here we apply the same method, but use partially transparent PPF on quartz to more closely replicate conditions in PPF/molecule/metal molecular junctions. This approach enables a direct correlation between Raman characterization and electrical measurements, since the latter are carried out using thick PPF films as the substrate. Figure 3-6 shows the Raman spectra of Q/OTPPF/NAB initially (red curves) and after deposition of four different top metal contacts: Cu (A), Au (B), Ti (C) and Pt (D), and intensity changes are tabulated in Table 3-2. Peak assignments and vibrational analysis of NAB bonded to carbon surfaces has been reported previously*[43, 48, 49]*. Analysis of Figure 3-6 shows that deposition of both Cu and Au has minimal effects on the Raman spectrum for NAB.

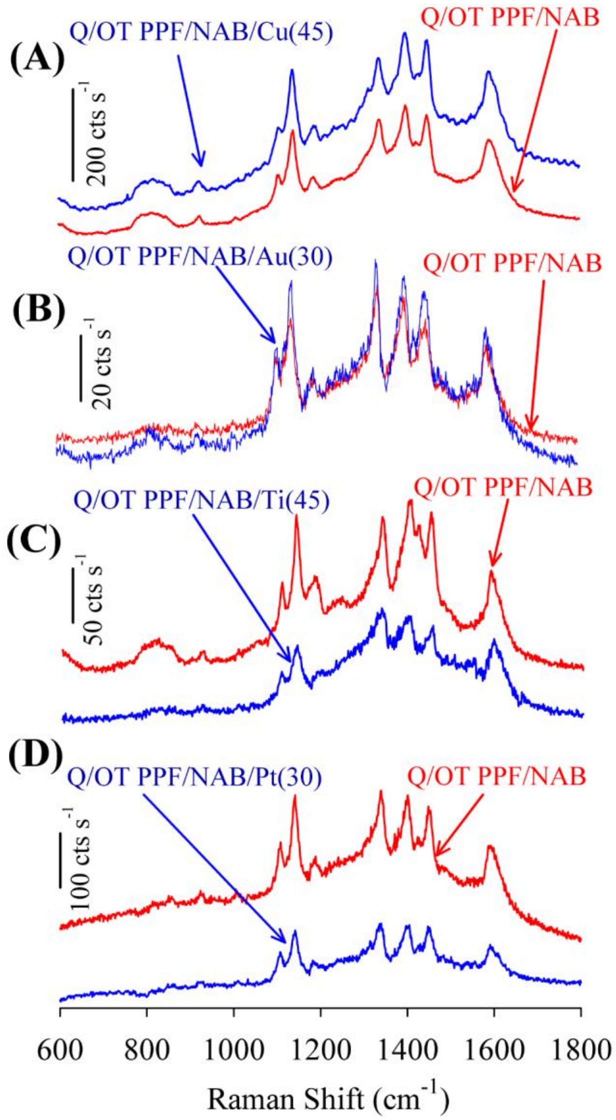

Figure 3-6. "Backside" Raman Spectra of Q/OTPPF/NAB before (red curves) and after (blue curves) deposition of the indicated thickness (in nm) of Cu (A), Au(B), Ti(C) and Pt (D).

Top Metal Contact	% reduction in Raman peak height 1600 cm^{-1}	Initial 1402/1450 cm^{-1} intensity ratio	1402/1450 cm^{-1} intensity ratio after metal deposition
Cu (45)	9.8%	0.86	0.77
Au (30)	3.6%	0.88	0.74
Ti (45)	63%	0.92	0.89
Pt (30)	61%	0.92	0.92

Table 3-2. The reduction of Raman peak intensity at 1600 cm^{-1} and the ratios for 1402/1450 cm^{-1} (azo stretches) before and after top contact deposition for PPF/NAB samples.

Although the change in optical geometry accompanying metal deposition makes intensity comparisons semi-quantitative, it is clear that Ti and Pt have a much greater effect on the NAB spectrum than Au and Cu. In addition, Raman spectra obtained for Au, Cu, and Ti after removal of the top contact metal by etching show minor changes in the case of Au and Cu compared to the unmetallized samples, but nearly complete loss of the spectrum for Ti as shown in Figure 3-7. This result indicates that some structural changes and/or a decrease in the surface coverage of NAB molecules occurred during Ti and Pt deposition. The melting points of Pt and Ti are significantly higher than those of Au and Cu, and the higher resulting target temperature may be responsible for greater damage to the molecular layer during Pt and Ti deposition.

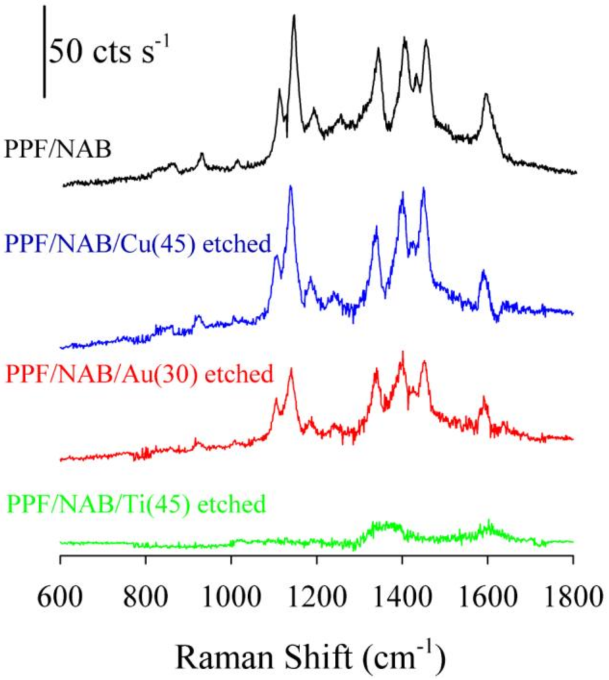

Figure 3-7. Raman Spectra of Si/SiO_2/PPF/NAB initially and after etching Cu(45) Au(30), and Ti(45).

In the case of Ti, the effect observed in Figure 3-6 is larger than that reported previously*[44]*, due to the significantly greater thickness of Ti in the current case (45 nm compared to 1-3 nm). In any case, it is clear that Ti metal must be used with caution, as it is possible that this reactive metal can cause damage to the molecular layer*[19, 21]*. The larger effect of Pt on the NAB layer compared to Cu and Au likely results from the heat released during condensation of the metal on the molecular layer surface. The Pt heat of evaporation (ΔH_{vap} 509.9 kJ/mol = 5.28 eV) is higher than Au (ΔH_{vap} 341.9 kJ/mol = 3.46 eV) and Cu (ΔH_{vap} 304.3 kJ/mol = 3.15 eV)*[50]*. Thus, it is possible that Pt deposition on the molecular layer results in significantly greater local heating from Pt condensation compared to Cu and Au. Recalling that PPF/NAB/Pt junctions behave as short circuits (i.e., a linear *J*-*V* curve is observed without any signature from the molecule), the results in Figure 3-6 indicate that Pt deposition causes enough damage to result in direct PPF-Pt contact. To provide further insight into the mechanism for damage to the molecular layer, we have obtained Raman and XPS spectra of molecular layers after removal of the metal top contact using etchants appropriate for each metal.

Figure 3-8 shows high-resolution XPS spectra of the N_{1s} region for samples of PPF/NAB obtained before metal deposition (red curves) and after removing the metal with a chemical etch (black curves). Also shown are the spectra obtained after PPF/NAB (non-metallized) is exposed to the wet etching procedure for each case (blue curves). The blue spectra indicate that any spectral changes detected upon metal etching originate from metal deposition and are not artefacts of the wet etching process. Note that spectra are shown for Au, Cu, and Ti, as etching of these metals is straightforward. However, in the case of Pt metal, the etching procedure is considerably more aggressive and was not attempted. In each of the three cases where metal was removed by etching, residual metal was undetected by XPS indicating < 1 atom % remaining on the surface.

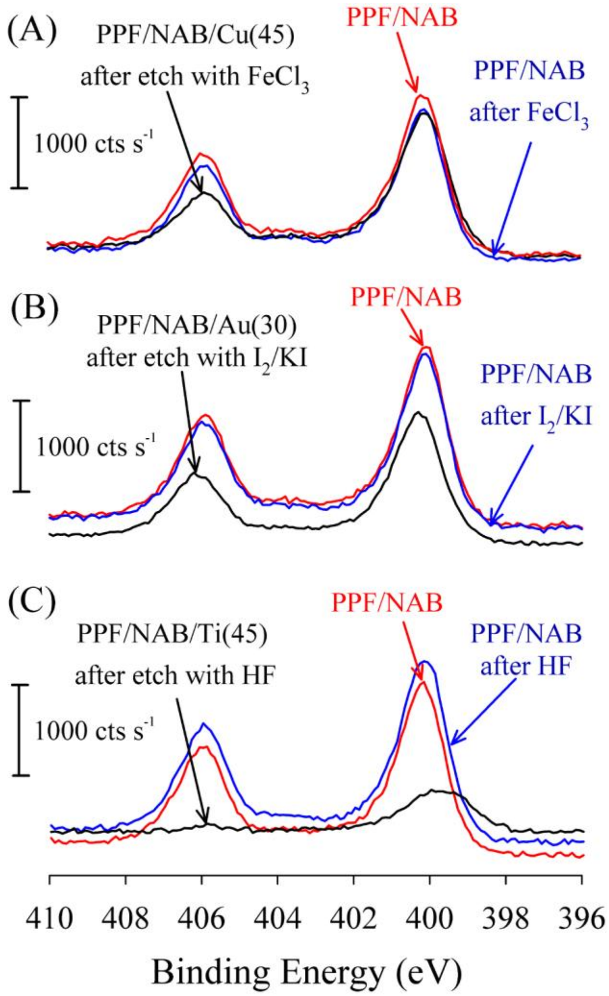

Figure 3-8. High-resolution XPS spectra of N_{1s} region for three samples of Si/SiO_2/PPF/NAB. The red spectra were obtained before treatment, the black spectra after metal deposition and etching and the blue spectra after immersion of Si/SiO_2/PPF/NAB samples in etchant solution without metal deposition. (A) Cu (45 nm) and etchant $FeCl_3$; (B) Au (30 nm) and etchant KI/I_2 ;(C) Ti (45 nm) and etchant HF.

The N_{1s} region of the NAB spectrum is composed of two peaks: one centered at 400.2 eV, corresponding to the azo group, and a second peak at 405.9 eV, corresponding to the nitro group. The similarity of the red and blue spectra in Figure 3-8 indicates that wet etching processes (with $FeCl_3$, KI/I_2 and HF) by themselves affect neither the ratio nor the intensity of the two N_{1s} peaks. This result also indicates good chemical stability of the covalently bonded layer, as reported previously*[51]*. Table 3-3 presents a summary of the XPS atomic N/C ratio for both the azo (400.2 eV) and nitro (405.9 eV) peaks before and after metal etching.

	N/C of N 400.2 eV (azo)		N/C of N 405.9 eV (nitro)	
Metal	Initially	After metal etch	Initially	After metal etch
Cu	0.10	0.11	0.058	0.033
Au	0.11	0.10	0.057	0.045
Ti	0.12	0.03	0.068	0.002

Table 3-3. XPS atomic ratios of N_{1s} of NAB molecular layer on PPF substrate initially and after deposition and etching of the metal top contact.

Direct evaporation of Cu (45 nm) onto NAB (black curve in Figure 3-8A) does not measurably affect the azo group of NAB molecules (the $N_{400.2}/C$ ratio is 0.10 before and 0.11 after). However, the nitro peak (405.9 eV) undergoes a decrease (the $N_{405.9}/C$ ratio is 0.058 before and 0.033 after). This reduction in the peak intensity may be attributed to either reduction of the nitro group by Cu deposition*[43, 49]* or loss of peripheral nitro groups. For the case of Au deposition on PPF/NAB, there is minimal change in the N/C ratio or the relative intensities of the 400 and 406 eV N_{1s} peaks. Finally, Figure 3-8C shows the effect of Ti deposition on NAB. In this case, comparison of the spectrum after removal the Ti overlayer to that before deposition of Ti shows that the peak associated with the nitro group is dramatically affected. The $N_{405.9}$/C ratio decreases from 0.068 to 0.002, indicating nearly complete loss of the nitro group. In addition, the $N_{400.2}$/C ratio diminished by more than 75%. Although a Ti-N bond appearing at 397 eV has been reported after deposition of Ti onto PPF/NAB sample*[43]*, in the current case, the HF etch removed all titanium from the surface (no Ti XPS peaks were observed). As discussed above, Raman spectra were also obtained after removal of top contact metals as shown in Figure 3-7 to ensure optical artefacts with the metal overlayer present do not affect the spectra. It is striking to note that the molecular signature of NAB is absent from the surface after etching Ti, consistent with XPS data indicating the near total loss of the NAB structure. Combining the Raman and XPS results on the etched surfaces, we conclude that direct e-beam deposition of Cu and Au do not cause destruction of the NAB film, while Pt and Ti deposition cause substantial structural changes. In the case of Ti, it is likely that the reactivity of the Ti metal during evaporation results in damage through titanium carbide (and possibly other) bond formation. When the Ti metal is etched, the molecule is removed from the surface along with any Ti metal. For the case of Pt metal, it is likely that the heat released during condensation of the metal on the molecular layer results in local heating that is sufficient to disrupt some of the chemical bonds present, but does not entirely remove the layer from the surface.

3.3.4 Evaluation of Sample Morphology

Although Au and Cu caused minimal changes in Raman and XPS spectra of the NAB layer, it is possible that their deposition causes morphological changes. We investigated the film morphology with AFM after etching of Cu and Au. PPF/NAB surfaces before metal deposition were smooth, with no visual variations across a several μm^2 area (5 x 5 μm^2) and an rms roughness value similar to underivatized PPF ~0.46 nm over an area of 5 x 5 μm^2, shown in Figure 3-9.

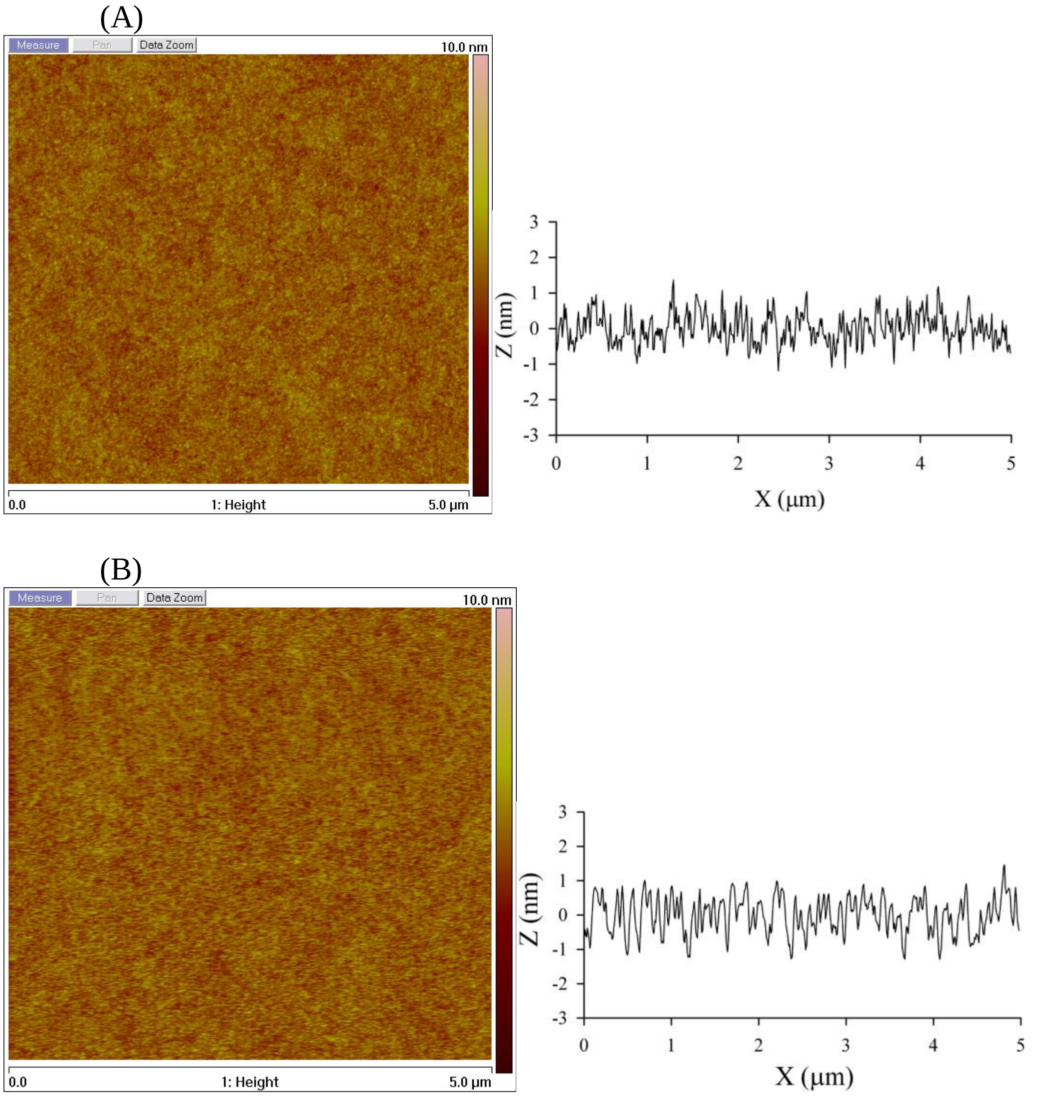

Figure 3-9. 5 μm x 5 μm Tapping mode AFM images of **(A)** PPF (rms ~ 0.44 nm) and **(B)** PPF/NAB (rms ~ 0.46 nm).

Figure 3-10 shows AFM images of PPF/NAB after deposition and etching of 45 nm of Cu or Au, using the same parameters as those for junction preparation. Figure 3-10A shows that deposition and removal of Cu metal had minor effects on the appearance of the AFM image over 5 x 5 μm^2 area, and an insignificant change in surface roughness to 0.47 ± 0.03 nm. However, after deposition and etching of Au, the rms roughness of the molecular layer over 5 x 5 μm^2 area was more than doubled to 1.12 ± 0.37 nm, and the AFM image was noticeably different (Figure 3-10B).

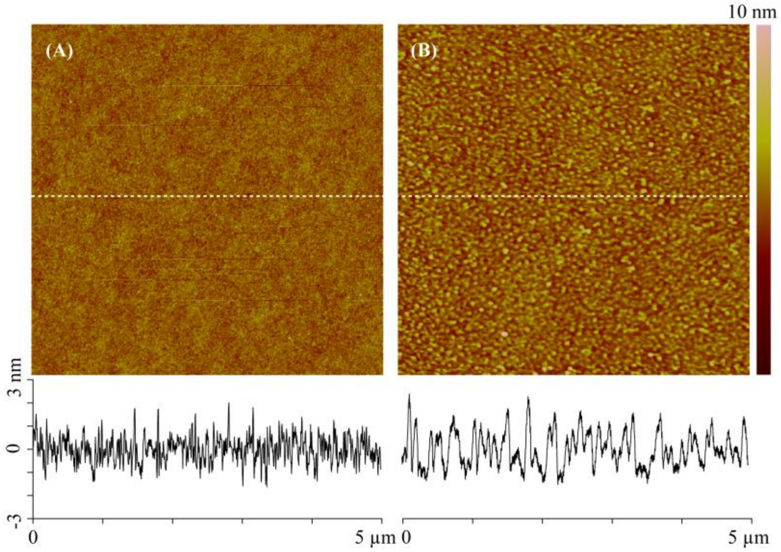

Figure 3-10. AFM scan over 5 x 5 μm^2 area of PPF/NAB surface with corresponding line scans after etching the top metal; (A) top metal was Cu while (B) top metal was Au. Roughness (rms) for Cu case: 0.47 nm, and for Au: 1.12 nm.

A control experiment in which an uncoated PPF/NAB sample was subjected to the etchant used to remove Au showed no changes in roughness or morphology over 5 x 5 μm^2 area as shown in Figure 3-11. Together with the higher currents observed for PPF/NAB/Au junctions compared to PPF/NAB/Cu devices, the AFM results in Figure 3-10 imply that Au partially penetrates the NAB molecular layer while Cu does not.

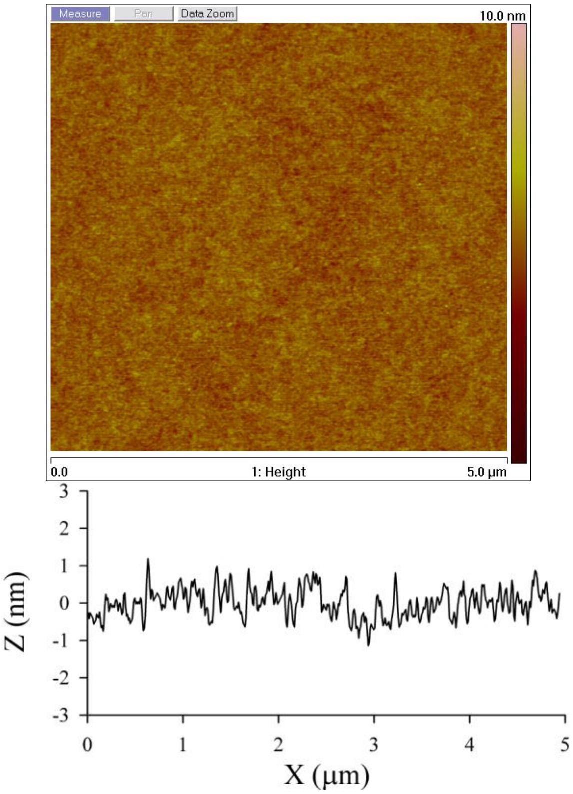

Figure 3-11. Tapping mode AFM scan of Si/SiO$_2$/PPF/NAB after immersion in Au etchant (KI/I$_2$) for 60 seconds, the scanned area is 5 μm x 5μm and rms ~ 0.37 nm.

Since both Raman and XPS results indicate that Au does not cause structural damage to the NAB film observable by these techniques, these results imply that Au penetrates the molecular layer during deposition without widespread damage to the molecular structure. The surface energy for Cu is higher than that of Au*[52]*, and we have reported previously that there is evidence from Raman and XPS that Cu interacts with the nitro group of NAB, while Au does not*[53]*. It is possible that the lower enthalpy of interaction of Au with aromatic molecules is insufficient to compensate the entropy increase associated with partial penetration of Au into the molecular layer. Thus, Cu appears to be the best choice for direct deposition of a top contact metal that will not disrupt the molecular layer, nor penetrate significantly into the molecular layer.

3.3.5 Thermal Stability of finished molecular junctions

In order to determine the temperature window that a completed PPF/NAB/Cu device can withstand, we have temperature-treated junctions in a vacuum environment. It should be noted that previous report demonstrates that PPF/NAB/Cu junctions are functional over wide temperature range (5 to 300 K) with no observable changes in *J-V* behaviour*[24]*. Figure 3-12 shows a series of *J-V* curves obtained after heat treatments of complete PPF/NAB/Cu devices. In each case, the sample was heated to the stated temperature for 5 minutes in vacuum, and then removed from the chamber and cooled to room temperature before testing. While there are no significant changes up to 190 ^{o}C, the conductance begins to increase at higher temperatures. After heating at 400 ^{o}C, the junction is ~33 times more conductive at 0.2 V. We reported recently that microfabricated carbon/NAB/Cu/Au junctions exhibited an irreversible slow conductance increase of 50% during 20 hours at 150 ^{o}C in vacuum, and were then stable for at least another 24 hours at 150 ^{o}C*[32]*.

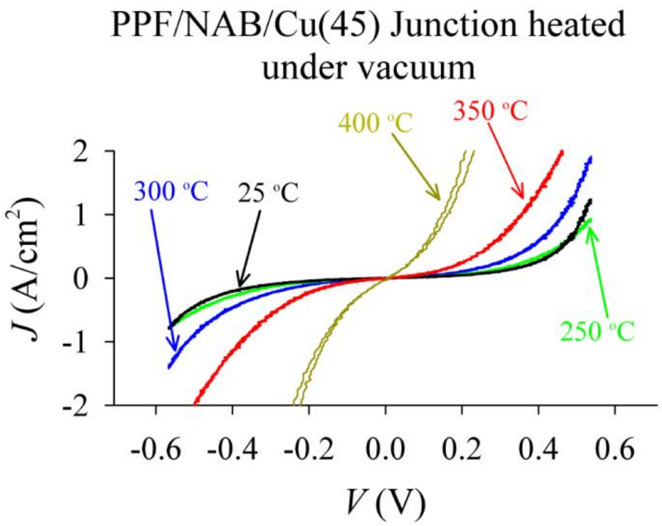

Figure 3-12. *J-V* curves of a single Si/SiO_2/PPF/NAB/Cu(45) junction heated in vacuum (~ 2 x 10^{-6} torr) to progressively higher temperature for 5 minutes at each temperature. Samples were cooled in air before obtaining each *J-V* curve.

Since a PPF/NAB sample without a top contact was shown to survive temperatures of 400 ^{o}C in the same vacuum environment (Figure 3-4), there are several possible explanations for the increase in junction conductance after thermal treatments in the 200-400 ^{o}C range. First, annealing of the Cu top contact could reorder the Cu atoms, leading to an increase of the effective contact area of the junction*[11]*. Second, a chemical reaction between the Cu and the NAB at elevated temperature could also alter junction conductance. Finally, although the molecular layer is expected to remain intact (see Figure 3-4), penetration of Cu atoms due to their increased mobility at higher temperature is possible. In any case, it is clear that completed devices can survive temperature excursions to ~200 ^{o}C without large conductance changes, and that the molecular layer is stable beyond 400 ^{o}C. This level of temperature stability is significantly beyond that of all known molecular junctions demonstrated to date.

3.3.6 Compatibility with Photolithography

Conventional photolithographic processing can involve harsh chemical treatments and significant UV radiation. Although this process is compatible with inorganic materials, the integration of "soft" organic molecules with lithographic processes is more challenging since many materials can undergo photo-degradation during the UV exposure*[54-56],* chemical reactions with resist components, and possible removal by solvents and developers. Recently we showed that a diazonium-derived molecular layer on titanium withstands sonication in acetone and acetonitrile, as well as 60 minutes in boiling water or 30 minutes in 0.1 M aqueous acid or base*[47].* In the current work, PPF/NAB samples were exposed to the photolithographic process of resist application/UV exposure/developing described in "experimental". Figure 3-13 shows Raman spectra for Si/SiO_2/PPF/NAB before and after a complete photolithographic process. The absence of changes in the spectrum for NAB indicates that this molecule is compatible with the photolithographic reagents and processing.

In addition, diazonium-derived trifluoromethylphenyl (TFMP) on PPF was also tested using XPS as a diagnostic and no change in the F/C ratio was observed after the photolithography process as shown in Figure 3-14.

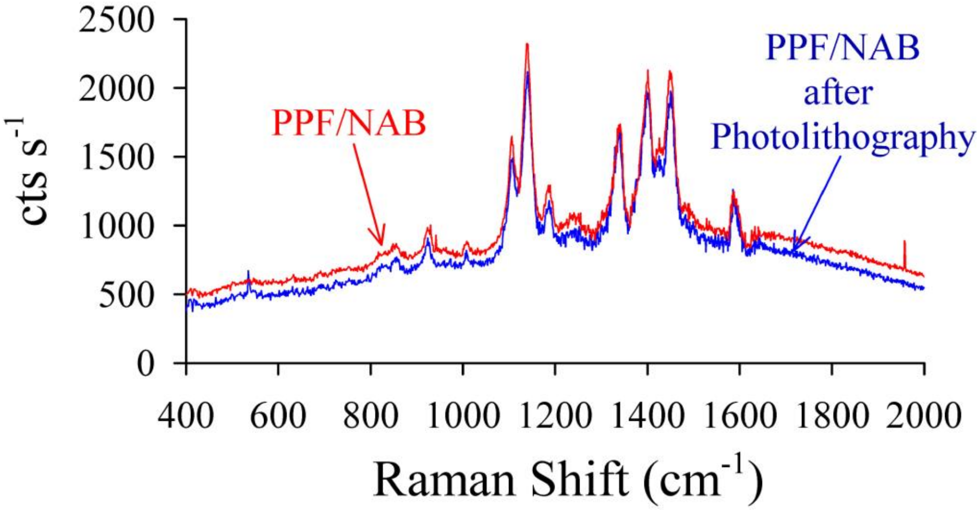

Figure 3-13. Raman Spectra of Si/SiO$_2$/PPF/NAB before (blue curve) and after (red curve) a complete photolithographic process (spin photoresist, UV exposure and development).

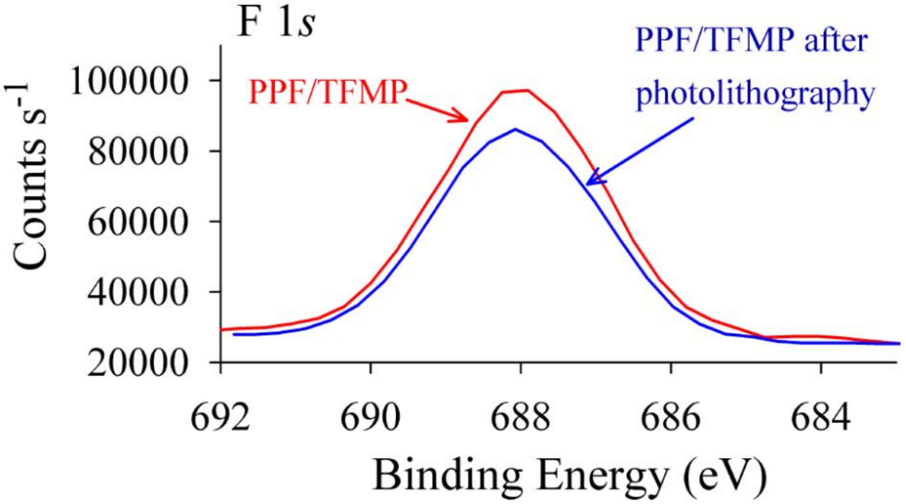

Figure 3-14. High-resolution XPS spectra of F*1s* region of Si/SiO$_2$/PPF/TFMP-4 as before (red curve), and after (blue curve) complete photolithographic process, F/C ratio initially = 0.0865 and after photolithography = 0.0862.

3.3.7 Sealing with parylene

Pyrolysis of the precursor di-p-xylylene at 600 °C under vacuum leads to dimer decomposition and production of gas-phase *p*-xylylene monomers. The *p*-xylylene monomers subsequently polymerize to parylene N (poly (*p*-xylylene)) on the sample surface, to produce a transparent hydrophobic film. The chamber maintains a sample temperature of ~ 30 °C*[57]*. As such, parylene N has been used as protective layer for microelectronics applications due to its low gas and water permeability, high melting point*[58]*, and hydrophobicity. In addition, it has good optical transparency*[58]* and a low dielectric constant*[59]*. Figure 3-15A shows *J-V* curves of a PPF/NAB(4.5)/Cu junction initially and after deposition of 0.3 μm parylene N. No significant changes in electronic behaviour occurred during parylene deposition, as expected, since the molecular junction is protected by the Cu top contact and the conditions during deposition are quite mild.

The effectiveness of parylene N as a barrier against moisture and chemical agents was investigated. The *J-V* curves shown in Figure 3-15B were obtained before and after immersion of a parylene-N coated PPF/NAB/Cu junction in 0.5 M $FeCl_3$ in water. Without the parylene coating, the $FeCl_3$ solution completely removed the Cu contact within 10 seconds, as described in section 3.3.3 above. As shown in Figure 3-15B, a 10 minute immersion in $FeCl_3$ had no effect on the electronic response of the parylene coated junction.

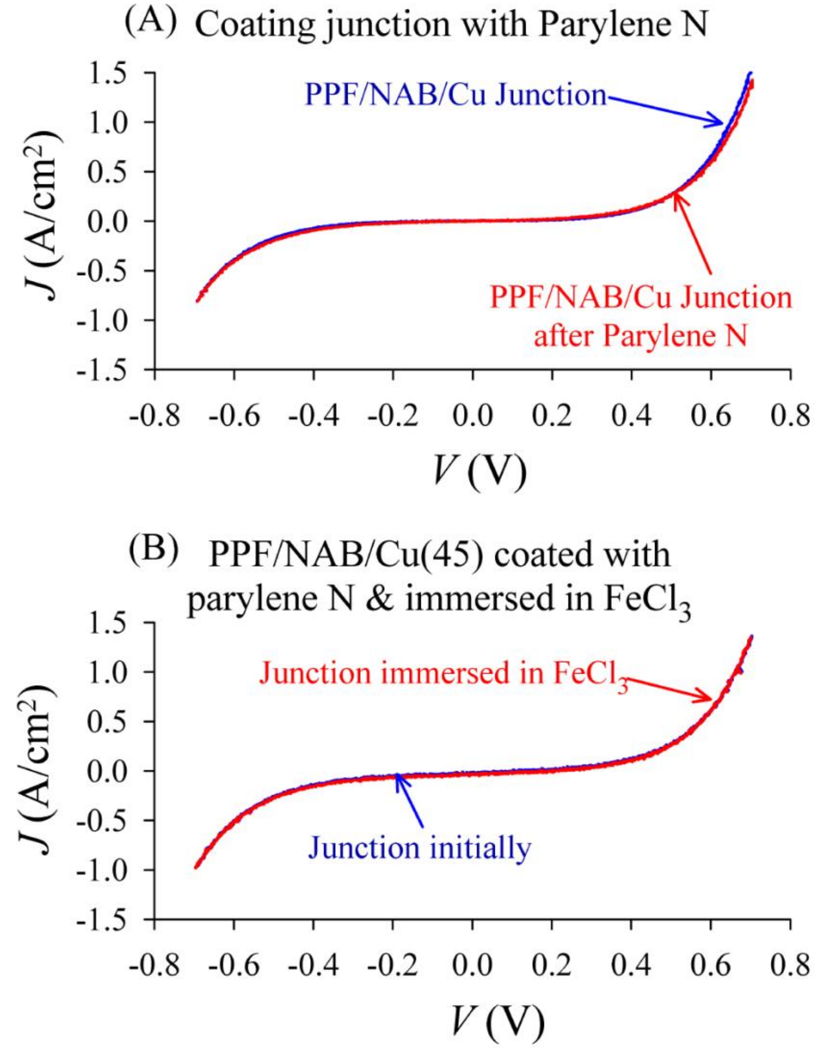

Figure 3-15. (A) Electrical characterization of Si/SiO_2/PPF/NAB/Cu junction before and after encapsulation with 0.3 μm parylene N. (B) *J-V* characteristic of parylene N coated Si/SiO_2/PPF/NAB-4/Cu junction and after immersion in 0.5 M $FeCl_3$ solution for 10 minutes.

The sample could also be immersed in water for 10 minutes as shown in Figure 3-16 behaving normally without any change in electrical properties. These results indicate that parylene-N forms an excellent barrier to water and aqueous reagents, and that the molecular junctions are unaffected by parylene deposition.

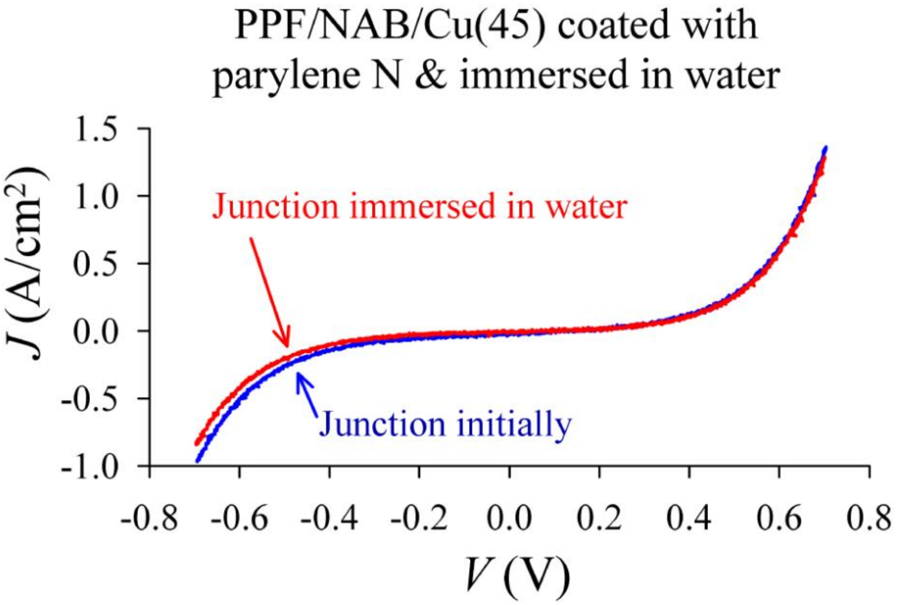

Figure 3-16. *J*-*V* curve of Si/SiO2/PPF/NAB/Cu(45) junction encapsulated with 0.3 μm parylene N and immersed in water for 10 minutes.

3.4 Summary

Taken together, the results herein establish several acceptable processing parameters for molecular electronic devices based on diazonium-modified carbon substrates. The strong carbon-carbon surface bond permits heating to at least 400 ^{o}C in vacuum without breaking the surface-molecule covalent bond, or detectable perturbation of the molecular structure. In addition, irreversible bonding permits direct e-beam deposition of Cu and Au on diazonium-derived molecular layers without observable damage to the molecular structure, nor the formation of carbon/metal short circuits. Metal penetration has been a significant problem with Langmuir-Blodgett and Au/thiol monolayers, with direct vapor deposition often resulting in short circuits*[4, 18, 20, 22, 60, 61]*. Although these approaches benefit from ordering of molecules into a 2-dimensional crystal, that ordering requires a labile molecule/surface bond in order to equilibrate to a low energy ordered state*[3]*. Diazonium modification of carbon sacrifices some ordering to ensure irreversible bonding to the surface*[3]* and its associated thermal and chemical stability. Unlike Au and Cu, direct Ti and Pt deposition cause significant changes to the molecular layer, due to the reactivity of Ti and the high heat of condensation of Pt. The reproducibility of carbon/NAB/Cu devices was significantly better than carbon/NAB/Au, and the cause was revealed by AFM of the molecular layers after removing the metal by chemical etching. Cu had no observable effect on the surface of the molecular layer, while Au caused a significant increase in roughness, presumably caused by partial Au penetration into the film.

No observable changes in NAB layers derived from diazonium reduction on carbon were observed by XPS or Raman spectroscopy following exposure to $FeCl_3$, I_2/KI, or HF solutions in water, or from temperature excursions to 400 ^oC in vacuum. Finished devices could be heated to 250 ^oC without major changes in electronic properties, and sealing with parylene protected the devices from at least 10 minutes of exposure to water or $FeCl_3$ solution. PPF/NAB can be subjected to a complete resist/exposure/develop photolithography cycle with no apparent changes to the Raman spectrum, implying structural integrity throughout the process.

While there are many more requirements which much be met for integration of molecular devices with conventional microelectronics, the current work extends the temperature range and acceptable processing steps significantly. We demonstrated recently that the diazonium route to molecular junctions is compatible with microfabrication techniques, with high yield and good reproducibility*[32]*.

3.5 Endnotes

A version of chapter III has been published. Amr M. Mahmoud, Adam J. Bergren, Nikola Pekas, Richard L. McCreery, *Advanced Functional Materials* **2011**, 21(12), 2273-2281.

3.6 References

[1] H. B. Akkerman, B. De Boer, *Journal of Physics: Condensed Matter* 2008, *20*, 013001.

[2] R. L. McCreery, *Analytical Chemistry* 2006, *78*, 3490.

[3] R. L. McCreery, A. J. Bergren, *Advanced Materials* 2009, *21*, 4303.

[4] H. Haick, D. Cahen, *Progress in Surface Science* 2008, *83*, 217.

[5] A. Salomon, T. Boecking, O. Seitz, T. Markus, F. Amy, C. Chan, W. Zhao, D. Cahen, A. Kahn, *Advanced Materials* 2007, *19*, 445.

[6] A. Salomon, D. Cahen, S. Lindsay, J. Tomfohr, V. B. Engelkes, C. D. Frisbie, *Advanced Materials* 2003, *15*, 1881.

[7] B. Ulgut, H. D. Abruna, *Chem. Rev.* 2008, *108*, 2721.

[8] R. E. Holmlin, R. Haag, M. L. Chabinyc, R. F. Ismagilov, A. E. Cohen, A. Terfort, M. A. Rampi, G. M. Whitesides, *Journal of the American Chemical Society* 2001, *123*, 5075.

[9] F. Chen, J. Hihath, Z. F. Huang, X. L. Li, N. J. Tao, *Annual Review of Physical Chemistry* 2007, *58*, 535.

[10] P. A. Van Hal, E. C. P. Smits, T. C. T. Geuns, H. B. Akkerman, B. C. De Brito, S. Perissinotto, G. Lanzani, A. J. Kronemeijer, V. Geskin, J. Cornil, P. W. M. Blom, B. De Boer, D. M. De Leeuw, *Nature Nanotechnology* 2008, *3*, 749.

[11] A. J. Bergren, K. D. Harris, F. J. Deng, R. L. McCreery, *Journal of Physics-Condensed Matter* 2008, *20*, 374117.

[12] L. Luo, C. D. Frisbie, *Journal of the American Chemical Society* 2010, *132*, 8854.

[13] E. A. Weiss, R. C. Chiechi, G. K. Kaufman, J. K. Kriebel, Z. F. Li, M. Duati, M. A. Rampi, G. M. Whitesides, *Journal of the American Chemical Society* 2007, *129*, 4336.

[14] F. Anariba, R. L. McCreery, *Journal of Physical Chemistry B* 2002, *106*, 10355.

[15] C. Grave, E. Tran, P. Samori, G. M. Whitesides, M. A. Rampi, *Synthetic Metals* 2004, *147*, 11.

[16] H. B. Akkerman, A. J. Kronemeijer, J. Harkema, P. A. van Hal, E. C. P. Smits, D. M. de Leeuw, P. W. M. Blom, *Organic Electronics* 2010, *11*, 146.

[17] M. Coll, C. A. Richter, C. A. Hacker, *Journal of Vacuum Science & Technology B* 2009, *27*, 2826.

[18] H. Haick, D. Cahen, *Accounts of Chemical Research* 2008, *41*, 359.

[19] Z. Zhu, D. L. Allara, N. Winograd, *Applied Surface Science* 2006, *252*, 6686.

[20] A. V. Walker, T. B. Tighe, O. M. Cabarcos, M. D. Reinard, B. C. Haynie, S. Uppili, N. Winograd, D. L. Allara, *Journal of the American Chemical Society* 2004, *126*, 3954.

[21] B. C. Haynie, A. V. Walker, T. B. Tighe, D. L. Allara, N. Winograd, *Applied Surface Science* 2003, *203*, 433.

[22] G. L. Fisher, A. V. Walker, A. E. Hooper, T. B. Tighe, K. B. Bahnck, H. T. Skriba, M. D. Reinard, B. C. Haynie, R. L. Opila, N. Winograd, D. L. Allara, *Journal of the American Chemical Society* 2002, *124*, 5528.

[23] F. Anariba, J. K. Steach, R. L. McCreery, *Journal of Physical Chemistry B* 2005, *109*, 11163.

[24] A. J. Bergren, R. L. McCreery, S. R. Stoyanov, S. Gusarov, A. Kovalenko, *Journal of Physical Chemistry C* 2010, *114*, 15806.

[25] R. McCreery, *Chemistry of Materials* 2004, *16*, 4477.

[26] R. L. McCreery, *ChemPhysChem* 2009, *10*, 2387.

[27] W. R. McGovern, F. Anariba, R. L. McCreery, *J. Electrochem. Soc.* 2005, *152*, E176.

[28] F. Anariba, S. H. DuVall, R. L. McCreery, *Analytical Chemistry* 2003, *75*, 3837.

[29] J. K. Kariuki, M. T. McDermott, *Langmuir* 1999, *15*, 6534.

[30] J. K. Kariuki, M. T. McDermott, *Langmuir* 2001, *17*, 5947.

[31] R. L. McCreery, U. Viswanathan, R. P. Kalakodimi, A. M. Nowak, *Faraday Discussions* 2006, *131*, 33.

[32] J. Ru, B. Szeto, A. Bonifas, R. L. McCreery, *ACS Applied Materials & Interfaces* 2010, *in press*.

[33] H. H. Yang, R. L. McCreery, *Journal of the Electrochemical Society* 2000, *147*, 3420.

[34] S. H. DuVall, R. L. McCreery, *Journal of the American Chemical Society* 2000, *122*, 6759.

[35] P. Allongue, M. Delamar, B. Desbat, O. Fagebaume, R. Hitmi, J. Pinson, J. M. Saveant, *Journal of the American Chemical Society* 1997, *119*, 201.

[36] S. Ranganathan, R. McCreery, S. M. Majji, M. Madou, *Journal of the Electrochemical Society* 2000, *147*, 277.

[37] S. Donner, H. W. Li, E. S. Yeung, M. D. Porter, *Analytical Chemistry* 2006, *78*, 2816.

[38] H. Tian, A. J. Bergren, R. L. McCreery, *Applied Spectroscopy* 2007, *61*, 1246.

[39] J. Ramsey, S. Ranganathan, R. L. McCreery, J. Zhao, *Applied Spectroscopy* 2001, *55*, 767.

[40] L. C. T. Shoute, A. J. Bergren, A. M. Mahmoud, K. D. Harris, R. McCreery, L., *Appl Spectrosc* 2009, *63*, 133.

[41] A. P. Bonifas, R. L. McCreery, *Nature Nanotechnology* 2010, *5*, 612.

[42] W. R. McGovern, F. Anariba, R. McCreery, *J. Electrochem Soc* 2005, *152*, E176.

[43] A. M. Nowak, R. L. McCreery, *Analytical Chemistry* 2004, *76*, 1089.

[44] A. M. Nowak, R. L. McCreery, *Journal of the American Chemical Society* 2004, *126*, 16621.

[45] E. DeIonno, H. R. Tseng, D. D. Harvey, J. F. Stoddart, J. R. Heath, *J. Phys. Chem. B* 2006, *110*, 7609.

[46] M. Toupin, D. Belanger, *Journal of Physical Chemistry C* 2007, *111*, 5394.

[47] A. M. Mahmoud, A. J. Bergren, R. L. McCreery, *Analytical Chemistry* 2009, *81*, 6972.

[48] H. H. Liang, H. Tian, R. L. McCreery, *Applied Spectroscopy* 2007, *61*, 613.

[49] T. Itoh, R. L. McCreery, *Journal of the American Chemical Society* 2002, *124*, 10894.

[50] P. S. Chen, *A new handbook of chemistry*, Chemical Elements Pub, Camarillo, Calif 1975.

[51] C. H. deVilleneuve, J. Pinson, M. C. Bernard, P. Allongue, *Journal of Physical Chemistry B* 1997, *101*, 2415.

[52] H. L. Skriver, N. M. Rosengaard, *Physical Review B* 1992, *46*, 7157.

[53] R. L. McCreery, J. Wu, R. P. Kalakodimi, *Physical Chemistry Chemical Physics* 2006, *8*, 2572.

[54] J. Ficker, H. von Seggern, H. Rost, W. Fix, W. Clemens, I. McCulloch, *Applied Physics Letters* 2004, *85*, 1377.

[55] M. Manceau, J. Gaume, A. Rivaton, J. L. Gardette, G. Monier, L. Bideux, *Thin Solid Films* 2010, *518*, 7113.

[56] T. Caronna, M. Forte, M. Catellani, S. V. Meille, *Chemistry of Materials* 1997, *9*, 991.

[57] P. Kramer, A. K. Sharma, E. E. Hennecke, H. Yasuda, *Journal of Polymer Science Part a-Polymer Chemistry* 1984, *22*, 475.

[58] Y. S. Yeh, W. J. James, H. Yasuda, *Journal of Polymer Science Part B-Polymer Physics* 1990, *28*, 545.

[59] J. J. Senkevich, S. B. Desu, *Applied Physics Letters* 1998, *72*, 258.

[60] R. M. Metzger, *Acc. Chem. Res.* 1999, *32*, 950.

[61] R. M. Metzger, T. Xu, I. R. Peterson, *J. Phys. Chem. B* 2001, *105*, 7280.

Chapter 4

Charge Transfer within Molecular Electronic Junctions based on Si(111) / Aromatic Molecular Layer and Cu Top Contact

4.1 Introduction

One target of studying molecular electronics junctions is the incorporation of organic molecules into electronics devices between two electrodes, this incorporation allows exploitation of organic molecules' intrinsic properties to tune charge transfer within molecular electronics devices. Understanding the mechanism of charge transfer is a crucial step for rational design and fabrication of molecular electronic devices with pre-determined electrical characteristics. There are various experimental methods to study how molecular layer structure affects charge transfer through molecular electronic junctions, such as systematic variation of molecular layer thickness by multilayer formation or using homologous series of organic molecules *[1-6]*. Another method is changing the molecular layer while the contacts remain constant*[1]* or changing the bond between the contacts and molecular layer*[3, 7-12]*. In addition, effect of contact electrode was studied by changing the top contacts of the molecular junction keeping the same molecular layer*[3, 13, 14]*.

As described in previous chapters, PPF/molecule/Cu molecular junctions permit evaluation of the electronic behavior of various molecules acting as active components in an electronic circuit. The Cu top contact produces junctions that are reproducible*[1, 15, 16]*, thermally stable*[13, 17]*, scalable*[18]* and the yield is high*[1, 16, 18]* and without evidence of damage to the organic molecular layer*[17]*. Quantum tunneling is the proposed charge transfer mechanism within PPF/molecule/Cu junctions and the tunneling barrier height is the energy difference between the contact Fermi level and the highest occupied molecular orbital HOMO of the molecular layer*[15, 19]*. To gain more information about charge transfer, PPF/molecular layer junctions were fabricated using different top contacts. Carbon*[13]*, amorphous Si deposited by electron beam evaporator*[14]*, Au and Pt deposited by a diffusion mediated method*[20]* were used as top contacts to fabricate the junctions and compared to PPF/molecular layer/Cu junctions.

In this chapter, molecular junctions with the PPF electrode replaced by Si are described. Molecular electronic devices based on a Si substrate were fabricated in order to study the effect of substrate composition on conduction through the molecular layer. Both n- and p- type Si samples were used as substrates in order to evaluate the effect of majority charge carriers (electrons or holes) on transport. Furthermore, the Fermi energy of the Si substrate can be manipulated by controlling the doping level, presumably without disturbing the Si/molecule interface.

Silicon has been used previously as a substrate electrode for fabrication and study of molecular electronic junctions. The Si(100) and Si(111) surfaces are commonly used to fabricate molecular junctions*[7, 21]*, since they are readily prepared from bulk silicon. Upon wet etching of the native silicon oxide, Si(111) produces atomically flat surface while Si(100) produces a rougher surface. Furthermore, modified Si(111) surfaces have a more dense molecular layer and higher coverage than modified Si(100)*[22-24]*. There are various chemical methods to modify the silicon surface to form stable Si-C bond. For example, molecular electronic junctions based on Si modified by aromatic molecular layer*[25-31]* and modified by alkane and alkene molecular layers have been fabricated. In addition, molecular electronic junctions with Si- thiol*[32]* or Si-O-C bond were investigated*[7, 33]*.

The doping level of Si is expected to be a crucial factor that contributes to the junction's electrical behavior*[34]*. For moderately doped Si substrate, the semiconductor characteristics predominate and the junction behaves as a Schottky diode, with the molecular layers having negligible effect on modulating the Schottky barrier*[35, 36]*. For heavily doped Si, molecular layer characteristics should dominate the junction behavior and changes in the molecule thickness affect conduction*[30]*. In the current research, heavily doped Si substrates were used to minimize the semiconductor properties of the substrate. Of particular interest is the comparison of Si-based molecular junctions to those made with carbon (PPF), and how the majority carrier in the Si affects electronic behavior.

4.2 Experimental Section

4.2.1 Materials and reagents

Acetonitrile, acetone and isopropanol (HPLC grade, Fischer Scientific), buffer oxide etch (BOE) (40% NH_4F/49% HF 10:1, CMOS grade J. T. Baker), 40% NH_4F and tetrabutylammonium hexafluorophosphate (TBAHFP, from Sigma-Aldrich) were used as received. . Heavily doped *p*-Si (B doped, orientation 111) and *n*-Si (As doped, orientation 111) wafers both have a resistivity of ~ 0.001-0.005 Ω.cm (purchased from El-Cat inc.), nitroazobenzene diazonium salt (NAB DS) was prepared as described previously*[37-39]*.

4.2.2 Junction Fabrication and Surface Characterization

4.2.2.1 Sample Cleaning and Au Contact Pad Deposition

Scheme 4.1 summarizes the fabrication steps of the Si/Molecular layer/Cu/Au junctions. First, the Si(111) sample wafers were cleaned with piranha solution (3:1 H_2SO_4/H_2O_2) for 15 minutes. Then, 250-300 nm of oxide layer was grown thermally to avoid residual polishing damage as discussed previously*[40, 41]*. In addition, it has been reported that the structure of the H-terminated Si depends strongly on the nature of the initial silicon/oxide interfacial layer, where thermal oxides lead to flatter surfaces*[42]*. The smoothness of H-terminated Si surface was found to greatly affect molecular junctions' reproducibility, as described below. Moreover, the thermal oxide serves as the insulator between the Si bottom electrode and Cu/Au top contact in regions outside the junction area.

The wafers were diced into pieces of 18 x 13 mm^2 after being coated with photoresist to protect Si surface from scratches. To make ohmic contact with Si surface, Au contact pads were deposited on H-terminated Si surface as follows: the samples were cleaned with piranha solution for 15 minutes and then contact pad area (500 x 500 μm^2) was defined by conventional photolithography. A positive photoresist AZ P4330-RS was spin-coated on the samples at a speed of 500 rpm for 10 seconds followed by 6000 rpm for 60 s, and soft baked on a hotplate at 110 °C for 180 seconds in air. A Quintel Q-4000 mask aligner was used to expose the photoresist to UV radiation using pressure contact mode. After that, samples were exposed to UV for 10 seconds, the photoresist was developed in a mixture of AZ400K developer and deionized water (1:3 v/v). Finally, samples were rinsed with deionized water and dried with N_2. The samples were immersed in BOE (etch rate of thermal oxide was 50 nm/minute) until thermal oxide was etched. Then samples were transferred directly to a Johnsen Ultravac electron-beam evaporator where 50 nm of Au was deposited under vacuum (deposition rate 3 Å/s, vacuum pressure 2.4 x 10^{-7} torr). Finally, the samples were immersed in acetone, and then isopropanol 5 minutes each to lift off the photoresist and samples cleaned were with piranha and rinsed copiously with de-ionized water.

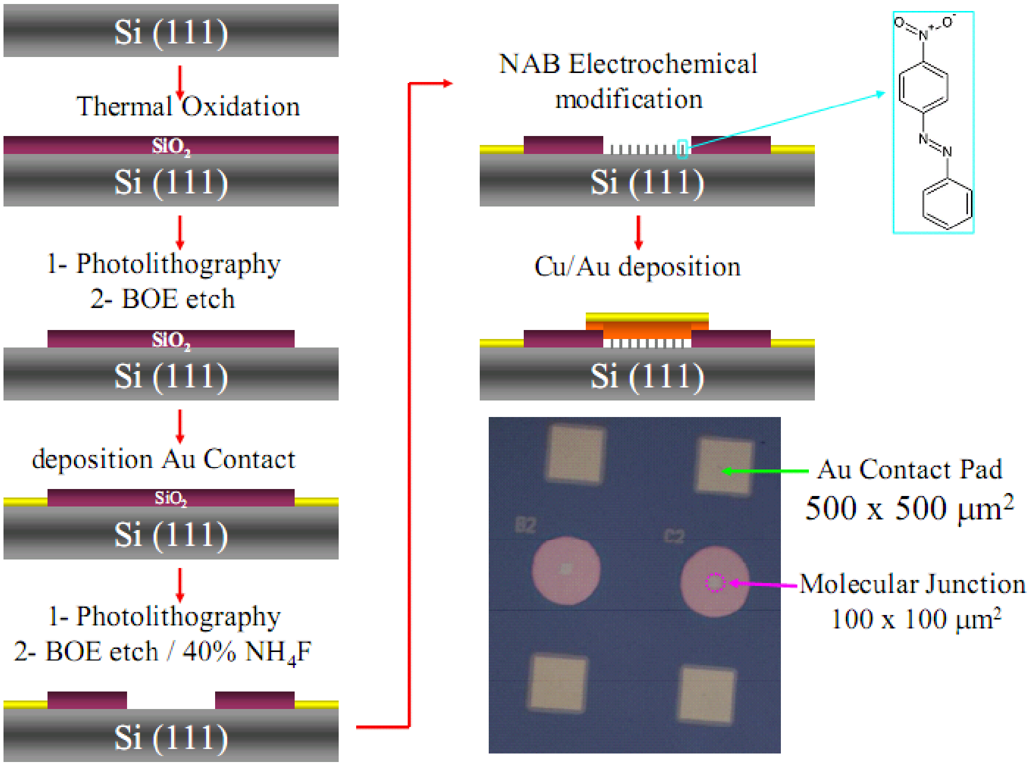

Scheme 4.1. Fabrication steps of Si(111)/molecular layer/Cu/Au junctions and the bottom right is an optical image (magnified x10) of the finished device (not drawn to scale).

4.2.2.2 Flat H-terminated Si Surface Preparation and Electrochemical Modification

The Junction area (100 x 100 μm^2) was defined by another photolithographic process following steps described above. The thermally grown silicon oxide was stripped by BOE, then atomically smooth H-terminated Si was obtained by immersion of the samples for 6 minutes in 40% NH_4F[40] (previously degassed with Ar for 30 min). Then samples were cleaned with acetone, IPA and de-ionized water to remove the photoresist. Covalent modification of freshly prepared hydrogen-terminated Si samples was performed using cyclic voltammetry in 3 electrode configuration. The working electrode was an H-terminated Si sample that was contacted by the Au pads. The reference electrode was Ag/Ag^+ in acetonitrile, and a Pt wire was the counter electrode. Samples were immersed in acetonitrile solution of 1 mM of NAB diazonium salt and 0.1 M of TBAHFP as supporting electrolyte. Then a voltage sweep was applied (from 400 to -1000 m*V* vs. Ag/Ag^+) with four voltammetric cycles and scan rate was 200 m*V*/s. Cyclic voltammetry of *p*-Si(111)/NAB in NAB diazonium ion solution is shown in Figure 4.1. After voltammetry, the samples cleaned with acetonitrile and dried under N_2 stream.

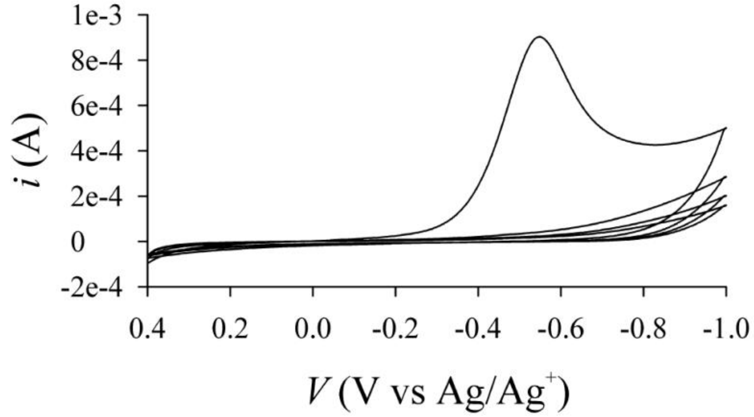

Figure 4.1. Cyclic voltammetry of H-terminated *p*-Si(111) modified in 1 mM NAB DS in acetonitrile solution and 0.1 M tetrabutylammonium hexafluorophosphate as supporting electrolyte, 4 cycles were done. Ag/Ag^+ in acetonitrile is used as reference electrode and Pt wire as counter electrode.

4.2.2.3 Top Metal Deposition and Junction Electrical Characterization

Freshly modified Si/NAB samples were transferred to an e-beam evaporator (Kurt J. Lesker, PVD75) and top metal contact deposition performed under vacuum pressure (2.2 x 10^{-6} torr) through a metal shadow mask. Top metal contacts were Cu 30 nm followed by Au 15 nm as measured by quartz crystal microbalance (QCM); deposition rate were 1 Å/s and 2 Å /s respectively.

Electrical characterization of Si/NAB/Cu/Au junctions was performed in ambient atmosphere and room temperature, using a three-wire configuration where the top metal contact was the virtual ground, with the drive voltage (V_{drive}) applied to Si through Au contact pad (thus, all voltages reported herein indicate the voltage of the Si relative to the top contact). The third probe was used to sense voltage on Si to compensate for ohmic loss (*iR* drop). Data collection was done using a National Instruments 6111 or 6120 DAQ board controlled by LabView software to execute voltage sweeps and record the resulting current after amplification by an SRS 570 current amplifier. The voltage sweep was 1000 *V*/Sec unless indicated otherwise. In addition, a Keithley 2602A sourcemeter in 2 wires configuration was used to measure the Au/Si(111)/Au contact pad resistance as shown in Figure 4.2. Si/Molecule/Cu junctions were compared to pyrolyzed photoresist film (PPF) molecular junctions' data published in the literature*[15]*.

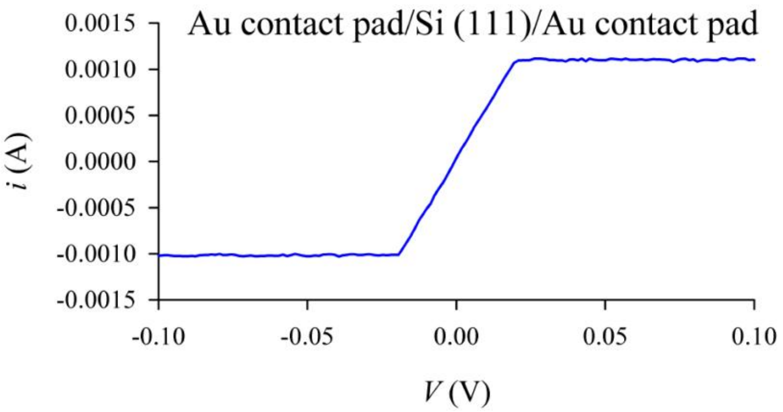

Figure 4.2. *i-V* curve of Au contact pad/Si(111)/Au contact pad measured in 2 wire configuration.

4.2.2.4 Surface Characterization

Samples for surface characterization were prepared as discussed above except that deposition of Au contact pad and photolithography steps were omitted. The morphology of H-terminated Si and modified Si surfaces was studied by tapping mode atomic force microscopy (AFM). The thickness of NAB molecular layer on Si substrate was determined by AFM scratching of the molecular layer by AFM tip in contact mode as described previously in detail*[43]*. Raman Spectroscopy was used to detect the NAB molecular layer covalently attached to the surface during electrochemical modification of Si samples. Raman spectra were collected using a custom built spectrometer equipped with an Argon ion laser (514.5 nm), and a back scattering geometry that employs an Andor back-thinned charge-coupled device (CCD) detector cooled to -80° C as described previously*[44]*. The incident power on the sample was ~19 mW and the signal was integrated for 240 seconds. H-terminated Si and modified Si Samples were characterized by X-ray photoelectron spectroscopy (XPS) to obtain information about elemental composition of the surface and electronic structure of the core energy levels. Ultra-violet photoelectron spectroscopy (UPS) was used to explore the electronic structure of H-terminated and modified Si samples. The samples for XPS and UPS were loaded in the analysis chamber within 15 minutes of preparation and transferred under vacuum to minimize any oxidation by atmosphere. For UPS measurements, a helium I (21.2 eV) light source was used to excite the electrons. During UPS analysis, -5 V bias was applied to the samples in order to enable collection of data near the secondary electron cutoff.

4.3 Results and Discussion

4.3.1 Surface Characterization

4.3.1.1 Atomic Force Microscopy

To confirm the preparation of flat H-terminated Si (111) surfaces, samples were scanned by AFM tapping mode. Figure 4.3 and 4.4 show AFM scans of the freshly prepared H-terminated Si surfaces of *p*- and *n*- Si(111) respectively. The root mean square (rms) roughness was 0.15 nm for *p*-Si(111) over a scan area 2 x 2 μm^2, while for *n*-Si(111) it was 0.1 nm over 5 x 5 μm^2 area. That roughness is comparable to the roughness for Si(111) reported in the literature (0.15 nm over 1 μm^2 area)*[7, 34]*. Figure 4.5 is an AFM scan of *n*-Si (111) modified with NAB prepared by 4 voltammetric cycles. The rms roughness was 0.3 nm, which is comparable to that observed for PPF/NAB surfaces (~0.46 nm)*[43]*.

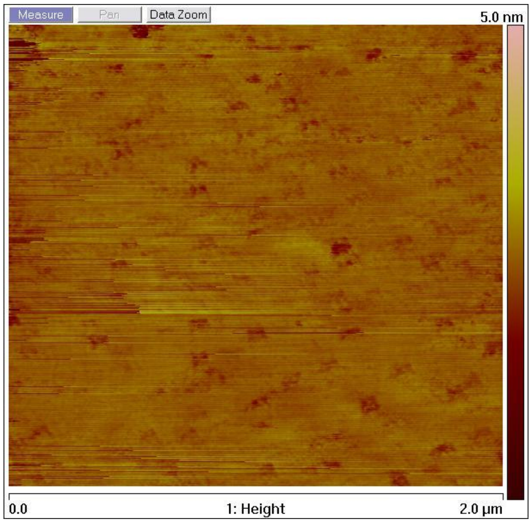

Figure 4.3. AFM scan of p-Si(111) surface 2 x 2 μm^2, rms = 0.15 nm

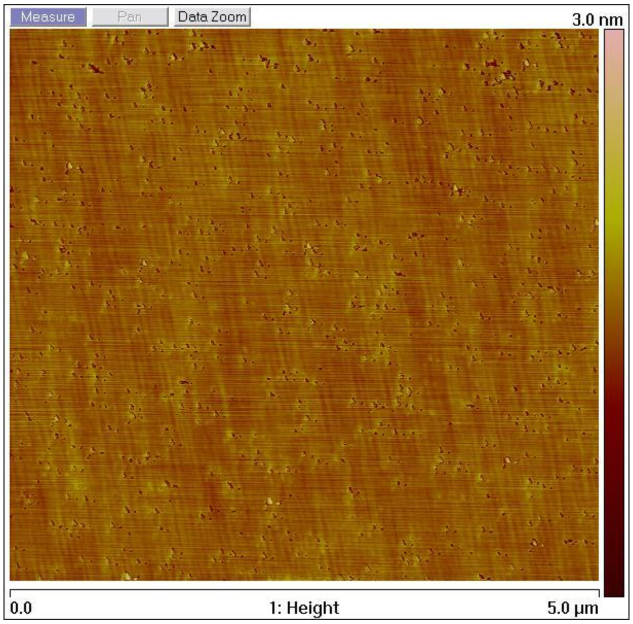

Figure 4.4. AFM scan of n-Si(111) surface 5 x 5 µm^2, rms = 0.1 nm

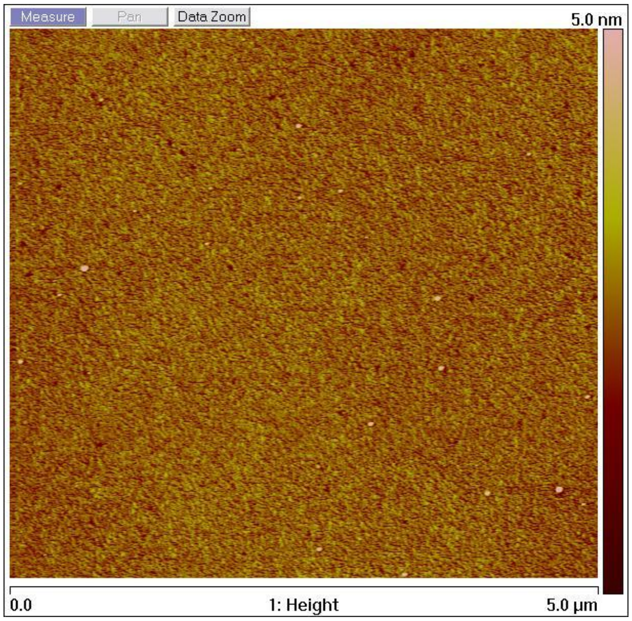

Figure 4.5. AFM scan of modified n-Si(111)/NAB-4 surface 5 x 5 µm^2, rms = 0.3 nm

The thickness of NAB molecular layer was determined by scratching techniques to be 5.6 ± 0.6 nm for *p*-Si(111)/NAB and 5.8 ± 0.5 nm for *n*-Si(111)/NAB as shown in Figures 4.6 and 4.7 respectively. It is worth noting that the silicon oxide layer thermally grown before etching Si(111) significantly improves the flatness of the Si surface, which in turn improves the reproducibility of the molecular electronic junctions.

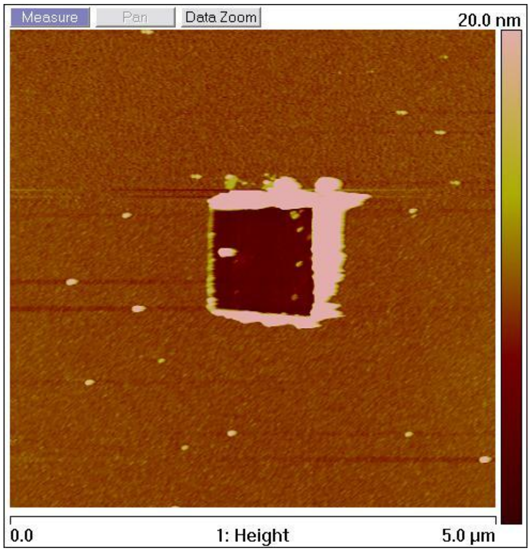

Figure 4.6. AFM scan of p-Si(111)/NAB-4 surface 5 x 5 µm^2, the molecular layer was scratched 1 x 1 µm^2, and thickness of molecular layer is 5.6 nm.

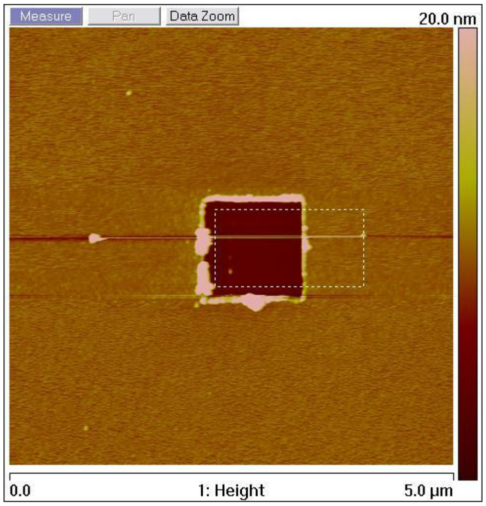

Figure 4.7. AFM scan of n-Si(111)/NAB-4 surface 5 x 5 µm^2, the molecular layer was scratched 1 x 1 µm^2, and thickness of molecular layer is 5.8 nm.

4.3.1.2 Raman Spectroscopy

Figure 4.8 shows the Raman spectra of both H-terminated *p*-Si and *p*-Si/NAB samples. It is obvious that there are no peaks on H-terminated Si above 1100 cm^{-1}, where the modified Si shows the characteristic Raman signals for NAB molecule on the surface. The peaks assignment for NAB Raman peaks are given in Table 4.1 and compared with the NAB molecule in CCl_4 from literature*[45, 46]*.

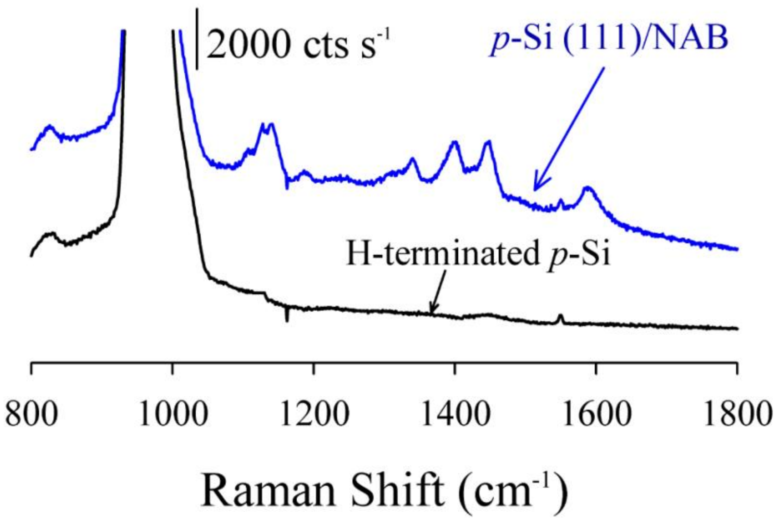

Figure 4.8. Raman spectra of both H-terminated p-Si(111) and p-Si/NAB(5.6), the data collection time was 240 seconds.

Raman Shift(cm^{-1}) NAB in CCl_4*	Raman Shift (cm^{-1}) p-Si(111)/ NAB	Peak Assignment
1147	1139	Ph-N=N stretch
1183	1186	CH bend
1347	1340	NO_2 sym stretch
1412	1408	N=N stretch
1449	1449	N=N stretch
1594	1589	C=C ring stretch

* Data from the literature see the text

Table 4.1. Characteristic Raman frequency and peak assignment for NAB molecular layer on p-Si(111) sample compared to NAB molecule in CCl_4.

4.3.1.3 X-ray photoelectron spectroscopy (XPS)

XPS survey spectra of *p*-Si(111) with native oxide cleaned with piranha solution, H-terminated *p*-Si(111) and *n*-Si(111) are shown in Figures 4.9, 4.10 and 4.11 respectively. All spectra have strong Si peaks, and adventitious carbon peak. For *p*-Si with native oxide, there is another strong peak for O(1*s*) of the silicon oxide layer near 532 eV. The oxygen peak on both H-terminated *p*- & *n*-Si samples are due to adsorbed oxygen on the surface not oxidation of silicon surface as discussed below. Figure 4.12 is a magnification of the Si region showing two strong sharp peaks, the first peak for Si_{2p} near 100 eV and the second peak near 150 eV for Si 2*s*. There are also two small broad peaks at 118 and 169 eV corresponding to Si_{2p} and Si_{2s} plasmon losses peaks respectively*[47]*.

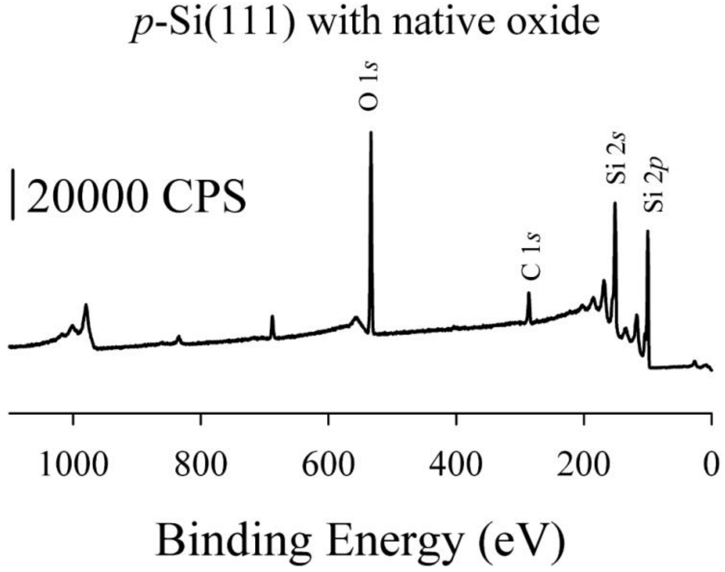

Figure 4.9. XPS survey spectrum analysis for p-Si(111) with native oxide sample.

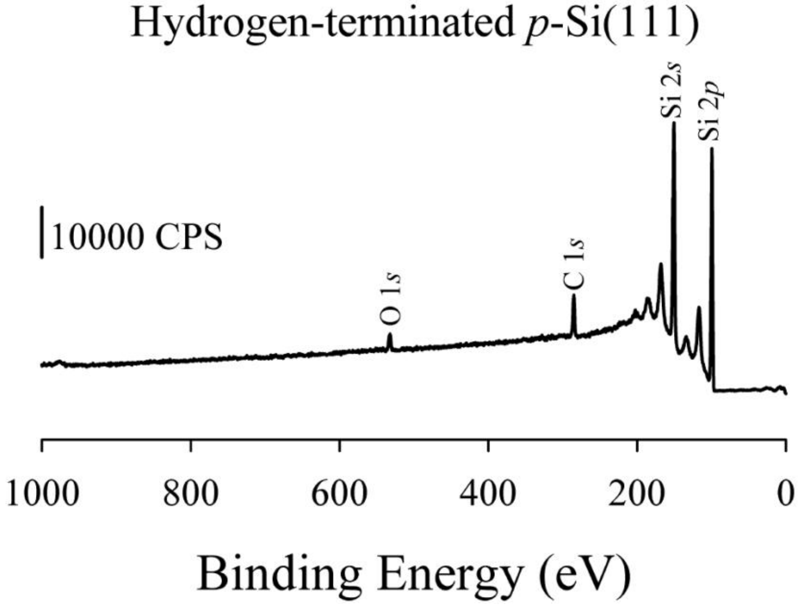

Figure 4.10. XPS survey spectrum analysis for H-terminated p-Si(111) sample.

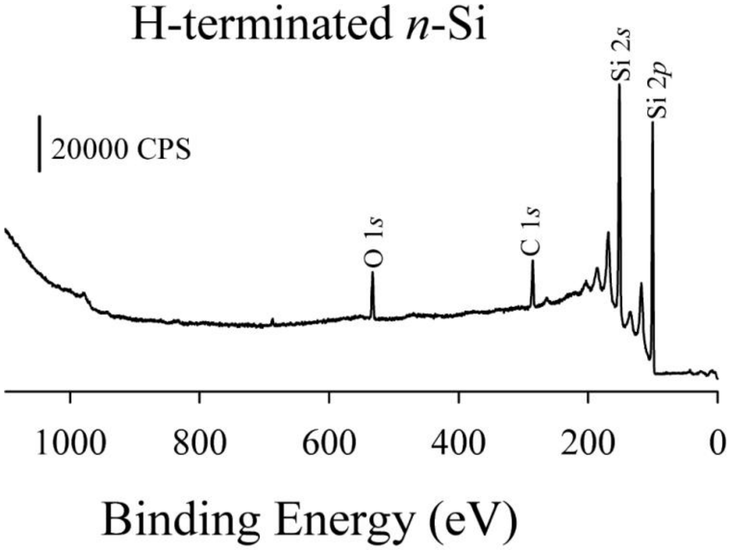

Figure 4.11. XPS survey spectrum analysis for H-terminated n-Si(111) sample.

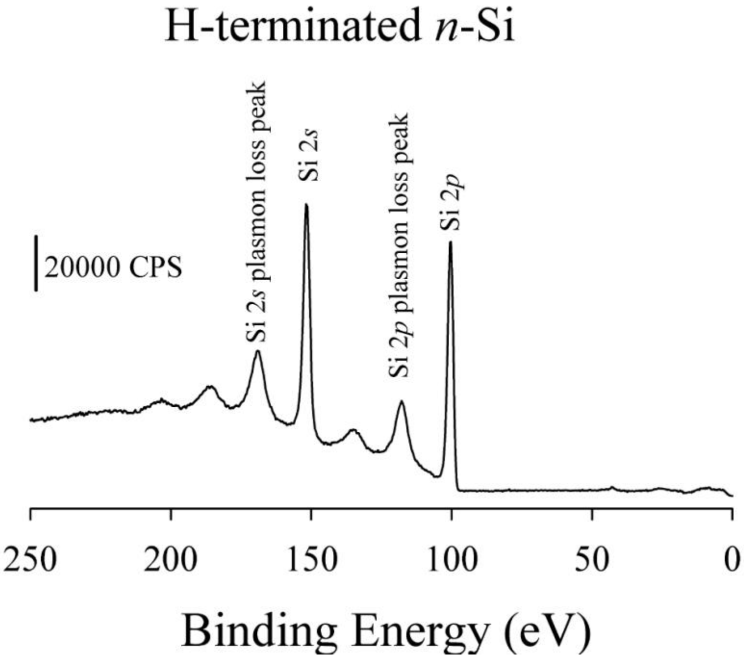

Figure 4.12. Magnification of XPS spectrum of H-terminated n-Si(111) sample in the silicon peak region.

High resolution analysis of Si_{2p} was performed in order to differentiate between the Si surface oxidation and adventitious O_2 on the surface during sample transfer; it also provides information about the electronic energy levels of Si surface. In the case of ideally H-terminated Si, the Si 2*p* peak shows only the doublet due to $\mathrm{Si}_{2p\ 3/2}$ and Si $2p_{1/2}$. As the samples start to oxidize, a peak for Si-O bond appears near 104 eV, and this peak has been reported to quantify the thickness of silicon oxide layer on Si surface *[28]*. The deconvoluted high resolution XPS survey spectra of Si peak for *p*-Si with native oxide, H-terminated p- & n-Si are presented in Figures 4.13, 4.14 and 4.15 respectively. The three spectra have two peaks in common, one near 99 eV and another near 100 eV corresponding to $\mathrm{Si}_{2p3/2}$ and $\mathrm{Si}_{2p1/2}$ respectively. Only in case of p-Si with native oxide, there is an additional peak near 104 eV corresponding to Si surface oxidation. The absence of this peak at both H-terminated n- and p- Si surfaces provides evidence that there is not noticeable Si surface oxidation and the oxygen peak noticed on the survey spectra is due of adventitious oxygen on the surface before loading the sample to XPS analysis chamber.

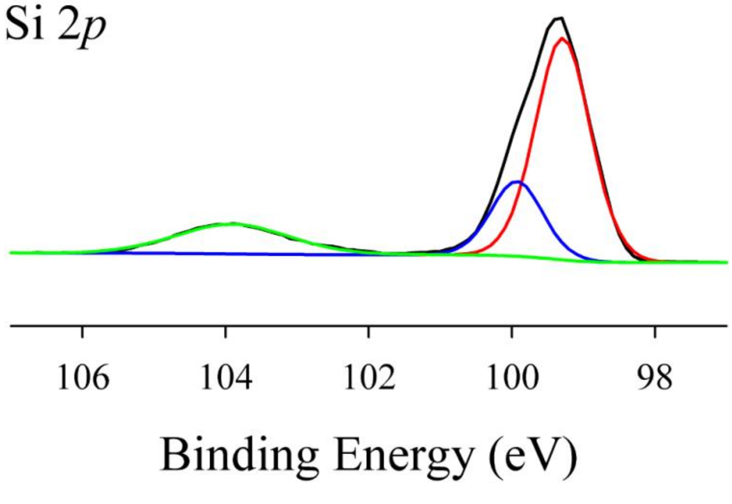

Figure 4.13. High-resolution XPS spectrum (black curve) for Si_{2p} peak of p-Si(111) with native oxide, the analysis showing three peaks. The first peak (red curve) at 99.3 eV, the second peak (blue curve) at 99.9 eV and the third peak (green curve) at 103.9 eV and correspond to Si-O bond of the SiO_x.

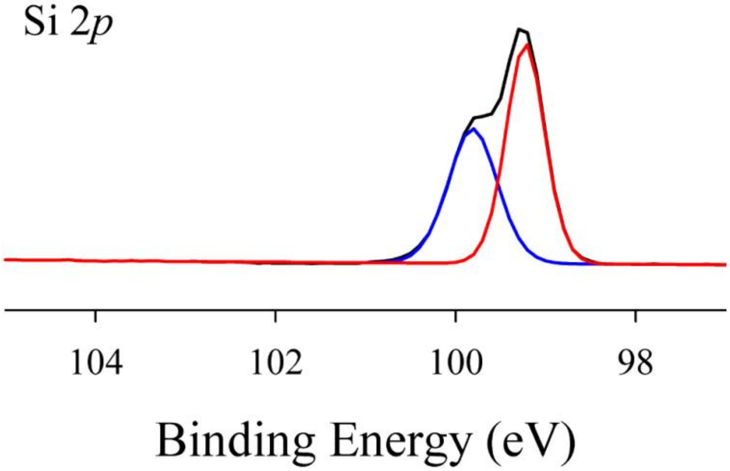

Figure 4.14. High-resolution XPS spectrum analysis for Si_{2p} peak of H-terminated p-Si(111), the analysis showing only two peaks, the first peak (red curve) at 99.2 eV, the second peak (blue curve) at 99.8 eV.

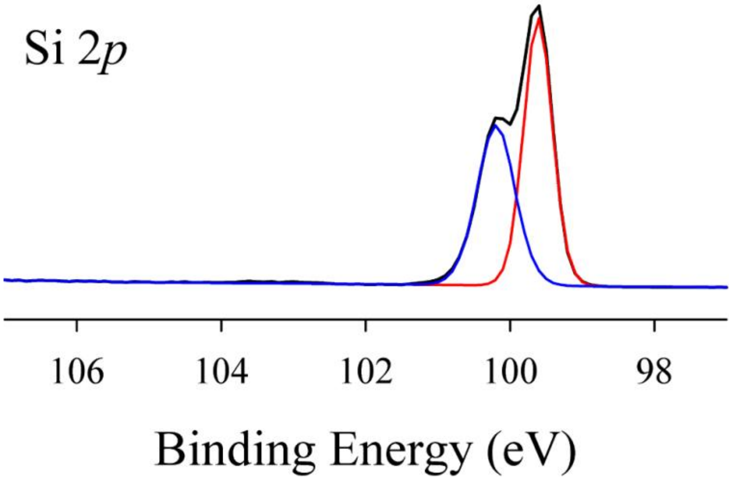

Figure 4.15. High-resolution XPS spectrum analysis for Si_{2p} peak of H-terminated n-Si(111) sample, the analysis showing two peaks, first peak (red curve) at 99.6 eV, the second peak (blue curve) at 100.2 eV.

Survey XPS spectra of both *p*- and *n*- Si/NAB modified samples are shown in Figures 4.16 and 4.17 respectively. In both samples, there are strong peaks near 282 eV, 400 eV and 532 eV corresponding to C_{1s}, N_{1s} and O_{1s} peaks of the NAB molecular layer respectively. For Si substrate signal, there are two very week signals near 100 eV and 150 eV corresponding to Si_{2p} and Si_{2s}. This significant attenuation of Si signal indicates that Si substrate is buried under multilayers of NAB molecules, and indeed the magnitude of this attenuation was used to calculate the multilayer thickness in the literature*[48]*. The deconvolution of high resolution C_{1s} peak in Figure 4.18 results in two peaks, one peak near 284.4 eV corresponds to C-C bond of aromatic system, while the peak near 285.2 eV correspond to C-N bond. While the fitting of N_{1s} peak in Figure 4.19 results in two peaks, the first peak at 399.9 eV corresponds to nitrogen of the of the azo (N=N) group and the second peak at 405.7 eV represents nitrogen of the nitro (NO_2) group of NAB molecular layer. Molecular layer density of both *n*- and *p*-type modified Si samples was compared by calculating area of N_{1s} peak/Si_{2p} peak. In case of *p*- type modified Si/NAB, the ratio of N/Si was 3.5, and for *n*- type, the ratio of N/Si was 3.3. This result indicates that molecular layer density is similar in both samples.

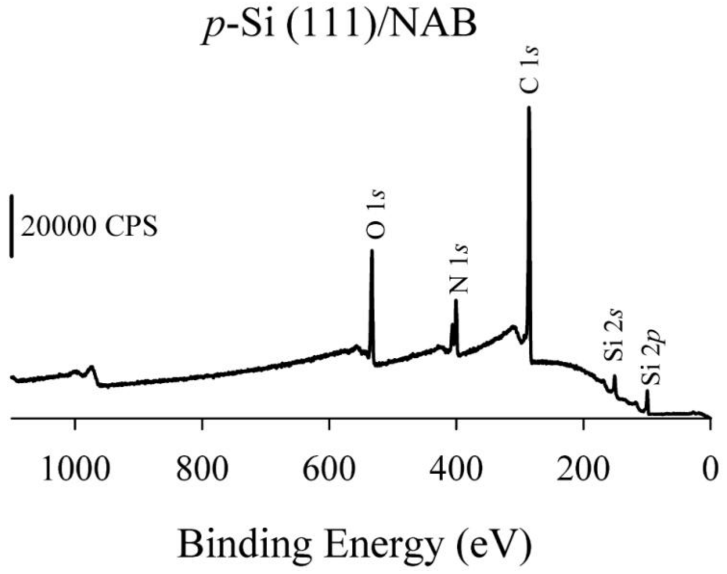

Figure 4.16. XPS survey spectrum analysis for H-terminated *p*-Si/NAB sample.

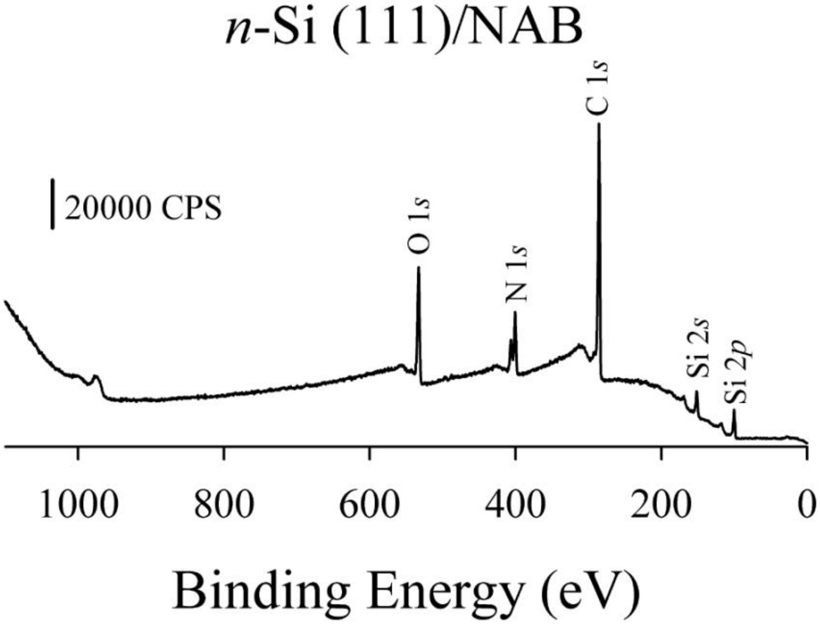

Figure 4.17. XPS survey spectrum analysis for H-terminated *n*-Si/NAB sample.

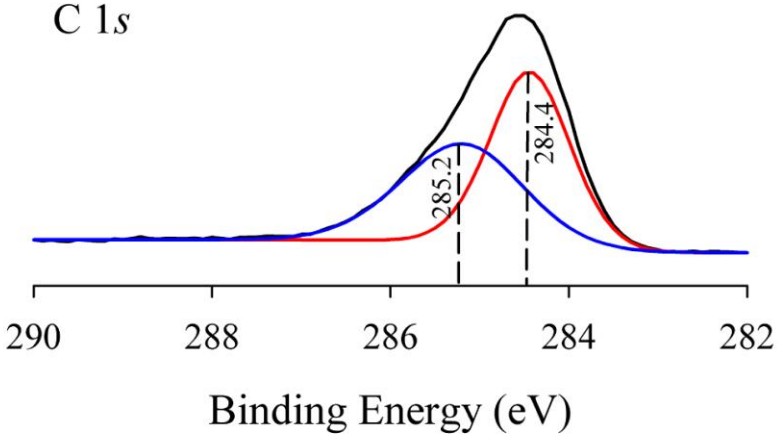

Figure 4.18. High resolution XPS spectrum for C_{1s} of p-Si/NAB sample the deconvolution analysis showing two peaks, one peak (red curve) at 284.4 eV and the other peak (blue curve) at 285.2 eV.

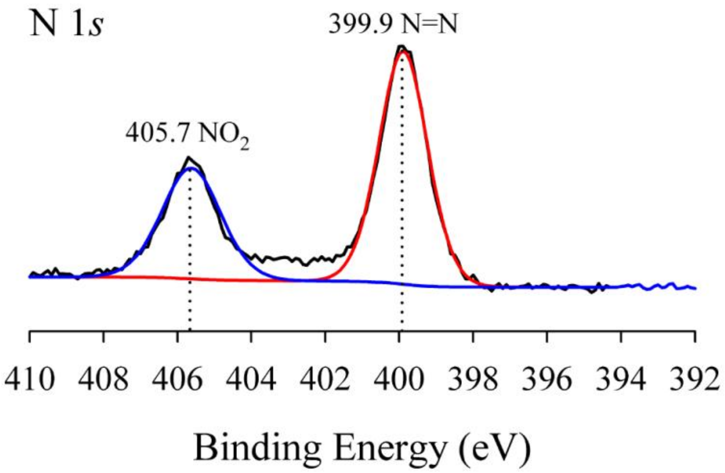

Figure 4.19. High resolution XPS spectrum for N_{1s} of p-Si/NAB sample. The analysis showing two peaks, the first peak (red curve) at 399.9 eV and the second peak (blue curve) at 405.7 eV.

Figures 4.20 and 4.21 are high resolution spectra of Si_{2p} peak of *p*- & *n*-Si/NAB samples, both have a small peak near 103 eV indicating oxidation of the Si surface occurred and formation of Si-O bond. This oxidation probably occurred during the electrochemical modification process as those samples were prepared in parallel with the H-terminated Si samples shown above.

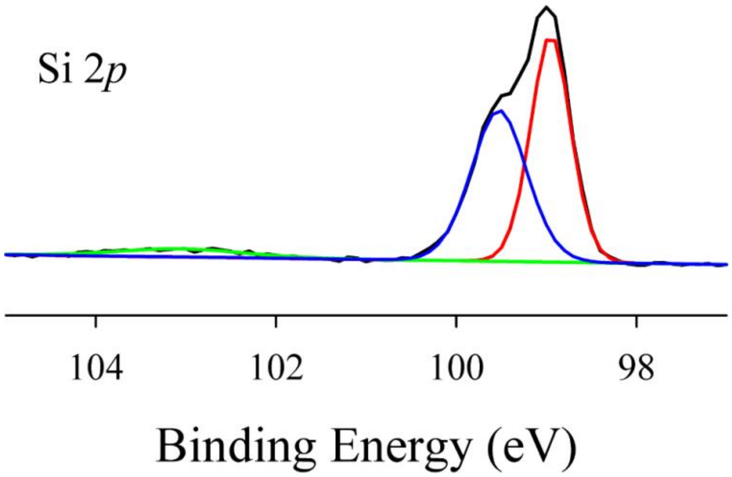

Figure 4.20. High-resolution XPS spectrum analysis for Si_{2p} peak of H-terminated p-Si/NAB, the analysis showing three peaks, first peak (red curve) at 98.9 eV, the second peak (blue curve) at 99.5 eV and the third one (green curve) at 102.9 eV.

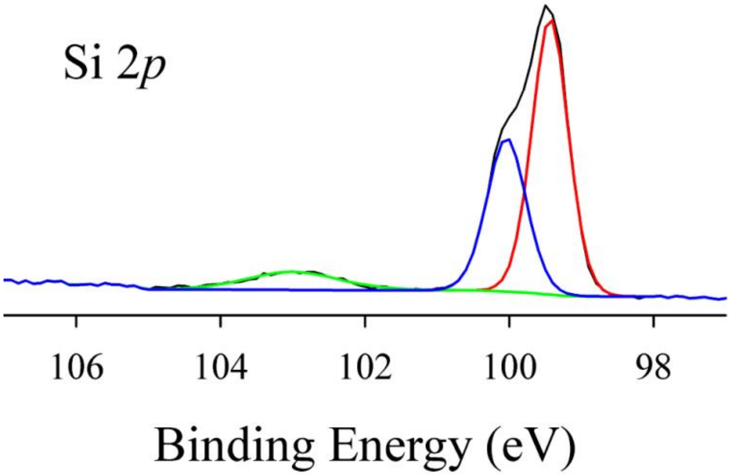

Figure 4.21. High-resolution XPS spectrum analysis for Si_{2p} peak of H-terminated n-Si/NAB-4, the analysis showing three peaks, first peak (red curve) at 99.4 eV, the second peak (blue curve) at 100.1 eV and the third one (green curve) at 102.9 eV.

4.3.1.4 Ultra-violet Photoelectron Spectroscopy (UPS)

Ultraviolet photoelectron spectroscopy analysis of Si surfaces permits measurements of the valence band energy and work function (WF) as reported in the literature*[48, 49]*. The work function can be calculated as the difference between the secondary electron cutoff energy E_{cutoff}, where the He radiation can not excite any electrons out of the sample and the radiation energy ($h\nu$ =21.2 eV).

$$WF = h\nu - E_{cutoff}$$

Where h is Plank’s constant and ν is the radiation frequency. In Figure 4.22, the UPS spectra of both H-terminated n- & p-Si are shown. In addition, the electron cutoff region is magnified in the inset. The UPS spectra of modified p- & n-Si (111)/NAB are compared to corresponding H-terminated Si sample and are shown in Figures 4.23 and 4.24 respectively. The WF for H-terminated Si and modified Si/NAB samples were calculated and summarized in Table 4.2.

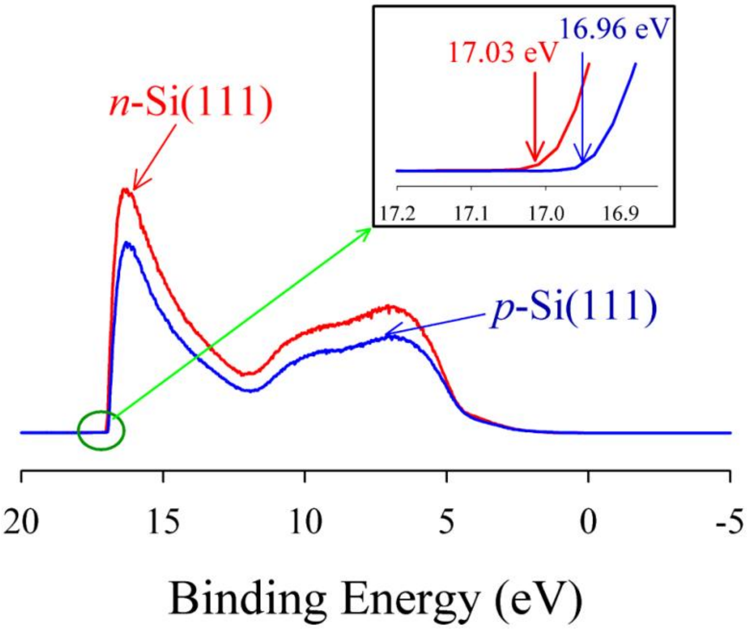

Figure 4.22. UPS spectra of hydrogen-terminated p-Si(111) blue curve and hydrogen-terminated n-Si(111) red curve. The inset is magnification of the secondary electron cutoff region.

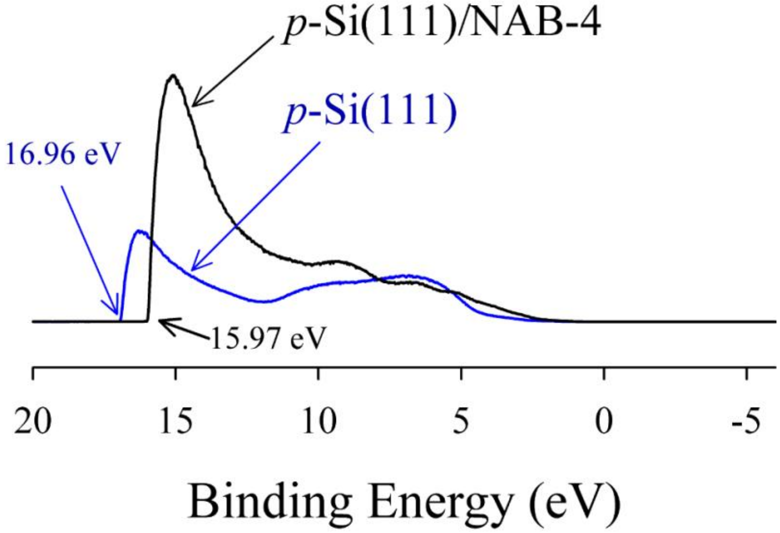

Figure 4.23. UPS spectra of hydrogen-terminated p-Si(111) blue curve and p-Si(111)/NAB black curve.

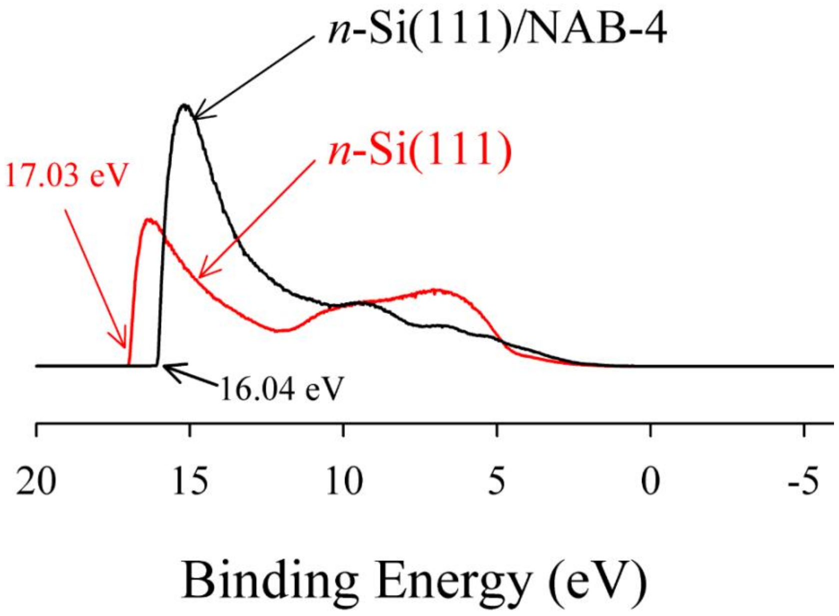

Figure 4.24. UPS spectra of hydrogen-terminated n-Si(111) red curve and p-Si(111)/NAB black curve.

From Figure 4.23 and 4.24, it is obvious that surface modification with NAB molecule results in an apparent shift of 1 eV in the work function of Si substrate. For both n- and p- Si samples, the shift is ~1 eV, indicates that the shift is substrate independent and depends mainly on the molecular layer attached. This shift is attributed to molecular layer dipole moment and band bending as discussed previously in detail*[48, 49]*.

UPS data is quite informative for modified Si samples. The onset of electron emission in the low binding energy region (0 to 14 eV) has been used to estimate the highest occupied molecular orbital (HOMO) onset of the molecular layer on the Si surface*[50, 51]*. HOMO onset is determined by performing a linear fit of the low binding energy edge of the spectrum, then determining the point where the background intersects *[3, 51, 52]* , and shown in Figure 4.25 for modified *p*- & *n*-type Si/NAB samples. The energy offset between the Fermi level and HOMO is considered as the tunneling barrier height for hole transport (ϕ_{h+}) as discussed below. The data of WF and HOMO energy offsets was determined for modified p- and n-Si/NAB and included in Table 4.2.

Sample	Work Function (eV)	E_{Fermi} - HOMO
H-terminated p-Si	-4.24	--
H-terminated n-Si	-4.17	--
p-Si/NAB	-5.23	1.01
n-Si/NAB	-5.16	1.04

Table 4.2. Summary of work function and energy difference between E_{Fermi} & HOMO extracted from UPS data for both modified and H-terminated *n*- & *p*-Si(111) samples.

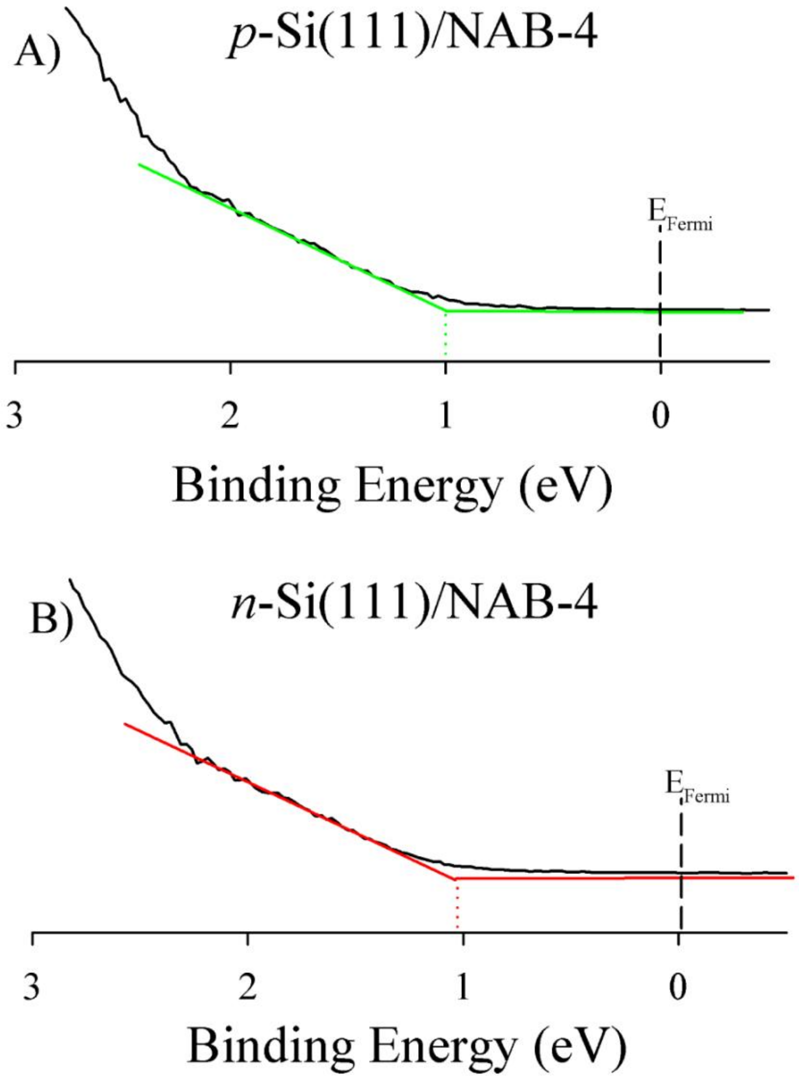

Figure 4.25. HOMO onset calculation from UPS spectra of (A) *p*-Si(111)/NAB sample and (B) *n*-Si(111)/NAB sample.

4.3.2 Junction Electrical Characterization

The interfacial resistance between Au contact pads and H-terminated Si surface is low (~ 17Ω) as calculated form the *i*-*V* curve shown in Figure 4.2, indicating that the Au/Si interface does not dominate the junction's electrical behavior. The logarithm of current density versus bias (ln |*J*| *vs. V)* for n- and p-type Si/NAB/Cu junctions are compared to that of carbon (PPF)/NAB junction of similar thickness in Figure 4.26. From this Figure, it is apparent that n-Si/NAB/Cu junctions are about 2 orders of magnitude more conductive than both p-Si/NAB junctions & PPF/NAB junctions of similar molecular layer thickness. Furthermore, p-Si/NAB/Cu/Au junctions are less conductive than PPF/NAB/Cu junction at negative bias and have a similar current density for positive bias, due to a difference in symmetry. Also both n- and p- Si/NAB/Cu/Au junctions show unsymmetrical conductivity, where n-Si/NAB/Cu/Au junctions are more conductive under negative bias while p-Si/NAB/Cu/Au junctions are more conductive when a positive bias was applied as apparent in normalized linear scale of J *vs.* V in Figure 4.27. Reproducibility of junctions is shown in Figure 4.28, where the ln $|J|$ curve for n-Si/NAB junctions is the average of 21 junctions out of 24, and errors bars of 1 standard deviation. The remaining 3 junctions exhibited 10 times higher currents than the average, implying direct Cu to Si contact. For p-Si/NAB junction, the ln $|J|$ curve represents the average of 12 junctions out of 16 with 1 standard deviation (the other 4 junctions exhibited 10 times higher current than the average. Scans to higher bias (± 1.2 V) are presented in Figure 4.29. The current behavior was less reproducible at high voltage so most of the analysis and comparisons are based on the ± 0.7 V range.

Janes and co-workers studied diazonium-derived molecular junctions on a Si substrate and reported a yield of non-shorted devices of 46-83%. Of the non-shorted devices, the range of current densities was ±50% from the median value*[25]*. For the p-Si/molecule/Cu junctions described in the current chapter, the yield was 75% and the rsd of $J_{0.5V}$ was 29%.

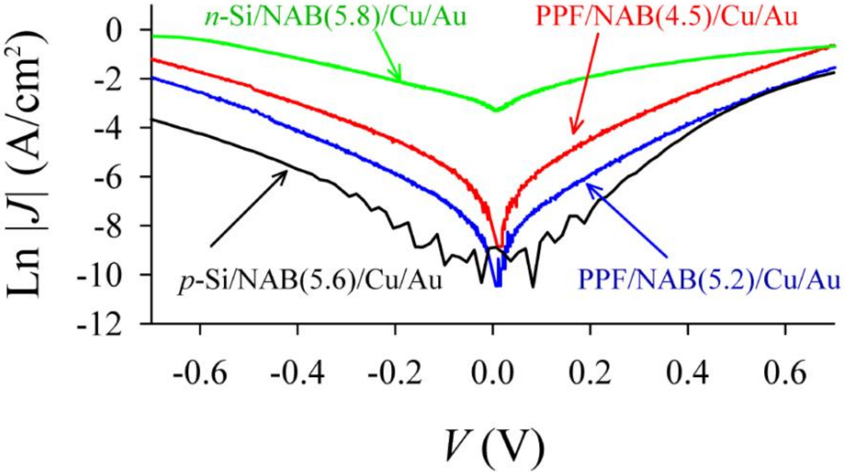

Figure 4.26. Overlay of ln |*J*|-*V* curves of *p*-Si(111)/NAB(5.6)/Cu(30)/Au(15) black curve, *n*-Si(111)/NAB(5.8)/Cu(30)/Au(15) green curve, PPF/NAB(5.2)/Cu(30)/Au(15) blue curve and PPF/NAB(4.5)/Cu(30)/Au(15) red curve.

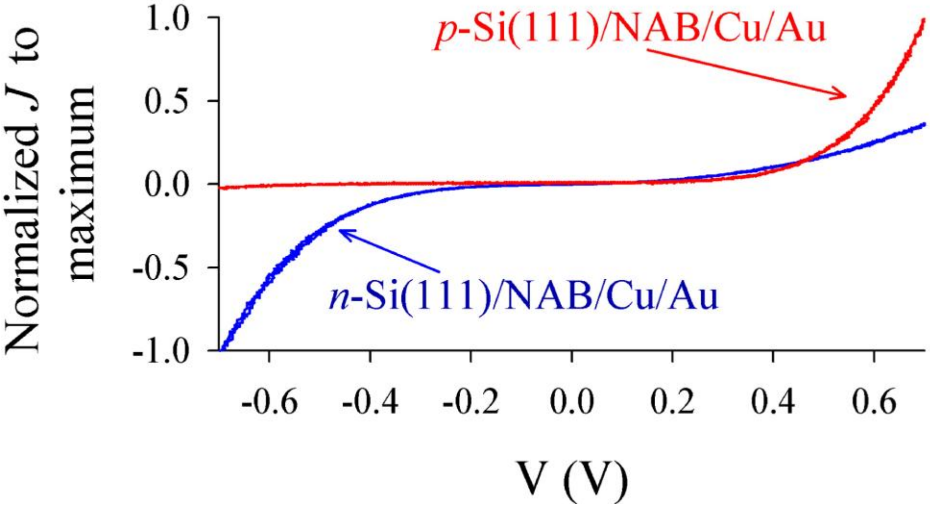

Figure 4.27. Normalized *J*-*V* curves of *p*-Si(111)/NAB(5.6)/Cu/Au, *n*-Si(111)/NAB(5.8)/Cu/Au.

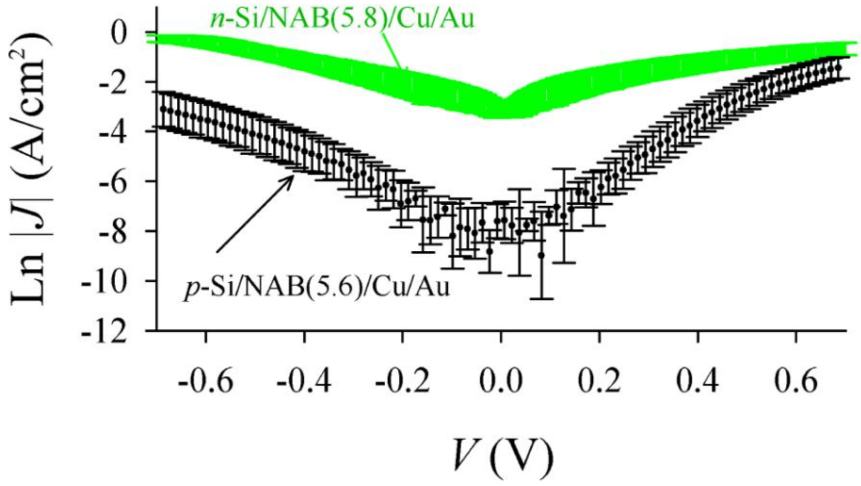

Figure 4.28. Average of ln |*J*|-*V* curves for 12 junctions of *p*-Si(111)/NAB(5.6) /Cu/Au with 1 standard deviation black curve, Average of ln |*J*|-*V* curves for 21 *n*-Si(111)/NAB(5.8)/Cu/Au junctions with 1 standard deviation green curve.

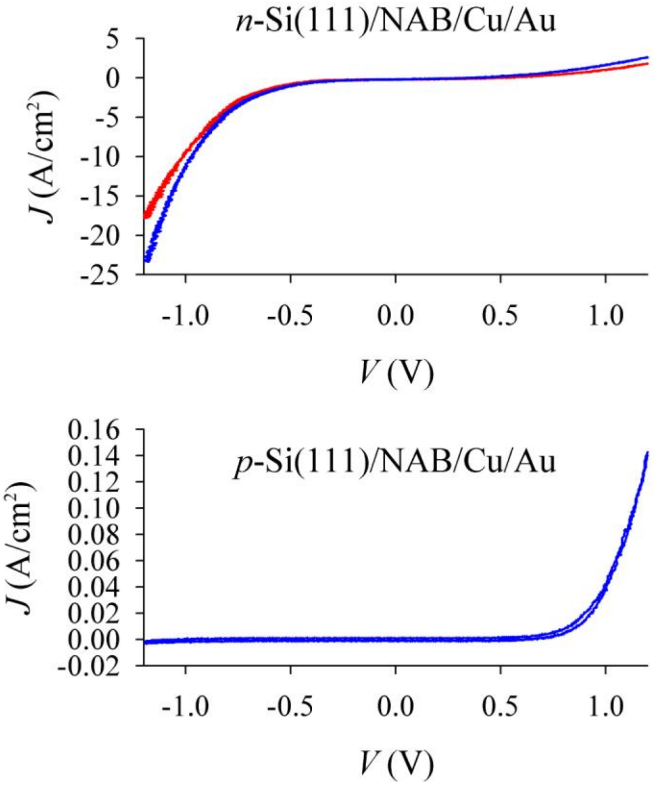

Figure 4.29. High voltage scan of *n*-Si(111)/NAB/Cu/Au (top curve) & *p*-Si(111)/NAB/Cu/Au junctions (bottom curve).

Although the current densities for n-Si substrates are much higher than that for p-Si, the curves have opposite asymmetry, with p-Si exhibiting larger currents with the p-Si biased positive. A similar asymmetry was reported for molecular junctions based on aromatic molecular monolayer attached to p- and n-Si*[25, 29]* and molecular junctions based on p-Si modified by alkyl molecular monolayer and using a Hg top contact*[51]*. For Si/aromatic molecular junctions, the authors proposed that the asymmetry is caused by charge transfer near resonance*[25]* or resonant tunneling of charge carriers through molecular layer HOMO*[29]*. Although a similar model can be used to explain the asymmetry observed in Si/NAB/Cu junctions, some important differences should be considered. First, the reported doping level of n-type Si was lower than the doping level in the current work and so in their case semiconductor property of Si dominates the junction behavior. The authors reported asymmetry in current-voltage curves even without a molecule present*[25]*. Second, the semiconductor Fermi level energy, molecular layer HOMO and LUMO positions were based completely on simulation and theoretical values, and no experimental values were presented*[25, 29]*.

To understand the difference in conductivity between n-type Si/NAB/Cu junctions and both p-Si/NAB/Cu and C/NAB/Cu junctions, the tunneling barrier height (ϕ) needs to be estimated, as it strongly influences the tunneling probability. For metal/molecule junctions, the offset between Fermi level and molecular HOMO is considered the energy barrier for hole transport (ϕ_{h+}) and the offset between Fermi and molecular LUMO is the barrier for electron transport

(ϕ_e) as shown in Figure 4.30. The barrier height for hole transport was estimated from UPS data to be ~ 1.2 eV*[53]* for PPF/NAB/Cu junctions, determined as offset between C Fermi level and molecular layer HOMO.

Before extending this approach to the semiconductor/molecule junction, it should be noted that the Fermi level is defined as the energy state where the probability is 1/2 that the level is occupied by an electron*[54]*. In a metal electrode, all energy levels below the Fermi level are filled with electrons as there are numerous available energy states, while for a semiconductor, with no dopants, there are no available energy states in the band gap and the Fermi level resides in the middle of the band gap. Upon doping, new energy states become available in the band gap, and the Fermi level is modified according to the dopant level and type*[55]*. In case of p-type semiconductors, the barrier for hole transport (ϕ_{h+}) is the offset between the Fermi level and molecular HOMO, while barrier for electron transport (ϕ_e) is the difference between the conduction band edge and molecular LUMO*[50]* as shown in Figure 4.30.

The theoretical barrier height for hole transport (ϕ_{h+}) through PPF/NAB can be estimated from the offset between bare PPF Fermi level (4.6 eV as measured from UPS*[53]*) and HOMO of gas phase free NAB molecule (6.66 eV as reported from Gaussian calculation, B3LYP.631G(d)*[53]*) to be **1.94 eV**, and for p-Si/NAB to be **2.4 eV** (p-Si Fermi level is 4.24 eV from UPS data Table 4.2). For n-Si/NAB, the theoretical barrier height for electron transport (ϕ_e) can be estimated as the offset between LUMO of gas phase free NAB molecule (3.04 eV as reported from Gaussian calculation*[53]*) and the conduction band edge (4.05 eV), yielding a barrier height (ϕ_e) of **1.0 eV**. According to the theoretical calculation, the barrier height for tunneling (ϕ) in case of n-Si/NAB/Cu junctions is smaller than for both p-Si/NAB/Cu and C/NAB/Cu junctions. So based on free molecular energy levels, n-Si/NAB/Cu junctions should be more conductive than both p-Si/NAB/Cu and C/NAB/Cu junctions of similar layer thickness. In the next section, the experimental barrier height for tunneling (ϕ) will be estimated from UPS data.

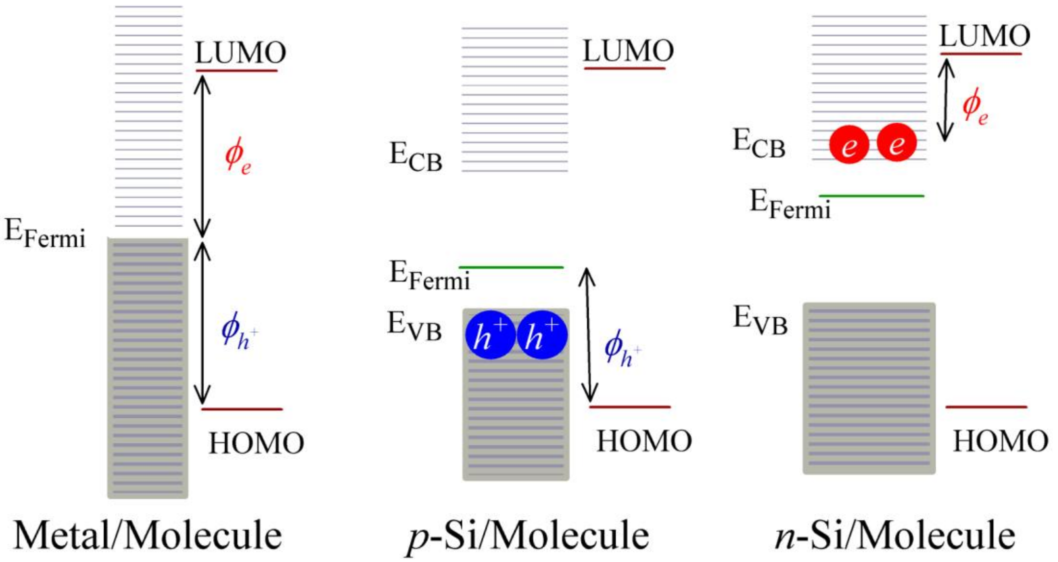

Figure 4.30. Charge transfer barrier height (ϕ) through metal/molecule interface, p-Si/molecule interface and n-Si/molecule interface.

UPS has been used to estimate the experimental hole barrier height for PPF/NAB/Cu junctions and reported to be 1.2 eV*[53]*, which is the difference between bare PPF Fermi and HOMO of NAB molecular layer bonded to PPF. By referring to UPS data in Table 4.2, tunneling barrier height for hole transport (ϕ_{h+})

for p-Si/NAB/Cu junctions was estimated to be ~ 1 eV, which explains the similarity in current density between p-Si/NAB/Cu and PPF/NAB/Cu junction at positive bias. The lower current density at negative bias is explained below. It should be noted that there is a shift in HOMO level upon bonding to the surface which result in a significant decrease of the theoretical barrier height (ϕ) (0.7 eV for PPF/NAB and 1.4 eV in case of p-Si/NAB).

Although the offset between Fermi level and molecular HOMO (ϕ_{h+}) is 1 eV in case of n-type Si/NAB/Cu junctions, the major charge carriers are electrons not holes. Therefore the barrier for electron tunneling (ϕ_e) would be the offset between molecular LUMO (which can be estimated from inverse photoemission spectroscopy IPES*[51, 56]*) and conduction band edge*[50]*. Although no IPES data are available for n-Si/NAB sample, a shift in NAB molecular LUMO similar to that occurred with the HOMO is expected to occur during bonding. That shift will bring LUMO closer to conduction band and result in a decreasing of the theoretical (ϕ_e) to less than 1 eV. This small barrier height in case of n-type Si/NAB junctions is lower than that in both p-type Si/NAB/Cu and PPF/NAB/Cu junctions, consistent with the higher conductivity of the n-Si/NAB devices.

To explain the asymmetry in both p- and n-type Si/NAB/Cu junctions, energy band diagrams based on the UPS data described above are shown in Figure 4.31. Although the LUMO level was not determined experimentally, the expected effect of an applied bias on the energy band diagram is shown in Figures 4.32 and 4.33 for *p*- and *n*-type Si/NAB/Cu junctions respectively.

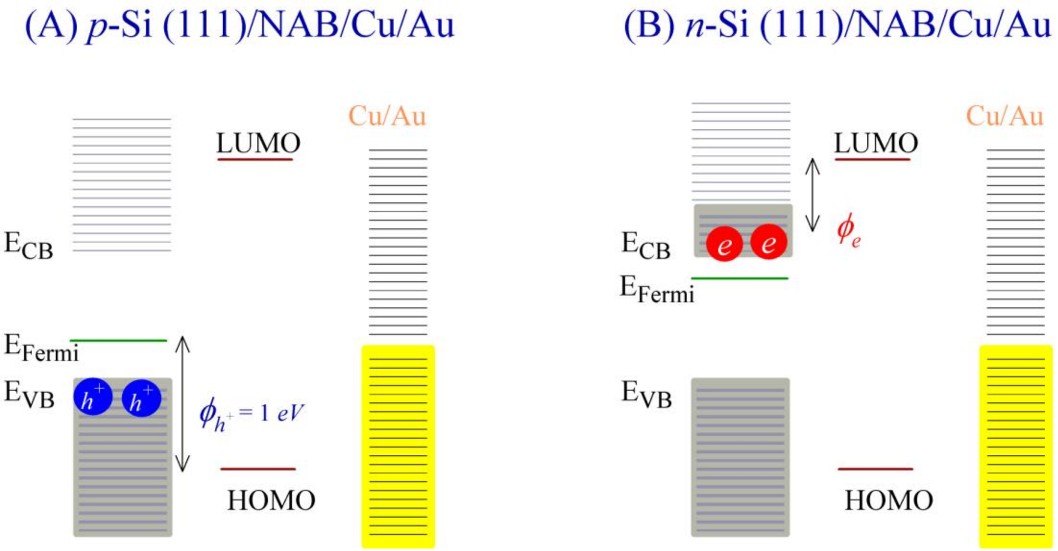

Figure 4.31. (A) Energy level diagram of *p*-Si(111)/NAB/Cu junctions based on UPS data, (B) energy level diagram of *n*-Si(111)/NAB/Cu junctions.

When a positive bias is applied to p-Si in Si/NAB/Cu/Au junctions, the majority charge carriers (holes) tunnel from the semiconductor valence band to the filled energy level in Cu metal. At higher bias, the Fermi level of Cu will come closer to Si conduction band and electrons have a greater probability to tunnel through the barrier from Cu metal into the vacant energy level of Si conduction band. While under negative bias, the Cu Fermi level will be at lower energy than the Si valance band, so the hole tunneling probability from Si valence band to Cu metal will decrease, as shown in Figure 4.32. Therefore, the model shown in Figure 4.32 for p-Si predicts higher currents for positive bias on Si, as observed experimentally (fig 4.26).

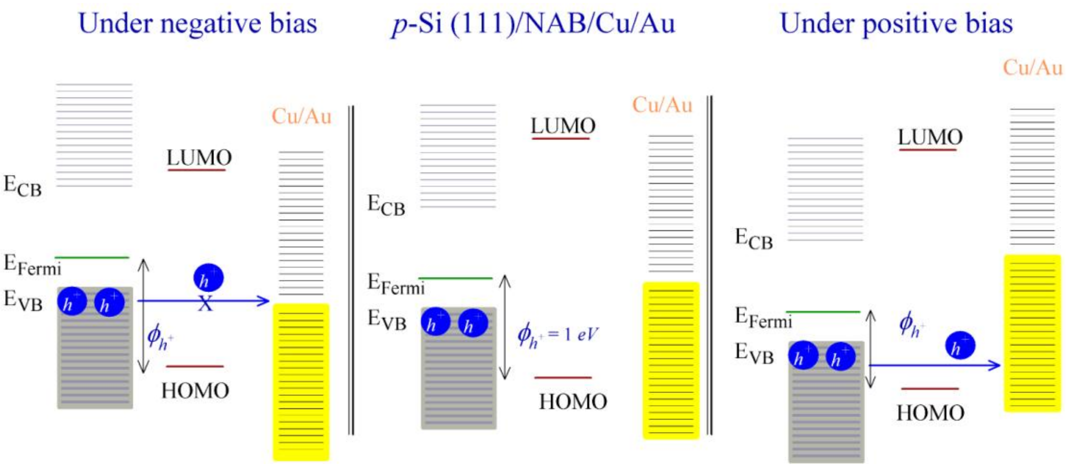

Figure 4.32. Energy band diagram of p-Si/NAB/Cu/Au junctions under application of positive and negative bias to the Si substrate.

For n-Si/NAB/Cu/Au junctions (Figure 4.33), the conduction band electrons are the majority charge carriers. When a negative bias is applied on Si, more electrons will populate the Si conduction band and (ϕ_e) will decrease. So more electrons will tunnel from the conduction band to the Cu vacant energy level. While applying a positive bias on n-Si, the electron population in conduction band will decrease and (ϕ_e) will increase, thus reducing the electron tunneling probability. The result is higher currents for negative bias in n-Si/NAB junctions, as observed experimentally (fig 4.26).

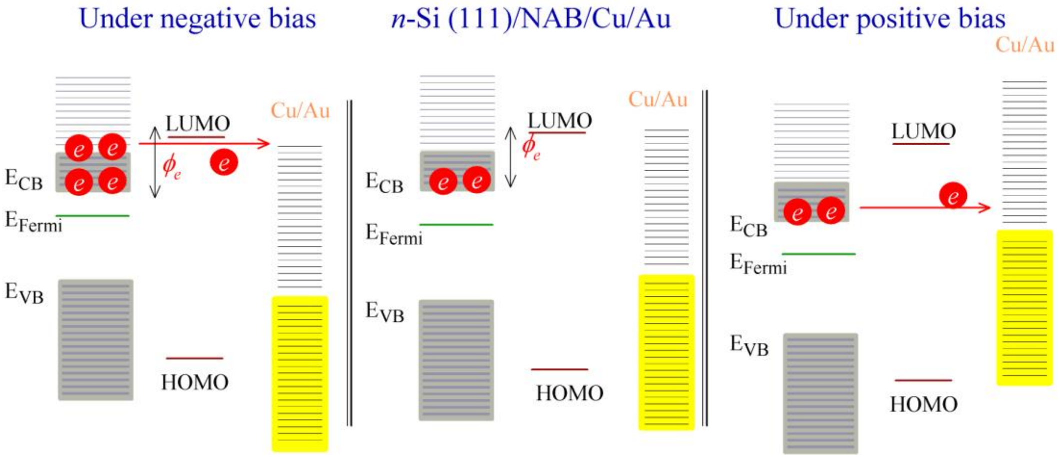

Figure 4.33. Energy band diagram of *n*-Si/NAB/Cu/Au junctions under application of positive and negative bias to the Si substrate.

4.4 Conclusions

In conclusion, H-terminated n- and p- type Si(111) samples have been modified by electrochemical reduction of NAB diazonium ion to produce an NAB molecular multilayer. Substrate modification was confirmed by AFM, Raman spectroscopy and XPS. AFM data indicates that the Si/NAB surface is flat (0.3 nm rms of roughness) and also indicates multilayer formation (NAB thickness > 5 nm). Cu metal was deposited on top of modified Si/NAB samples to fabricate molecular electronic junctions. The Si/NAB/Cu junctions are reproducible and were fabricated with high yield. The junctions were characterized electrically and compared with carbon based molecular junctions. n-Si/NAB/Cu junctions are much more conductive than both p-Si/NAB/Cu and PPF/NAB/Cu molecular electronic junctions having comparable molecular layer thicknesses. This variation in conductivity was attributed to smaller barrier height for charge tunneling in n-Si/NAB/Cu junctions. In the n-Si devices, the barrier is the difference between the molecular LUMO and conduction band edge, since the dominant carrier is the electron. For both p-Si and PPF junctions, hole tunneling predominates, and the barrier is E_{Fermi} – HOMO. A model based on the energy levels predicted from UPS results is consistent with both the magnitude and symmetry of the observed current/voltage response for all three types of molecular junctions.

4.5 References

[1] F. Anariba, K. Steach Jeremy, L. McCreery Richard, *The journal of physical chemistry. B* **2005**, *109*, 11163.

[2] O. Yaffe, L. Scheres, S. R. Puniredd, N. Stein, A. Biller, R. H. Lavan, H. Shpaisman, H. Zuilhof, H. Haick, D. Cahen, A. Vilan, *Nano Letters* **2009**, *9*, 2390.

[3] B. Kim, S. H. Choi, X. Y. Zhu, C. D. Frisbie, *Journal of the American Chemical Society* **2011**, *133*, 19864.

[4] L. Luo, A. Benameur, P. Brignou, S. H. Choi, S. Rigaut, C. D. Frisbie, *Journal of Physical Chemistry C* **2011**, *115*, 19955.

[5] S. H. Choi, C. D. Frisbie, *Journal of the American Chemical Society* **2010**, *132*, 16191.

[6] L. Luo, C. D. Frisbie, *Journal of the American Chemical Society* **2010**, *132*, 8854.

[7] F. Thieblemont, O. Seitz, A. Vilan, H. Cohen, E. Salomon, A. Kahn, D. Cahen, *Advanced Materials* **2008**, *20*, 3931.

[8] O. Yaffe, L. Scheres, L. Segev, A. Biller, I. Ron, E. Salomon, M. Giesbers, A. Kahn, L. Kronik, H. Zuilhof, A. Vilan, D. Cahen, *Journal of Physical Chemistry C* **2010**, *114*, 10270.

[9] H. Haick, J. Ghabboun, O. Niitsoo, H. Cohen, D. Cahen, A. Vilan, J. Y. Hwang, A. Wan, F. Amy, A. Kahn, *Journal of Physical Chemistry B* **2005**, *109*, 9622.

[10] B. Kim, J. M. Beebe, Y. Jun, X. Y. Zhu, C. D. Frisbie, *Journal of the American Chemical Society* **2006**, *128*, 4970.

[11] V. B. Engelkes, J. M. Beebe, C. D. Frisbie, *Journal of the American Chemical Society* **2004**, *126*, 14287.

[12] R. J. Nichols, S. J. Higgins, *Nature Nanotechnology* **2012**, *7*, 281.

[13] H. J. Yan, A. J. Bergren, R. L. McCreery, *Journal of the American Chemical Society* **2011**, *133*, 19168.

[14] R. Kumar, H. J. Yan, R. L. McCreery, A. J. Bergren, *Physical Chemistry Chemical Physics* **2011**, *13*, 14318.

[15] A. J. Bergren, R. L. McCreery, S. R. Stoyanov, S. Gusarov, A. Kovalenko, *Journal of Physical Chemistry C* **2010**, *114*, 15806.

[16] A. J. Bergren, K. D. Harris, F. Deng, R. L. McCreery, *Journal of Physics: Condensed Matter* **2008**, *20*, 374117/1.

[17] A. M. Mahmoud, A. J. Bergren, N. Pekas, R. L. McCreery, *Advanced Functional Materials* **2011**, *21*, 2273.

[18] J. Ru, B. Szeto, A. Bonifas, R. L. McCreery, *Acs Applied Materials & Interfaces* **2010**, *2*, 3693.

[19] A. P. Bonifas, R. L. McCreery, *Nano Letters* **2011**, *11*, 4725.

[20] A. P. Bonifas, R. L. McCreery, *Nature Nanotechnology* **2010**, *5*, 612.

[21] L. Segev, A. Salomon, A. Natan, D. Cahen, L. Kronik, F. Amy, C. K. Chan, A. Kahn, *Physical Review B* **2006**, *74*.

[22] J. M. Buriak, *Chemical reviews* **2002**, *102*, 1271.

[23] D. D. M. Wayner, R. A. Wolkow, *Journal of the Chemical Society-Perkin Transactions 2* **2002**, 23.

[24] S. Ciampi, J. B. Harper, J. J. Gooding, *Chemical Society Reviews* **2010**, *39*, 2158.

[25] A. Scott, D. B. Janes, C. Risko, M. A. Ratner, *Applied Physics Letters* **2007**, *91*.

[26] A. Scott, C. A. Hacker, D. B. Janes, *Journal of Physical Chemistry C* **2008**, *112*, 14021.

[27] W. Wang, A. Scott, N. Gergel-Hackett, C. A. Hacker, D. B. Janes, C. A. Richter, *Nano Letters* **2008**, *8*, 478.

[28] A. Scott, D. B. Janes, *Journal of Applied Physics* **2009**, *105*.

[29] S. Bala, R. K. Aithal, P. Derosa, D. Janes, D. Kuila, *Journal of Physical Chemistry C* **2010**, *114*, 20877.

[30] A. Scott, D. B. Janes, *Ieee Transactions on Nanotechnology* **2010**, *9*, 494.

[31] A. Scott, C. Risko, N. Valley, M. A. Ratner, D. B. Janes, *Journal of Applied Physics* **2010**, *107*.

[32] M. Coll, N. Gergel-Hackett, C. A. Richter, C. A. Hacker, *Journal of Physical Chemistry C* **2011**, *115*, 24353.

[33] M. Coll, C. A. Richter, C. A. Hacker, *Journal of Vacuum Science & Technology B* **2009**, *27*, 2826.

[34] A. Vilan, O. Yaffe, A. Biller, A. Salomon, A. Kahn, D. Cahen, *Advanced Materials* **2010**, *22*, 140.

[35] Y. Selzer, A. Salomon, D. Cahen, *Journal of Physical Chemistry B* **2002**, *106*, 10432.

[36] Y. L. Loo, D. V. Lang, J. A. Rogers, J. W. P. Hsu, *Nano Letters* **2003**, *3*, 913.

[37] H. H. Yang, R. L. McCreery, *Journal of the Electrochemical Society* **2000**, *147*, 3420.

[38] S. H. DuVall, R. L. McCreery, *Journal of the American Chemical Society* **2000**, *122*, 6759.

[39] P. Allongue, M. Delamar, B. Desbat, O. Fagebaume, R. Hitmi, J. Pinson, J. M. Saveant, *Journal of the American Chemical Society* **1997**, *119*, 201.

[40] G. S. Higashi, R. S. Becker, Y. J. Chabal, A. J. Becker, *Applied Physics Letters* **1991**, *58*, 1656.

[41] G. S. Higashi, Y. J. Chabal, G. W. Trucks, K. Raghavachari, *Applied Physics Letters* **1990**, *56*, 656.

[42] P. Jakob, P. Dumas, Y. J. Chabal, *Applied Physics Letters* **1991**, *59*, 2968.

[43] F. Anariba, S. H. DuVall, R. L. McCreery, *Analytical Chemistry* **2003**, *75*, 3837.

[44] J. Ramsey, S. Ranganathan, R. L. McCreery, J. Zhao, *Applied Spectroscopy* **2001**, *55*, 767.

[45] A. M. Nowak, R. L. McCreery, *Analytical Chemistry* **2004**, *76*, 1089.

[46] F. Anariba, U. Viswanathan, D. F. Bocian, R. L. McCreery, *Analytical Chemistry* **2006**, *78*, 3104.

[47] T. L. Barr, *Applied Surface Science* **1983**, *15*, 1.

[48] R. Hunger, W. Jaegermann, A. Merson, Y. Shapira, C. Pettenkofer, J. Rappich, *Journal of Physical Chemistry B* **2006**, *110*, 15432.

[49] T. He, H. J. Ding, N. Peor, M. Lu, D. A. Corley, B. Chen, Y. Ofir, Y. L. Gao, S. Yitzchaik, J. M. Tour, *Journal of the American Chemical Society* **2008**, *130*, 1699.

[50] A. Salomon, T. Boecking, C. K. Chan, F. Amy, O. Girshevitz, D. Cahen, A. Kahn, *Physical Review Letters* **2005**, *95*, 266807.

[51] O. Yaffe, Y. B. Qi, L. Scheres, S. R. Puniredd, L. Segev, T. Ely, H. Haick, H. Zuilhof, A. Vilan, L. Kronik, A. Kahn, D. Cahen, *Physical Review B* **2012**, *85*.

[52] Y. L. Gao, *Materials Science & Engineering R-Reports* **2010**, *68*, 39.

[53] S. Y. Sayed, J. A. Fereiro, H. Yan, R. L. McCreery, A. J. Bergren, *Proceedings of the National Academy of Sciences* **2012**, *109*, 11498.

[54] A. J. Bard, L. R. Faulkner, *Electrochemical methods: fundamentals and applications*, Wiley, New York **2001**.

[55] B. G. Streetman, S. K. Banerjee, *Solid State Electronic Devices*, Pearson Prentice Hall, **2006**.

[56] Y. B. Qi, O. Yaffe, E. Tirosh, A. Vilan, D. Cahen, A. Kahn, *Chemical Physics Letters* **2011**, *511*, 344.

Conclusions and Future Work

The incorporation of organic molecules as active elements into electronic devices is a major target for molecular electronics. In this thesis, the molecular layer integrity with current microfabrication processes was investigated by several spectroscopic techniques. Investigation of molecular layer integrity provides the limitations and challenges for practical employment of organic molecules into current microfabrication processes. In Chapter 2, a surface modification process was described to modify various substrates. Ultra-thin Ti metal was used as a primer to modify optically transparent substrates with organic molecular layers. The organic molecular layers were characterized through back-side spectroscopy after deposition of metal on top of the molecular layer. The spectroscopic data provided strong evidences that molecular layer covalently bonded to the metal primer have survived the direct metal deposition of Au (100 nm).

In Chapter 3, the compatibility of carbon based molecular junctions with current microfabrication processes was investigated. Four metals (Au, Cu, Ti and Pt) were deposited on carbon/ molecular layer to fabricate cross bar junctions. The metal deposition of Cu and Au did not disrupt the molecular layer, although Au appears to penetrate into the molecular layer. Spectroscopic data indicate that Ti and Pt deposition partially destroyed the molecular layer on carbon substrates. For Pt, the resulting carbon/molecules/Pt junctions were short circuits indicating direct contact between Pt and carbon electrode. In case of Ti, the junctions showed low conductivity probably due to of the formation of titanium carbides and oxides, which dominated the junctions' electrical behavior. These results regarding molecular layer integrity after metal deposition demonstrate the importance of spectroscopic characterization of the finished devices and why it should be considered before interpretation of electrical data.

The organic molecular layer covalently bonded to carbon electrode was shown to be stable at 400 ^{o}C under vacuum for 30 minutes, whereas the complete carbon/molecular layer/Cu junctions became more conductive after heating above 250 ^{o}C. The effect of a complete photolithographic process on molecular layer integrity was studied, and the results indicate that molecular layer can withstand a complete photolithographic process without damage.

In Chapter 3, the charge transfer mechanism within hybrid Si/molecular layer/Cu junctions was investigated and compared to previously studied carbon based molecular junctions. The junctions were reproducible and were fabricated with high yield. Both p-type Si and carbon based molecular junctions with the same layer thickness have similar conductivity, while significantly higher conductivity was observed for n-type Si molecular junctions compared to both p-type Si and carbon molecular junctions. Furthermore, both n- and p- type Si molecular junctions have asymmetric current–voltage behavior. The difference in conductivity was attributed to variations in tunneling barrier height. For n-type Si the barrier is the energy difference between the molecular LUMO and the conduction band edge for electron tunneling, while for both p-Si and PPF molecular junctions, the barrier is E_{Fermi} – HOMO for hole tunneling.

Future work might focus on the study of charge transfer mechanism in hybrid Si/molecular layer/Cu junctions. The nitroazobenzene molecular layer could be replaced by other molecules that have various LUMO energy relative to the conduction band in order to verify the hypothesis that the electron tunneling barrier in the case of n-type Si is the offset between LUMO and conduction band. This work should be supported by inverse photoemission spectroscopy (IPES) measurements to estimate that difference experimentally.

Furthermore, to understand the role of Si substrate in such a hybrid junction, Si wafers with a range of doping levels could be used as substrates. At high doping level the molecules should dominate the junctions' electrical behavior, while at low doping level the semiconductor character through formation of a Schottky barrier is expected to control the junctions' electrical behavior. Low doping levels in Si will permit fabrication of hybrid molecular junction where the electronic properties of both the semiconductor and the molecules affect the electrical behavior of the completed junction.

Appendix 1

UV-Vis study of the oxidation of ultrathin Ti metal

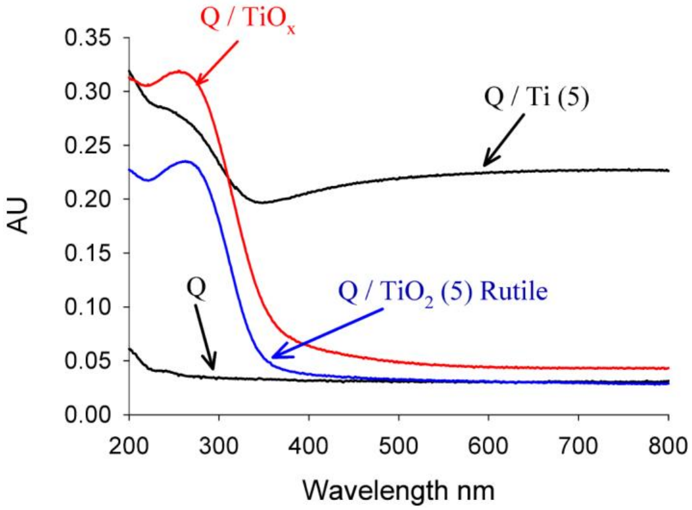

Figure 1A. UV-Vis spectra for samples of quartz (Q), 5 nm Ti deposited by e-beam onto Q (Q/Ti (5)), 5 nm rutile deposited by e-beam onto Q (Q/TiO$_2$ (5) Rutile) and Q/Ti sample after thermal oxidation (Q/TiO$_x$). All spectra were referenced to air.